THE UNIVERSITY *of* EDINBURGH

Phenomenology and Simulations of Active Fluids

Elsen Tjhung

A thesis submitted in fulfilment of the requirements
for the degree of Doctor of Philosophy
to the
University of Edinburgh
April 2013

Abstract

Active fluids are an interesting new class of non-equilibrium systems in physics. In such fluids, the system is forced out of equilibrium by the individual active particles - in constrast to driven systems where the system is forced out of equilibrium by some external forces. Some biological examples of active fluids are bacterial suspensions and actomyosin solutions inside eukaryotic cells. In the case of bacterial suspensions, the fluid is stirred internally by the swimming bacteria and as a consequence of this, active fluids can have some interesting physics of their own such as hydrodynamic instabilities and spontaneous symmetry breaking. Here, in particular, we study how such instabilities may arise and how they may lead to a non-equilibrium steady state.

We also study numerically a droplet of active matter as a simple representation of cell extract comprising actomyosin solution bounded by a cell membrane. It is widely believed that cell motility is driven only by actin polymerization pushing against the cell membrane. However, we show that even in the absence of actin polymerization, actin-myosin contraction alone can also generate a unidirectional motion. This happens due to the spontaneous breakdown of a discrete symmetry at large enough activity (i.e. actomyosin contraction). This non-equilibrium phase transition from stationary to motile state is somewhat similar to the second order phase transition in equilibrium thermodynamics.

Finally, we studied the behaviour of an active droplet on a two-dimensional surface to mimic cell crawling. Whereas cell migration in 3D environment maybe driven mainly by actin-myosin contraction (described above), cell crawling on a 2D surface is driven mainly by actin polymerisation. Here we find that localised actin polymerisation can cause protrusion in the cell membrane which is qualitatively similar to lamellipodium formation in cell crawling.

Declaration

Except where otherwise stated, the research undertaken in this thesis was the unaided work of the author. Where the work was done in collaboration with others, a significant contribution was made by the author.

E. Tjhung
April 2013

Acknowledgements

First of all, I would like to thank my supervisors Mike Cates and Davide Marenduzzo for suggesting this new and interesting PhD topic. I am also grateful for their many ideas and insightful comments. I also acknowledge support from SUPA prize studentship which has made this study possible.

Work in chapter 4 is done in collaboration with Adriano Tiribocchi and I would like to thank Adriano for the fruitful collaboration.

I have also benefited from useful discussions with A. N. Morozov for chapter 3, R. Voituriez and S. Ramaswamy for chapters 4 and 5 and many other people which I met during the conferences and summer schools. Finally I would like to thank all my colleagues working on active stuff, soft matter and biological physics for all the interesting and useful discussions.

Contents

List of Figures

List of Tables

Chapter 1

Why active fluids are interesting

In general, non-equilibrium systems in statistical physics can be divided into two distinct classes: active and driven systems. In driven systems, the system is forced out of equilibrium by some external forces such as temperature gradient or chemical potential gradient. A well known example of this is when we put a Newtonian fluid (such as water) in between two slabs of different temperatures (see Fig. 1.1). Suppose we keep the temperature of the bottom plate several degrees higher than the upper plate. This will then soon set up a temperature gradient across the fluid, which in turn, set the fluid into rolling motion (convection rolls [20]). In active systems, on the other hand, the system is forced out of equilibrium by the individual constituent particles themselves. An example of this is dense bacterial suspension [1], in which case, the fluid solvent is stirred internally by the swimming bacteria. Even in bacterial suspensions, we still see large-scale fluid rotations - similar to the convection rolls above (see Fig. 1.2(A)).

While active and driven systems share some common non-equilibrium physics (such as non-equilibrium steady states and spontaneous symmetry breaking), active systems possess even more rich non-equilibrium phenomena. One such example is giant density fluctuations. As we may know from equilibrium physics, the number density fluctuation for a system in contact with a reservoir typically goes down with the system size (in fact it scales as $\frac{\Delta N}{N} \sim \frac{1}{\sqrt{N}}$, where N is the total number of particles). However in active systems, the number density fluctuation may actually increase with the system size. This is illustrated in the experiment of Narayan and Ramaswamy [21]. In this experiment, rod-like particles are vibrated on an oscillating disc and they observe that such particles tend to cluster together;

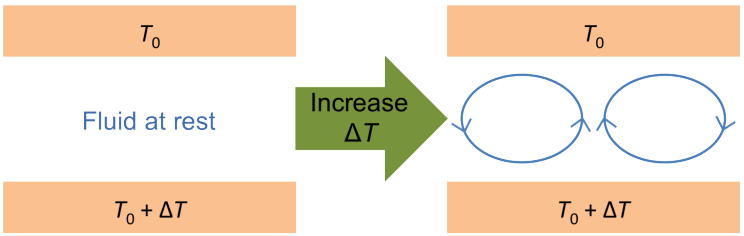

Figure 1.1: Rayleigh-Benard instability. We observe convection rolls in the fluid medium (blue lines) as the temperature difference across the two plates is increased.

increasing the number density fluctuation greatly. Correspondingly they measure the number density fluctuation to scale as $\frac{\Delta N}{N} \sim 1$.

We can further classify active systems into two groups: dry active systems and active fluids. Bacterial suspensions are an example of active fluids since they consist of active particles (bacteria) suspended in a fluid solvent (passive viscous fluid). Vibrated granular rods [21] may also constitute an active fluid even though the solvent is absent in this case. This is because the rods as a whole behave like a fluid with some effective viscosity[1]. In general, active fluids must satisfy the conservation of momentum (Navier-Stokes equation), whereas, dry active systems do not have a simple momentum balance equation. An example of dry active systems is flocks of birds [22] - whose direction of flying can change rapidly.

In this thesis, we will mainly talk about active fluids and the variety of non-equilibrium physics they display. In addition, we shall also mention their relevance to some biological systems from time to time.

1.1 Biological examples of active fluids

Many examples of active fluids come from living/biological systems. One example is dense bacterial suspension which contains a large concentration of bacteria dispersed in a viscous fluid. Such a simple system already displays some novel collective behaviours such as pattern formation [23] and turbulence [24] (see Fig. 1.2(A)).

Another biological system of interest is represented by eukaryotic cells. These are biological cells which come from most animals' and plants' tissues. Eukaryotic

[1]Actually some momentum is lost to the plate. However this momentum loss can be dealt with systematically *via* a friction term.

cells have long been known to be able to move in various media. For example, keratocyte cells from fish scales have been observed to be able to crawl on a 2D glass substrate [25]. Another example is tumour cells which are able to swim inside a 3D tissue in vivo or polymeric gel in vitro [12]. While the mechanism for cell crawling has been explained (to certain degrees), the mechanism for cell swimming is still largely unknown.

Such abilities for cells to move can be beneficial (*e.g.* in the case of wound healing [26, 27]) or pathological (*e.g.* in the case of tumour cells migration to invade various parts of human body [16]). For these reasons, cell motility remains an active area of research both in biology and biological physics. Our study of active fluids is also closely related to cell motility and in fact, a crawling/swimming/moving cell can be simply modelled as a droplet of active fluids - as we will illustrate below.

1.1.1 Bacterial suspensions

One biological example of active fluids - already mentioned above - are the bacterial suspensions. Other than being non-equilibrium, bacterial suspensions also show macroscopic orientational order at high density (see Fig. 1.2(A)). The origin of this orientational ordering may come from excluded volume interactions between one bacterium and its neighbours - since the bacteria have rod-shaped bodies [28]. This is similar to polar liquid crystals [29] - with the polarity defined to be the direction of swimming.

Fig. 1.2(B) shows the schematics of a single bacterium swimming with velocity $\mathbf{w}$ relative to a viscous fluid in the background. The swimming motion is typically driven by the rotation of a flagella bundle at the back. This flagella bundle exerts a force of magnitude $F_{self-propel}$ on the bacterial body and of the same direction as $\mathbf{w}$ (see Fig. 1.2(B) left). Since the Reynolds number for a bacterium is typically very small, this self-propel force will be balanced by a drag force from the fluid on the the bacterium with magnitude (assuming spherical shape): $F_{drag} = 6\pi\eta R w$, where η is the fluid viscosity, $R \sim 2\,\mu$m is the size of the bacterium and w is the swimming speed. And thus we have $F_{drag} = F_{self-propel}$. The Reynolds number is defined to be the ratio of the inertial force to the viscous force: $Re = \frac{\rho U L}{\eta}$ where ρ is the mass density, U is the typical velocity and L is the typical lengthscale. η is the shear viscosity of the fluid. In the case of bacterial suspensions, the Reynolds

number is typically very small ($Re \sim 10^{-5}$ [30]) and thus we may neglect the inertia. Consequently the net force on the bacteria has to be zero.

Due to this force balance, a swimming bacterium is effectively a force dipole consisting of two point forces separated by some distance R. The directions of these two point forces against the fluid solvent are indicated by the block arrows in Fig. 1.2(B) right. This force dipole will then create a quadrupolar fluid flow around the bacterium (see blue lines in the figure). This fluid flow has been observed experimentally in Goldstein *et. al.* [2] (see Fig. 1.2(C)). They also notice that the fluid flow is long-range and decays as $\sim \frac{1}{r^2}$. And consequently, the fluid flow may affect the motion of another bacterium at a distance r away. This kind of long-range *hydrodynamic interaction*, therefore, cannot be neglected in our modelling of bacterial suspensions (or active fluids in general).

1.1.2 Actomyosin inside eukaryotic cells

Another example of biological active fluids is actomyosin inside a eukaryotic cell. The actomyosin solution is actually a network of protein filaments (actin) cross-linked by motor proteins (myosin); immersed in a fluid solvent. They are found near the periphery of a cell (see Fig. 1.3 (A)). Physically it constitutes a polymeric gel and is therefore viscoelastic - it behaves like an elastic solid at short timescale ($\ll 10\,\mathrm{s}$), and behaves like a viscous fluid at long timescale ($\gg 10\,\mathrm{s}$) [31]. However, the actomyosin is more than just a passive polymeric gel. The actin filaments can also grow (by polymerising at the plus/barbed ends), and in turn, push the cell membrane - creating protrusion (see chapter 4). Note that the actin filaments are polarised with the plus ends mostly pointing away from the nucleus (see Fig. 1.3 (A)). Moreover, these filaments are also cross-linked by motor proteins (myosin), which can pull the protein filaments together causing the whole cell to contract [32]. These two active processes are fuelled by chemical energy released from ATP→ADP conversion ($\sim 20\,k_BT$).

The actomyosin network/solution is believed to play an important role in cell motility, which is illustrated in experiments of [33, 34] (see Fig 1.3 (B)). The figure shows two snapshots of a keratocyte cell crawling on a glass slide at two different times. Also visible from the experiment is the lamellipodial protrusion (a thin sheet containing actomyosin which extends from the cell body). They observe that a lamellipodial extract from the same cell can also move on its own.

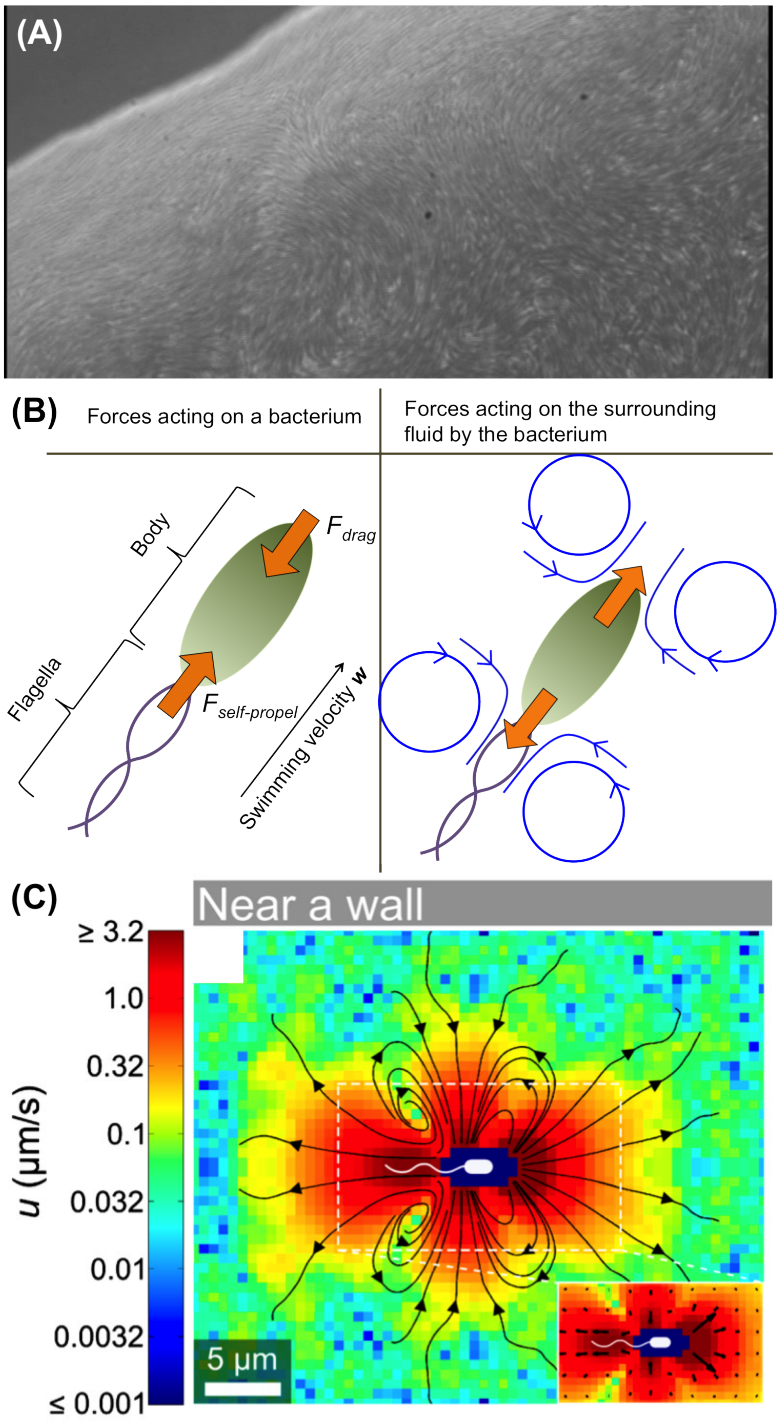

Figure 1.2: **(A)** shows an example of bacterial suspension [1]. The image shows some evidence of large-scale fluid rotations. (The width of this microscopy image is about $100\,\mu$m.) **(B)** Schematics of a single bacterium suspended in a fluid solvent. Shown in blue lines are the fluid velocity around the bacterium as a result of dipolar force. **(C)** Direct experimental measurement of the fluid velocity is consistent with the dipolar force model of a swimming bacterium [2].

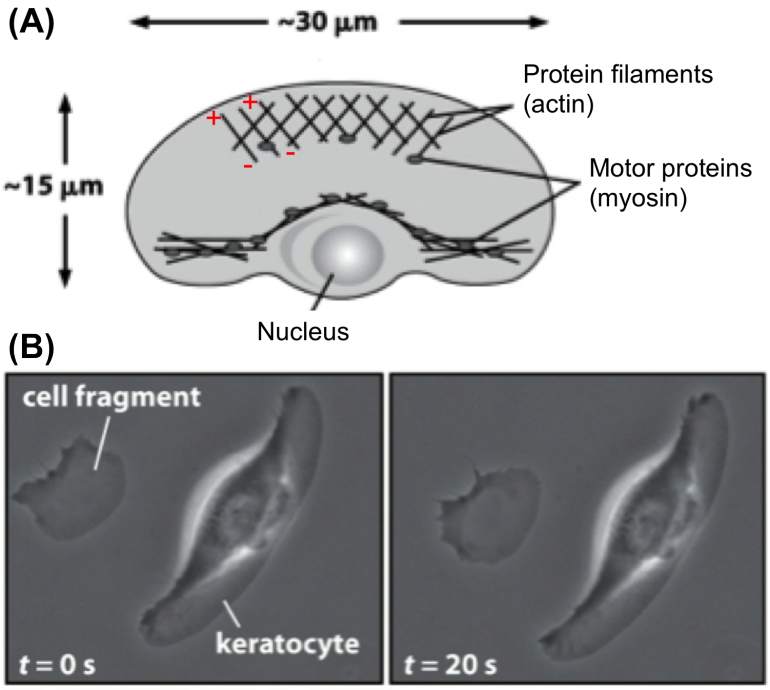

Figure 1.3: **(A)** Schematics of a eukaryotic cell showing the actomyosin network in the bulk of the cell. **(B)** Keratocyte cell crawling on a glass slide. (Figures adapted from [3]).

This shows that the actomyosin solution alone is enough to drive cell motility.

1.2 The physics of active fluids

Active fluid consists of active particles which are constantly doing work on the surrounding fluid (solvent) as they move around. The work done on the solvent is then dissipated as heat via friction/viscosity. The solvent itself is assumed to be an incompressible viscous fluid which satisfies the Navier-Stokes equation (or momentum balance equation) [20]:

$$\rho \frac{D\mathbf{u}}{Dt} = -\nabla P + \eta \nabla^2 \mathbf{u} + \nabla \cdot \underline{\underline{\sigma}} \tag{1.1}$$

where $\rho = constant$ is the mass density of the solvent, $\frac{D}{Dt}$ is a convective derivative, P is the isotropic pressure, η is the viscosity, and $\mathbf{u}$ is the velocity of the solvent. The isotropic pressure P can take any values at any instant to enforce the incompressibility condition: $\nabla \cdot \mathbf{u} = 0$. The only new thing (as compared to

a Newtonian fluid) in the above equation is $\underline{\underline{\sigma}}$ - a stress tensor - which represents momentum transfer from the solute to the solvent and *vice versa*. We usually split $\underline{\underline{\sigma}}$ into the equilibrium/passive and non-equilibrium/active part: $\underline{\underline{\sigma}} = \underline{\underline{\sigma}}^p + \underline{\underline{\sigma}}^a$. The equilibrium part of the stress tensor represents elastic response from the solutes. For example in nematic liquid crystals [35], we can have three different modes of elastic deformations: bend, splay and twist. Each of these elastic deformation will be accompanied by momentum transfer to and from the solvent. A lot of interesting things can happen if the solute particles are also active. These will contribute to an additional stress - active stress - which forces the system to be out of equilibrium internally. For example, it is known that some active liquid crystals can spontaneously induce splay deformation (without any external agent) [36], at the expense of an energetic cost due to elastic deformation.

There are many ways to model the individual active particles. One can simply model an active particle as a vibrating dumbbell for instance. However, this particle will not be able to move on its own and it will only do some work on the surrounding fluid (see Purcell's scallop theorem [30]). We call this type of particles '*shakers*'. Najafi and Golestanian [37] also modelled an active particle as a string of three connected beads. Provided we specify the correct vibrating frequencies for each connected bead, this active particle turns out to be able to swim in a straight line (relative to the fluid velocity in the background). We call this type of particles '*movers*'. These are a few models of active particles which could be used in a particle dynamics simulation. However, in this thesis, we will study such particles at a high concentration (*i.e.* hydrodyanamic limit). For this purpose, we will need a yet simpler model of active particles which can be coarse-grained more easily than beads and vibrating springs.

Ramaswamy *et. al.* [4] noted that the simplest realization of such particles turns out to be a permanent force dipole (see Fig. 1.4). The shape of the particles itself is assumed to be rod-like (like most bacteria and actin filaments). For movers, the particles must also be polar - with the polarity defined by the direction of swimming. For shakers however, the particles do not have to be polar - they may have a uniaxial body as in nematic liquid crystal. These particles can also be either extensile or contractile depending on the sign of the dipolar force (see Fig. 1.4). Notice that swimming bacteria (in Fig. 1.2) can be classified as extensile movers.

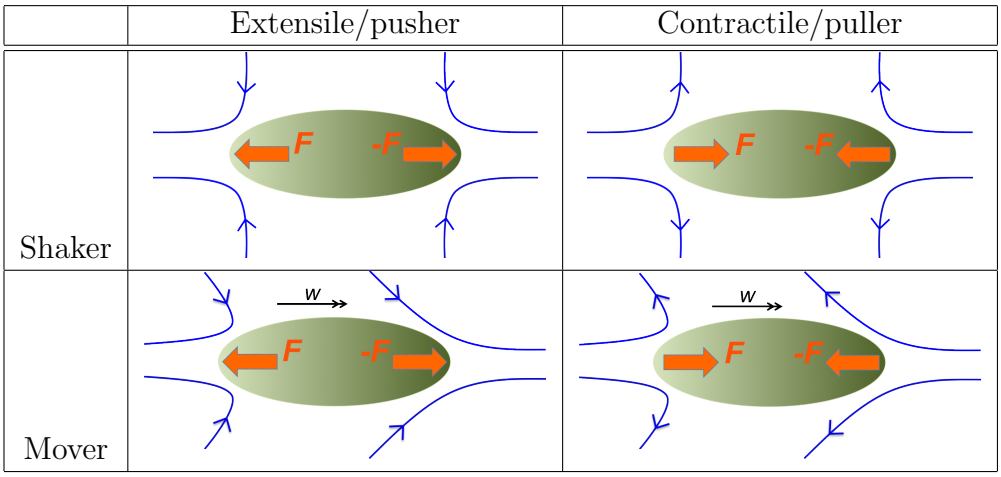

Figure 1.4: Classification of active polar particles [4]. Shown in blue lines are the quadrupolar fluid flow around the particle. In addition for movers, the particle is also swimming with velocity w relative to the surrounding fluid.

1.2.1 Rheology of active fluids

Active particle suspensions, or simply active fluids, have been shown to have some interesting rheology [4, 38]. Imagine a dense suspension of active shakers under an imposed shear stress (see Fig. 1.5). Since the active particles are rod shaped, under an applied shear, the particles will tend to align themselves in the direction of the shear (see Fig. 1.5). If the active particles happen to be extensile, the forces acting on the fluid by the particles will be in the same direction as the shear stress - and consequently tend to enhance the shear flow. On the other hand, if the particles happen to be contractile, the forces acting on the fluid will tend to oppose the shear flow. In other words, the presence of activity alone can increase/decrease the effective viscosity of the whole fluid.

More recently, active fluids have also been shown to have an unintuitive micro-rheology [39]. This involves dragging a colloidal particle in an active fluid. It was shown that the apparent drag coefficient (effective viscosity of the fluid) can change dramatically - depending on whether the active fluid is extensile or contractile. In particular for the contractile case, the drag coefficient may become negative.

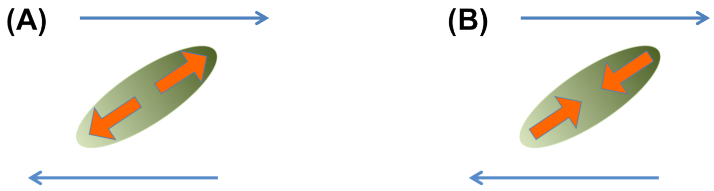

Figure 1.5: Sheared active particle suspension (only one particle is shown in the figure). The direction of the sheared fluid is given in blue arrows. **(A)** In the case of extensile, the dipolar force tends to enhance the fluid flow, thereby, decreasing the apparent viscosity. **(B)** In the case of contractile, the dipolar force tends to oppose the fluid flow, thereby, increasing the apparent viscosity.

1.2.2 Non-equilibrium steady states (NESS)

A common feature of non-equilibrium systems is the existence of non-equilibrium steady states (NESS). We will illustrate this idea by considering a suspension of shakers trapped in a one-dimensional box of size L (see Fig. 1.6). In 1D, all the particles are aligned in the same direction - say along the x-axis. Let us denote the concentration of the active particles to be $c(x,t)$. Suppose initially we have a uniform concentration of active particles: $c(x,t=0) = c_0 = constant$.

It turns out that there is a characteristic lengthscale L^* which depends on the magnitude of the pushing/pulling force from the particles [36, 40, 41]. Below this lengthscale ($L < L^*$), the system is stable with respect to small fluctuations and the particle concentration remains uniform. However above this lengthscale ($L > L^*$), any infinitesimal fluctuations in the particle concentration will be amplified until a steady state concentration $c(x, t \to \infty)$ is reached (see Fig. 1.6). In the extensile case, the particles are pushing away from each other. And since the particles are trapped in a box of size L, they will eventually accumulate near the walls. The steady state concentration for extensile particles will then look like Fig. 1.6 (A) right. On the other hands for contractile particles, the particles are pulling each other and they will accumulate at the centre [41]. The steady state concentration will then look like Fig. 1.6 (B) right. Actually the existence of any NESS in *strict*-1D active fluid requires the fluid flow to be compressible. (Otherwise the incompressibility condition $\nabla \cdot \mathbf{u} = 0$ will produce a no-flow solution $\mathbf{u} = 0$. For more mathematical detail of NESS in 1D, one can refer to Julicher *et al.* [41]).)

These steady states are obviously non-equilibrium ones since they do not

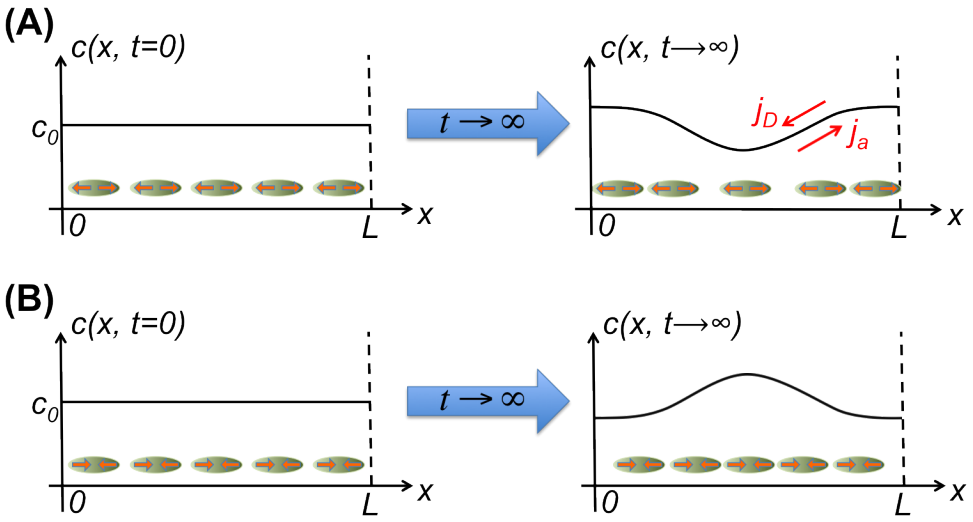

Figure 1.6: Non-equilibrium steady states in 1D active particles. The particles are trapped in between walls at $x = 0$ and $x = L$. Initially at $t = 0$, we have a uniform concentration of active particles which is then shown to be unstable as $t \to \infty$. The steady state concentration is denoted by $c(x, t \to \infty)$. For the case of extensile **(A)**, the particles will push each other so that we find more particles near the walls. And for the case of contractile **(B)**, the particles will pull each other so we will find more particles near the centre as $t \to \infty$.

follow the Boltzmann law: $c(x, t \to \infty) \neq Ae^{-E/k_BT}$, where E is the energy and A is the normalisation factor. Moreover if we look closely at one of the steady states we notice two non-zero currents flowing in the system (see the red arrows in Fig. 1.6 (A) right). The first one is a diffusive current: $j_D = -D\frac{\partial c}{\partial x}$, which describes passive diffusion from regions of high concentration to low concentration. And the second one is an active current j_a, due to particles being pushed towards the walls (in the case of extensile). At steady state, this active current will be balanced by the diffusive current so we have: $j_a = -j_D$. The same principle will also work for NESS in higher dimensions. For example in 2D active particle suspensions, this non-vanishing current will manifest itself in the form of fluid rotations - similar to the one observed in Rayleigh-Benard convection. This will be discussed further in chapter 3.

1.2.3 Spontaneous symmetry breaking (SSB)

Since spontaneous symmetry breaking (SSB) is a recurring theme in this thesis, it is useful to review this idea again. Consider a two dimensional elastic rod as shown in Fig. 1.7 (A). Suppose we apply a force F at both ends of the rod in equal magnitude and opposite direction as shown in the figure. If the magnitude of these two forces are small, the rod will be slightly compressed but still remain straight. However, if the applied force is large enough (above some critical value F_c) the rod will start to bend either upwards or downwards (see Fig. 1.7 (A)). This is in fact an example of SSB. Initially when the rod is straight, the system is invariant under reflection about the axis of symmetry (dashed line in the figure), however, this symmetry is lost after the rod starts to bend. To characterise this symmetry breaking, we introduce y to be the maximum vertical displacement of the rod. Consequently y is zero when $F < F_c$, but y can either be positive (bend upwards) or negative (bend downwards) when $F > F_c$. If we plot y as a function of F, we will then expect to see something like in Fig. 1.7 (B). Theory, of course, cannot predict which direction the rod is going to bend. Nevertheless, theory can still predict the shape of the curve - whether it is curve (i), (ii), or (iii) in Fig. 1.7 (B).

Suppose we denote the elastic energy stored in the rod to be E. This energy comes from both compression and bending deformation. Near the critical point F_c, we may expand E in power series of y:

$$E(y) = a_0 + a_1 y + a_2 y^2 + a_3 y^3 + a_4 y^4 \tag{1.2}$$

Note that since y is small near the critical point, we may stop the Taylor expansion at $O(y^4)$. Euler (and later Landau) soon noticed that the elastic energy of a bent rod is the same, whether the rod is bent upwards or downwards. In mathematical terms, this means $E(y) = E(-y)$ and the only way this is satisfied is when all the odd-power terms in Eq. (1.2) vanish. Thus we arrive at the Landau double-well energy:

$$E(y) = a_0 + a_2 y^2 + a_4 y^4 \tag{1.3}$$

We require $a_4 > 0$ so that the energy does not go to $-\infty$ as y becomes very large. a_2 can either be positive or negative and a_0 is assumed to be constant. To find

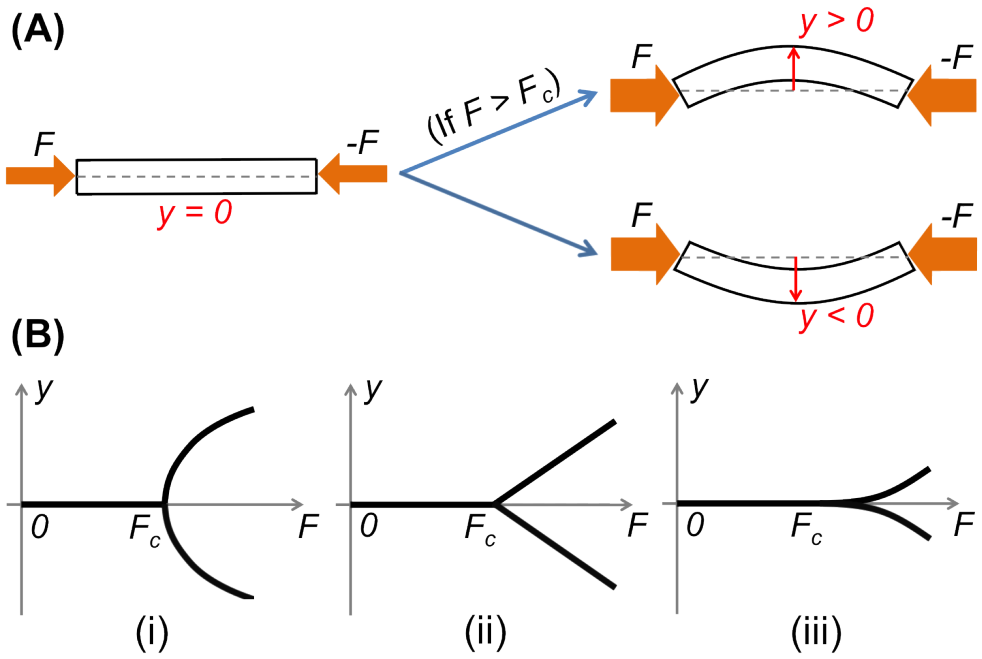

Figure 1.7: **(A)** Illustration of spontaneous symmetry breaking (SSB) in a 2D elastic rod. **(B)** Three possible solutions of $y(F)$ consistent with the SSB. By symmetry arguments (due to Landau), curve (i) turns out to be the correct solution.

the equilibrium value of y, we minimise $E(y)$; from which we obtain:

$$y = \begin{cases} 0 & , a_2 > 0 \\ \pm\sqrt{\frac{-a_2}{2a_4}} & , a_2 < 0 \end{cases} \tag{1.4}$$

Comparing this to Fig. 1.7 (B), we deduce $a_2 \sim -(F - F_c)$ and thus, $y \sim (F - F_c)^{0.5}$. The exponent 0.5 suggests that the curve will look more like (i) in Fig. 1.7 (B). This prediction of an *exponent* = 0.5 is a mean field result - not specific to this particular rod problem. In fact in the Rayleigh-Benard instability example above (Fig. 1.1), we might as well guess the angular velocity of the fluid rotation to scale as: $\omega \sim (\Delta T - \Delta T_c)^{0.5}$, since it also involves some SSB. In summary, the mean field result of an *exponent* = 0.5 applies to non-equilibrium systems as well as equilibrium systems - as long as some sort of SSB is involved and noise is absent. In chapter 5, we will consider an SSB of an active droplet which can lead to a translational motion - which is an unexpected consequence of SSB in non-equilibrium systems.

Finally it is also important to point out the distinction between SSB of a global and local symmetry. In the example above, the SSB refers to the breakdown of a global symmetry, which is a reflection of the whole plane about the axis of symmetry. Correpondingly, y is a global order parameter (since y is defined to be the maximum vertical displacement of the whole rod - which is a global property). However, later when we consider bacterial suspensions or actomyosin solutions, we will encounter SSB of a local symmetry. More specifically for bacteria, we may define a mesoscopic volume dV at some position $\mathbf{r}$ which contains sufficiently large number of bacteria. The bacteria inside this mesoscopic volume may undergo SSB from isotropic to polar state (*i.e.* from full rotational symmetry to none at all). We define the local order parameter $\mathbf{p}(\mathbf{r})$ to be the orientational average of all the bacteria inside the mesoscopic volume $dV(\mathbf{r})$. In isotropic state $\mathbf{p}(\mathbf{r})$ will be zero and thus invariant under arbitrary rotation, whereas in polar state, $\mathbf{p}(\mathbf{r})$ is finite. We can then construct the Landau potential energy as above:

$$E(\mathbf{p}(\mathbf{r})) = a_2 |\mathbf{p}(\mathbf{r})|^2 + a_4 |\mathbf{p}(\mathbf{r})|^4 \tag{1.5}$$

to describe SSB of local rotational symmetry inside the mesoscopic volume $dV(\mathbf{r})$. Note that it is possible to have different local symmetries at different points in space. For example, we may have polar order in regions where the density of bacteria is high and isotropic state in regions where the density of bacteria is low. The simplest way to do this phenomenologically is to add density dependence to a_2. More on this will be discussed in the chapter 4.

1.3 Outline of the thesis

In this thesis we will focus mainly on two main examples of active fluids: bacterial suspensions (Chapter 3) and actomyosin networks (Chapters 4 and 5). Despite the microscopic differences, the hydrodynamic descriptions of these two systems are actually rather similar (as we shall see later). The only difference is the sign of the activity parameter ζ with bacterial suspensions being extensile ($\zeta > 0$) and actomyosin systems being contractile ($\zeta < 0$). ζ here is a nonequilibrium parameter related to the internal active stress which can be positive (extensile) or negative (contractile). Another important nonequilibrium parameter is $w > 0$, which is always positive, and is related to the swimming/treadmilling speed of

the bacteria/actin filaments. These two nonequilibrium parameters (ζ and w) fully characterise an active fluid and they will be defined more fully in Chapter 3.

Besides varying the values of ζ and w, we shall also consider the effect of different geometries on the behaviour of an active fluid (see Table 1.1). For example in Chapter 3, we shall consider an extensile active fluid (such as bacterial suspensions) confined in between two parallel walls. And then in Chapters 4 and 5, we shall look at a droplet of contractile fluid as a simple representation of a eukaryotic cell (see Table).

	Chapter 3	**Chapter 4**	**Chapter 5**
Type of active fluids	Bacterial suspension $\zeta > 0$, extensile $w \geq 0$, swimming	Actomyosin $\zeta < 0$, contractile $w \geq 0$, treadmilling	Actomyosin $\zeta < 0$, contractile $w \geq 0$, treadmilling
Geometry considered	Confined between two walls	Droplet on a substrate	Droplet in a medium

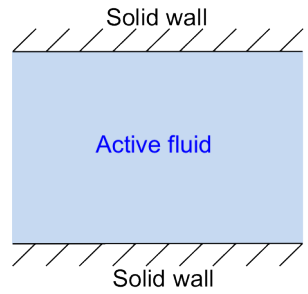

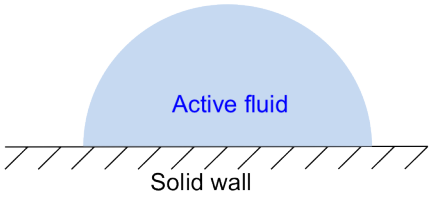

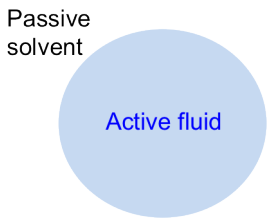

Table 1.1: **Map of thesis.** Thesis chapters are divided according to the geometry and system of interest (whether it is contractile or extensile).

Chapter 2

Hybrid lattice Boltzmann method

In many problems of complex fluids, we typically need to solve the incompressible Navier-Stokes equation:

$$\rho\left(\frac{\partial}{\partial t}+\mathbf{u}\cdot\nabla\right)\mathbf{u} = -\nabla P+\eta\nabla^2\mathbf{u}+\mathbf{f} \tag{2.1}$$

$$\nabla\cdot\mathbf{u} = 0 \tag{2.2}$$

coupled to some order parameter(s), say ϕ. (In general, the order parameter can be a vector or a tensor.) In the equation above η is the fluid viscosity, $\mathbf{f}$ is the force density acting on the fluid and P is the isotropic pressure which can take any value at any instant to satisfy the incompressibility condition (2.2). If the force density $\mathbf{f}$ originates from a short-range inter-molecular interaction, we can also write this force density as a gradient of the hydrodynamic stress: $\mathbf{f}=\nabla\cdot\underline{\underline{\sigma}}(\phi)$. Notice that the coupling from the order parameter ϕ enters through $\underline{\underline{\sigma}}$. Finally the time evolution of ϕ depends on whether ϕ is a conserved order parameter or not (see Bray [42]). In the case of a non-conserved variable, ϕ follows the equation below

$$\frac{\partial\phi}{\partial t}+(\mathbf{u}\cdot\nabla)\,\phi=-\frac{\delta F}{\delta\phi} \tag{2.3}$$

where $F[\phi]$ is a phenomenological free energy functional of ϕ. The term proportional to the gradient of the free energy on the right hand side of Eqn. (2.3) tends to relax the system towards the free energy minima (*i.e.* equilibrium).

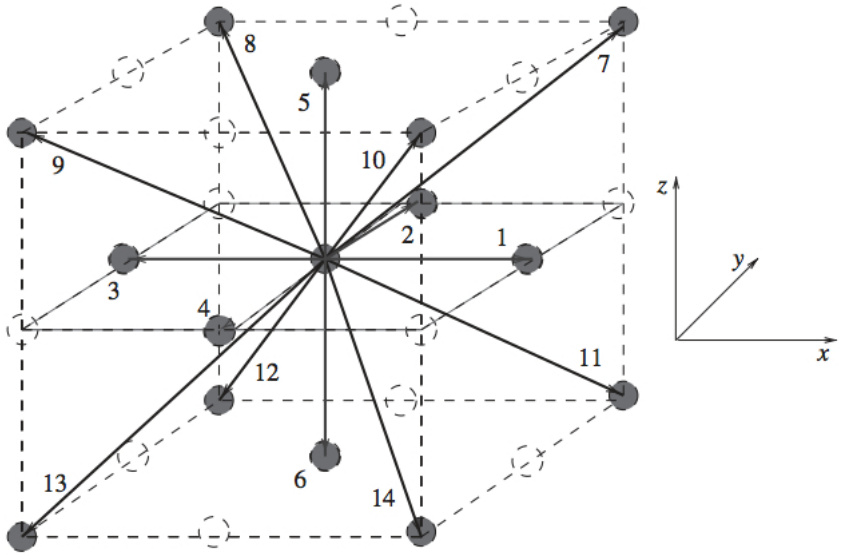

Figure 2.1: A set of lattice vectors in 3D which defines the fluid particles' velocities $\{\mathbf{v}_i\}$. The number corresponds to the index i of the particles' velocity $\mathbf{v}_i$. (Figure adapted from [5].)

The hydrodynamic stress $\underline{\underline{\sigma}}$ in Eqn. (2.1) will also depend on some free energy gradients (as we shall see in subsequent chapters). If the fluids are *active* like in this thesis (*i.e.* they are driven out-of-equilibrium internally), we will also have some terms which cannnot be written as a derivative of the free energy.

Solving this incompressible Navier-Stokes equation numerically can be a bit tricky. This is because one needs to update the fluid velocity $\mathbf{u}$ (at Δt timestep later) while maintaining the constraint $\nabla \cdot \mathbf{u} = 0$ at the same time. For instance, if we discretize a two-dimensional space into an $L \times L$ lattice points, this will amount to solving an $L \times L$ matrix or simultaneous equations. In summary, the lattice Boltzmann method (LB) simplifies this constraint by allowing the fluid density ρ to be slightly compressible. Below we shall explain briefly the hybrid lattice Boltzmann method which is used in all our simulations. More detail on this method can be found in Refs. [43, 44, 45, 46, 5].

2.1 Lattice Boltzmann equation

The lattice Boltzmann (LB) equation is basically a discretized version of the Boltzmann equation:

$$\frac{\partial f}{\partial t} + \mathbf{v} \cdot \nabla_{\mathbf{x}} f + \frac{\mathbf{F}}{m} \cdot \nabla_{\mathbf{v}} f = \left(\frac{\partial f}{\partial t} \right)_{coll} \tag{2.4}$$

where $f(\mathbf{x}, \mathbf{v}, t)$ is the particles distribution function in the phase space and $\mathbf{F}$ is the force acting on the particles. Here, rather than solving $\mathbf{u}$ and ρ explicitly, we introduce a mesoscopic distribution function $f(\mathbf{x}, \mathbf{v}_i, t)$, defined to be the number of fluid particles at position $\mathbf{x}$ and having velocity $\mathbf{v}_i$. Note that in LB, the position vector $\mathbf{x}$ is discretized to a d-dimensional lattice with lattice spacing $\Delta x = \Delta y = \Delta z$. Furthermore, the particles' velocities are also discretized such that $\mathbf{v}$ can only take a finite set of values $\{\mathbf{v}_0, \mathbf{v}_1, \ldots, \mathbf{v}_l\}$. In 3D, one choice of $\{\mathbf{v}_i\}$ is the following $l = 14$ lattice vectors:

$$\begin{aligned} \mathbf{v}_0 &= (0,0,0) \\ \mathbf{v}_{1-6} &= (0,0,\pm c), (0,\pm c,0), (\pm c,0,0) \\ \mathbf{v}_{7-14} &= (\pm c, \pm c, \pm c) \end{aligned} \tag{2.5}$$

where $c = \frac{\Delta x}{\Delta t}$. These lattice velocities are shown pictorially in Fig. 2.1. In LB simulations, it is also common to set the lattice spacing, timestep and particles' mass to be a unity: $\Delta x = \Delta t = m = 1$. The mapping between the simulation units and the physical units will be explained in more detail in the next chapter. The observables ρ and $\mathbf{u}$ can then be obtained from the distribution function $f(\mathbf{x}, \mathbf{v}_i, t)$ *via*

$$\rho(\mathbf{x}, t) = \sum_i f_i(\mathbf{x}, t) \tag{2.6}$$

$$\mathbf{u}(\mathbf{x}, t) = \frac{1}{\rho(\mathbf{x}, t)} \sum_i f_i(\mathbf{x}, t) \mathbf{v}_i \tag{2.7}$$

where we have introduced a shorthand notation: $f_i(\mathbf{x}, t) = f(\mathbf{x}, \mathbf{v}_i, t)$.

The lattice Boltzmann equation gives us the distribution function of the fluid

particles at time $t + \Delta t$:

$$\underbrace{f_i(\mathbf{x} + \mathbf{v_i}\Delta t, t + \Delta t) = f_i(\mathbf{x}, t)}_{\text{streaming}} + \Delta t F_i - \Delta t \underbrace{\left[\frac{f_i(\mathbf{x}, t) - f_i^0(\mathbf{x}, t)}{\tau}\right]}_{\text{collision}} \tag{2.8}$$

Notice that this equation is completely local. The term F_i is related to the force density $\mathbf{f}$ in the Navier-Stokes equation *via* $F_i = \mathbf{f} \cdot \mathbf{v}_i$ [46]. The collision integral is approximated as a difference between the distribution function f_i and its local equilibrium value f_i^0 (BGK approximation [47]). τ is the relaxation timescale for f_i to reach its equilibrium value (incidentally τ is also related to the macroscopic fluid viscosity η). In continuous Boltzmann equation, the equilibrium distribution $f^0(\mathbf{v})$ is given by the Maxwell-Boltzmann equation:

$$f^0(\mathbf{v}) = \frac{\rho}{(2\pi T)^{2/3}} e^{-(v-u)^2/2T} \quad \text{, where } \mathbf{v} \text{ is continuous} \tag{2.9}$$

and T is the temperature (assumed to be constant). However in LB, the particles' velocities are discretized: $\{\mathbf{v}_0, \mathbf{v}_1, \ldots, \mathbf{v}_{14}\}$. In this case, we use a polynomial expansion in $\mathbf{v}_i$ and $\mathbf{u}$ to approximate the Maxwell-Boltzmann distribution above. The expression for f_i^0 is then given by [44, 46]:

$$\begin{aligned} f^0(\mathbf{v}_i) &= A_i + B_i \mathbf{u} \cdot \mathbf{v}_i + C_i u^2 + D_i \mathbf{u}\mathbf{u} : \mathbf{v}_i\mathbf{v}_i + \underline{\underline{E}}_i : \mathbf{v}_i\mathbf{v}_i \\ &\quad \text{, for } i = 1, 2, \ldots, 14. \end{aligned} \tag{2.10}$$

The exact expressions for the coefficients A, B, ... and E can be found in Ref. [5]. Using Chapman-Enskog expansion [48], the Navier-Stokes equation (2.1) can be recovered from the LB equation with the macroscopic viscosity related to the mesoscopic timescale *via* $\eta = \frac{1}{3}(\tau - \frac{1}{2})$. Note that in actual lattice Boltzmann simulations, the fluid becomes slightly compressible (density fluctuations of up to 5% is expected[1]).

Finally, the equation for the order parameter can be solved numerically using the explicit Euler scheme (hence the hybrid part):

$$\phi(\mathbf{x}, t + \Delta t) = \phi(\mathbf{x}, t) + \Delta t \left[-(\mathbf{u} \cdot \nabla)\phi - \frac{\delta F}{\delta \phi}\right] \tag{2.11}$$

[1]The lattice Boltzmann equation also effectively solves the continuity equation: $\frac{\partial \rho}{\partial t} + \nabla \cdot (\rho \mathbf{u}) = 0$. See Ref. [45] for more detail.

with the gradient operators replaced with the appropriate lattice equivalents, for instance $\frac{\partial \phi}{\partial x} = \frac{\phi(x+\Delta x)-\phi(x-\Delta x)}{2\Delta x}$ (also see Ref. [49] for more detail). In this case, we do not need another LB scheme to solve the order parameter because there is no constraint such as the incompressibility condition (2.2) to worry about. However when simulating two fluids of different viscosities, we may then need two LB schemes (one for each fluid phase) with two different relaxation timescales τ's corresponding to the respective fluid viscosities [44][2]. Note that in our droplet simulations in chapter 4 and 5, we assume the fluid viscosity inside the droplet to be equal to that outside, thus avoiding the need for solving two LB equations.

2.2 Equations of motion for the order parameters

Some of the order parameters that we may encounter in this thesis are: (i) the concentration of the particles $c(\mathbf{r}, t)$ (which is a scalar), (ii) the average polar orientations of the particles $\mathbf{p}(\mathbf{r}, t)$ (a vector) and (iii) the nematic order parameter $\underline{\underline{\mathbf{Q}}}(\mathbf{r}, t)$ (a rank-2 tensor). The equations of motion for these hydrodynamic fields are similar to Eqn. (2.3), except for c which is a conserved field, in which case, the equation of motion has the form of a continuity equation:

$$\frac{\partial c}{\partial t} + \nabla \cdot (c\mathbf{u} - \nabla \frac{\delta F}{\delta c}) = 0 \tag{2.12}$$

This will be discussed further in subsequent chapters.

2.3 Boundary conditions at the walls

We typically perform this lattice Boltzmann simulation in a box of $L_x \times L_y \times L_z$ lattice sites. (For 2D simulations, one can set $L_z = 1$.) The simplest boundary condition is to have periodic boundary conditions on all six sides of the box. However in some simulations, we may also want to have solid walls at $z = 0$ and $z = L_z$. The appropriate boundary conditions for the fluid at these walls are

[2]Alternatively, one can also have a timescale τ which depends on the composition variable of the two fluids. This will only work if the variation in τ (and hence in η) is not too large ($< 10\%$).

discussed below.

Non-slip BC

Suppose we have a wall at $z = 0$. The most common boundary condition for $\mathbf{u}$ is the non-slip condition or,

$$\mathbf{u}(z = 0) = 0 \tag{2.13}$$

Substituting this equation to Eqn. (2.7), we then have, for f_i's,

$$\sum_i f_i \mathbf{v}_i = 0 \quad , \text{ at } z = 0$$

Equating the z-component, we have:

$$f_5 + f_7 + f_8 + f_9 + f_{10} - f_6 - f_{11} - f_{12} - f_{13} - f_{14} = 0$$

and equating the x-component, we have:

$$f_1 + f_7 + f_{10} + f_{11} + f_{14} - f_3 - f_8 - f_9 - f_{12} - f_{13} = 0$$

and finally equating the y-component, we have:

$$f_2 + f_7 + f_8 + f_{11} + f_{12} - f_4 - f_9 - f_{10} - f_{13} - f_{14} = 0$$

At the wall $z = 0$, we have five unknown distributions f_5, f_7, f_8, f_9 and f_{10} (referring back to Fig. 2.1) but we only have three equations given above. We therefore need two more equations which can be chosen arbitrarily. One choice is based on symmetry and they are given by [5]:

$$\begin{aligned} f_7 - f_8 &= f_{10} - f_9 \\ f_5 &= f_6 \end{aligned}$$

The solution to the equations above gives us the equivalent non-slip boundary condition for f_i's:

$$\begin{aligned} f_5 &= f_6 \\ f_7 &= \frac{1}{4}(-f_1 - f_2 + f_3 + f_4 - f_{11} + f_{12} + 3f_{13} + f_{14}) \\ f_8 &= \frac{1}{4}(f_1 - f_2 - f_3 + f_4 + f_{11} - f_{12} + f_{13} + 3f_{14}) \\ f_9 &= \frac{1}{4}(f_1 + f_2 - f_3 - f_4 + 3f_{11} + f_{12} - f_{13} + f_{14}) \\ f_{10} &= \frac{1}{4}(-f_1 + f_2 + f_3 - f_4 + f_{11} + 3f_{12} + f_{13} - f_{14}) \end{aligned} \tag{2.14}$$

The boundary conditions on f_i's can be implemented in the following ways. First we update the particles' distributions at every lattice point (including the ones at the wall) using the LB equation in (2.8). And then we change the values of f_5, f_6, f_7, f_8, f_9 and f_{10} at the walls using the boundary equations above so that the sum $\sum_i f_i \mathbf{v}_i$ becomes zero at the walls.

Full-slip BC

For full-slip boundary condition at $z = 0$, we have instead:

$$\begin{aligned} u_z(z=0) &= 0 \\ \left.\frac{\partial u_{x,y}}{\partial z}\right|_{z=0} = u'_{x,y}(z=0) &= 0 \end{aligned} \tag{2.15}$$

The easiest way to apply this boundary condition on f_i's is to reverse the signs of the x- and y- axes in Fig. 2.1 and thus f_1 becomes f_3, f_{11} becomes f_{13}, *etc.* We do this for the right hand sides of Eqns. (2.14) and the result is the full slip

BC for the distribution functions f_i's at $z = 0$:

$$\begin{aligned} f_5 &= f_6 \\ f_7 &= \frac{1}{4}(f_1 + f_2 - f_3 - f_4 + 3f_{11} + f_{12} - f_{13} + f_{14}) \\ f_8 &= \frac{1}{4}(-f_1 + f_2 + f_3 - f_4 + f_{11} + 3f_{12} + f_{13} - f_{14}) \\ f_9 &= \frac{1}{4}(-f_1 - f_2 + f_3 + f_4 - f_{11} + f_{12} + 3f_{13} + f_{14}) \\ f_{10} &= \frac{1}{4}(+f_1 - f_2 - f_3 + f_4 + f_{11} - f_{12} + f_{13} + 3f_{14}) \end{aligned} \tag{2.16}$$

Partial slip BC

Finally in chapter 4, we shall also use a mixture of non-slip and full-slip BC. The partial-slip BC can be defined mathematically to be (see Wolff *et al.* [50]):

$$\begin{aligned} u_z(z = 0) &= 0 \\ \frac{u_{x,y}(z = 0)}{u'_{x,y}(z = 0)} &= 3\eta\frac{s}{1 - s} \end{aligned} \tag{2.17}$$

where s is the slip parameter describing the amount of slip at the wall. η is the shear viscosity which originates from the relaxation timescale τ in the collision operator. s is also defined such that $s = 0$ corresponds to non-slip and $s = 1$ corresponds to full-slip. Finally, the boundary condition for f_i's at the wall can be

obtained by combining Eqn. (2.14) and Eqn. (2.16) with the appropriate weights:

$$\begin{aligned}
f_5 &= f_6 \\
f_7 &= \frac{1-s}{4}(-f_1 - f_2 + f_3 + f_4 - f_{11} + f_{12} + 3f_{13} + f_{14}) \\
&\quad + \frac{s}{4}(f_1 + f_2 - f_3 - f_4 + 3f_{11} + f_{12} - f_{13} + f_{14}) \\
f_8 &= \frac{1-s}{4}(f_1 - f_2 - f_3 + f_4 + f_{11} - f_{12} + f_{13} + 3f_{14}) \\
&\quad + \frac{s}{4}(-f_1 + f_2 + f_3 - f_4 + f_{11} + 3f_{12} + f_{13} - f_{14}) \\
f_9 &= \frac{1-s}{4}(f_1 + f_2 - f_3 - f_4 + 3f_{11} + f_{12} - f_{13} + f_{14}) \\
&\quad + \frac{s}{4}(-f_1 - f_2 + f_3 + f_4 - f_{11} + f_{12} + 3f_{13} + f_{14}) \\
f_{10} &= \frac{1-s}{4}(-f_1 + f_2 + f_3 - f_4 + f_{11} + 3f_{12} + f_{13} - f_{14}) \\
&\quad + \frac{s}{4}(+f_1 - f_2 - f_3 + f_4 + f_{11} - f_{12} + f_{13} + 3f_{14})
\end{aligned} \tag{2.18}$$

Eqn. 2.18 can then be obtained from the boundary conditions above (see derivation in [50]).

Boundary conditions for the order parameters

The boundary conditions for an order parameter at the walls vary and depend on whether it is a scalar or a vector. In the case of a scalar order parameter such as c, the obvious boundary condition is the no-flux condition, defined such that the concentration current across the wall is zero (as expected):

$$j_z(z = 0) = 0 \tag{2.19}$$

where the wall is located at $z = 0$. However, this condition alone is often not enough and one needs to supplement this boundary condition with a wetting condition which will be discussed in chapter 4.

In the case of a vector order parameter such as the polarisation $\mathbf{p}$, the boundary condition for $\mathbf{p}$ is normally a strong anchoring condition with $\mathbf{p}$ aligned parallel to the walls or perpendicularly to the walls or at some fixed angle to the walls [35]. In the case of bacterial swimmers, it is commonly observed that they always swim parallel next to a wall [51, 52] and thus the appropriate boundary

condition for $\mathbf{p}$ is the parallel anchoring:

$$\begin{aligned} p_z(z=0) &= 0 \\ \frac{\partial p_{x,y}}{\partial z}(z=0) &= 0 \end{aligned} \tag{2.20}$$

In the case of actomyosin solutions, the actin filaments can also be assumed to be anchored parallel to the walls due to focal adhesions (see chapter 4) and thus the boundary equations above still apply to actomyosin systems.

Chapter 3

Nonequilibrium steady states in bacterial suspensions

In this chapter, we are going to study our first example of active fluids (*i.e.* bacterial suspensions) in more detail. As described in the introduction, bacterial suspension constitutes an active fluid because the bacteria continuously stir the fluid as they move around. This swimming motion is typically driven by the flagella rotation at the back (see Fig. 3.1(A)), and consequently, bacteria are also shown to be extensile swimmers with the direction of the dipolar force shown by red arrows in Fig. 3.1(A). (This has also been shown experimentally by Goldstein *et al.* [2], see Fig. 1.2(C) in the introduction.) Note that not all microscopic swimmers are extensile. For example *Chlamydomonas*, a type of algae, is a contractile swimmer. This is because the flagella (or rather the *cilia*) are located at the head rather than at the back and the cilia stroke pulls the swimmer from the front. The resulting dipolar force is then opposite to that of bacteria, *i.e.* contractile (see Fig. 3.1(B)). Finally bacteria are also polar, with the direction of polarity defined by the swimming direction, and in high concentration, these bacteria often align themselves to swim together in the same direction (macroscopic polar orientational order).

Here, we are going to focus mainly on extensile polar fluids as a simple model of dense bacterial suspensions. More specifically, we are going to study hydrodynamic instabilities and non-equilibrium steady states (NESS) in polar active fluids. First we are going to consider extensile polar fluid without swimming (*i.e.* shakers) but later we are going to generalize this to

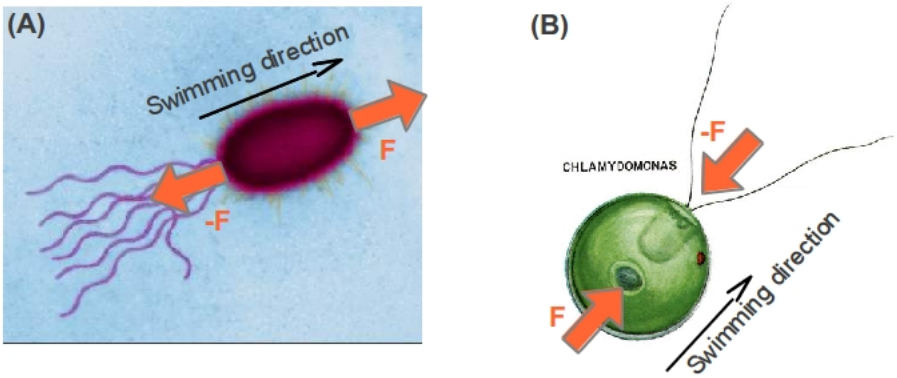

Figure 3.1: Some examples of microscopic swimmers. The red arrows indicate the forces exerted by the swimmer on the surrounding fluid. In **(A)**, we have an example of extensile swimmer (*E. Coli*, a type of bacteria). The flagella at the back of the swimmer pushes the swimmer forward. In **(B)**, we have an example of contractile swimmer (a type of algae called *Chlamydomonas*). Here, the flagella is located at the head and the swimmer is pulled by the flagella to swim in the direction indicated. (Images taken from `www.scientificamerican.com` and `www.botany.hawaii.edu`.)

extensile swimmers as well. As in many examples of hydrodynamic instabilities, the unstable system often undergoes a non-equilibrium phase transition to a steady flow state, oscillatory state, or in extreme cases, chaotic flow resembling turbulence (as can be seen in many bacteria). We are also going to learn how this non-equilibrium phase transition can be characterised.

3.1 Why hydrodynamics?

Suppose we have a collection of N microscopic swimmers (*e.g.* bacteria) suspended in a viscous fluid. Let us denote the centre of mass positions to be: $\{\mathbf{r}_1, \mathbf{r}_2, \ldots, \mathbf{r}_N\}$. Since these swimmers are also *polar*, we denote their orientations by the unit vectors: $\{\hat{\nu}_1, \hat{\nu}_2, \ldots, \hat{\nu}_N\}$. Assuming they are all swimming with the same speed relative to the solvent, the velocities of the swimmers are then given by: $\mathbf{v}_i = w\hat{\nu}_i$, where $w = constant$ is the swimming speed.

In principle, it is possible to simulate the dynamics of N swimmers by solving

the positions and velocities of the particles as follows (see Vicsek *et al.* [7]):

$$\begin{aligned} \mathbf{r}_i(t+\Delta t) &= \mathbf{r}_i(t) + \mathbf{v}_i(t)\Delta t \\ \hat{\nu}_i(t+\Delta t) &= \underline{\underline{\mathbf{R}}}_i \cdot \hat{\nu}_i(t) \end{aligned} \tag{3.1}$$

where $\underline{\underline{\mathbf{R}}}_i$ is a rotational operator which tends to align the swimmers parallel to each other - the rule of which is given in more details in [7]. However as discussed in the introduction, a swimming bacterium is also effectively a force dipole and creates a quadrupolar fluid flow around the swimmer. This fluid flow can in turn affect the motion of another swimmer at some distance away. So the equations above are not yet complete as one also has to add hydrodynamic interaction by solving the fluid velocity $\mathbf{u}(\mathbf{r})$ and replacing $\mathbf{v}_i(t) \to \mathbf{v}_i(t) + \mathbf{u}(\mathbf{r}_i(t))$ in equation (3.1). The microscopic dynamics of $N \sim 1000$ swimmers with hydrodynamic interaction has been studied extensively in Nash *et al.* [53, 54].

While the microscopic picture of bacterial suspension can be useful (to study the emergence of orientational order for instance), in this thesis we shall adopt an even simpler approach. Rather than solving $6N$ microscopic variables: $\{(\mathbf{r}_1, \hat{\nu}_1), (\mathbf{r}_2, \hat{\nu}_2), \ldots, (\mathbf{r}_N, \hat{\nu}_N)\}$ plus a fluid velocity $\mathbf{u}(\mathbf{r})$ directly; we are going to solve only a few coarse-grained fields. Each of these coarse-grained/hydrodynamic fields is a continuum variable of time t and position $\mathbf{r}$. Note that in our computer simulations, the time itself is discretized and the position vector $\mathbf{r}$ is confined to a d-dimensional lattice. This approach allows us to study the dynamics of bacterial suspension (or indeed any kinds of active fluids) at a much longer lengthscales. For example, we may be interested in how macroscopic fluid vortices arise in active fluids.

The first hydrodynamic field of interest is the concentration of the swimmers, which is related to the microscopic variables via [55]:

$$\underbrace{c(\mathbf{r},t)}_{coarse-grained} = \left\langle \sum_{i=1}^{N} \delta(\mathbf{r} - \underbrace{\mathbf{r}_i(t)}_{microscopic}) \right\rangle \tag{3.2}$$

where the angle bracket denotes a local average. The other coarse-grained fields that we need to solve are the order parameters which are defined microscopically

to be:

$$\mathbf{p}(\mathbf{r},t) = \frac{1}{c(\mathbf{r},t)}\left\langle \sum_{i=1}^{N} \hat{\nu}_i(t)\delta(\mathbf{r}-\mathbf{r}_i(t))\right\rangle \tag{3.3}$$

$$\underline{\underline{\mathbf{Q}}}(\mathbf{r},t) = \frac{1}{c(\mathbf{r},t)}\left\langle \sum_{i=1}^{N} \left(\hat{\nu}_i(t)\hat{\nu}_i(t) - \frac{1}{3}\underline{\underline{\mathbf{I}}}\right)\delta(\mathbf{r}-\mathbf{r}_i(t))\right\rangle \tag{3.4}$$

Physically $\mathbf{p}$ measures the average polar orientation of the swimmers and $\underline{\underline{\mathbf{Q}}}$ measures the degree of nematic order (discussed below). The above relations connect the coarse-grained fields to their relevant microscopic variables. Actually we are going to use these relations only once (in the derivation of the active stress below) since most equations for the coarse-grained fields can be derived phenomenologically.

3.1.1 Orientational order in bacterial suspension

As suggested in the introduction, bacterial suspensions often show some degrees of orientational order at high density. This is demonstrated in the experiment of Cisneros *et al.* [56] where they studied a dense suspension of swimming bacteria (*B. subtilis*). In this microscopy-based experiment, they divide the system into a grid of $18.9\,\mu\text{m} \times 18.9\,\mu\text{m}$ square cells, and in each cell, the average polar orientation of the swimming bacteria is measured. Strictly speaking, they only measured the magnitude of the polar order parameter $|\mathbf{p}|$, defined such that $|\mathbf{p}| = 1$ corresponds to perfect polar order while $|\mathbf{p}| = 0$ corresponds to disordered or possibly nematic state (see Fig. 3.2 for the definition of nematic and polar order). In line with previous experiments by Weibel *et al.* [1], Cisneros *et al.* also observed domains of large $|\mathbf{p}|$ in which the bacteria can be found to be swimming together in the same direction. However these domains are often short-lived as they spontaneously form, disaggregate and re-form somewhere else, almost like chaotic/turbulent motion. Other types of bacterial suspensions (such as *P. mirabilis*, shown in Fig. 1.2(A) in the introduction) has polar domains which are more stable and do not break up as often as *B. subtilis*. What happens instead, the direction (not the magnitude) of the polarisation $\mathbf{p}$ is evolving rather slowly. The latter case in particular is perhaps more relevant to us since our model only accounts for a slow dynamics in $\mathbf{p}$.

	Isotropic	**Nematic**	**Polar**
	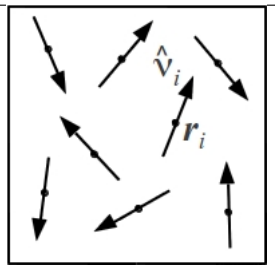	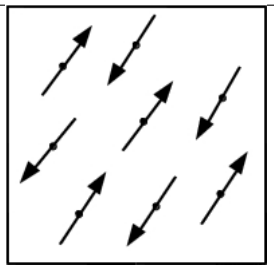	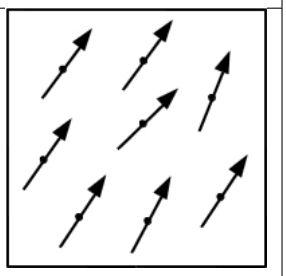
Symmetry:	Invariant under any arbitrary rotation	Invariant under 180° rotation	No symmetry
Order parameters:	$\mathbf{p} = 0$ $\underline{\underline{\mathbf{Q}}} = 0$	$\mathbf{p} = 0$ $\underline{\underline{\mathbf{Q}}} \neq 0$	$\mathbf{p} \neq 0$ $\underline{\underline{\mathbf{Q}}} \neq 0$

Figure 3.2: Orientational order in a suspension of microscopic swimmers. Depending on various parameter (such as density and temperature), a collection of polar active particles in some mesoscopic volume dV can be found in one of three states: isotropic, nematic, or polar.

Other than that, Cisneros *et al.* measured that $|\mathbf{p}|$ (or the degree of polar order) also depends on the swimming speed as well as the density of the bacteria in the cell. This suggests a non-equilibrium nature of disordered to ordered phase transition in bacterial suspensions. We are going to discuss this more a bit later but first we are going to give some definitions of orientational order.

More generally a collection of N polar particles (either swimming or not) in some mesoscopic volume dV can be found in any one of these three states: isotropic, nematic, or polar (see Fig. 3.2). In the isotropic state, the system is invariant under any arbitrary rotation on all particles in the subvolume dV:

$$\hat{\nu}_i \to \underline{\underline{\mathbf{R}}} \cdot \hat{\nu}_i \quad \text{, for all } i$$

and consequently $\mathbf{p}$ and $\underline{\underline{\mathbf{Q}}}$ have to be zero. On the other hand in the nematic state, the system is invariant under 180° rotation:

$$\hat{\nu}_i \to -\hat{\nu}_i \quad \text{, for all } i$$

and therefore $\underline{\underline{\mathbf{Q}}}$ has to be finite while $\mathbf{p}$ remains zero. Lastly in the polar state, the system does not have any rotational symmetry and correspondingly $\underline{\underline{\mathbf{Q}}}$ and $\mathbf{p}$ are finite.

3.1.2 How does a bacterial suspension acquire polarity?

Experimental results of Cisneros *et al.* suggest a non-equilibrium phase transition from disordered to ordered state in a bacterial suspension which can be understood as a two-step process as follows. First, a bacterial suspension may undergo an equilibrium phase transition from isotropic/disordered to nematic state as the density of the bacteria is increased. This happens because the bacteria (being rod-like particles) have to align themselves in order to minimise the space in between as the density is increased (excluded volume interaction, see Fig. 3.3(A)). And therefore in a densely packed suspension, the bacteria are either aligned parallel or anti-parallel to each other (nematic state, see Fig. 3.3(A) right).

Secondly the nematic state in bacterial suspension is unstable with respect to self-propulsion/swimming of the individual bacterium. This is illustrated in Fig. 3.3(B). From the figure, we initially have one single domain of bacteria in nematic state. Inside this domain there is an equal number of bacteria pointing to the left and bacteria pointing to the right. As we increase the swimming speed, the left-pointing bacteria will swim to the left while the right-pointing bacteria will swim to the right and this leads to a phase separation into two domains of opposite polarity. We therefore expect a non-equilibrium phase transition from nematic to polar order with increasing swimming speed.

Preliminary numerical results also appear to support the existence of nematic-to-polar transition at certain critical swimming speed. These numerical simulations were performed by solving the dynamics of $\mathbf{p}(\mathbf{r}, t)$ and $\underline{\underline{\mathbf{Q}}}(\mathbf{r}, t)$; the equations of which are given in more details in appendix A. Fig. 3.3(C) shows one such simulation of nematic-to-polar transition in a droplet of bacterial suspension.

3.1.3 Hydrodynamic equations

The hydrodynamic equations of the coarse-grained fields (such as the concentration and the order parameters) can be derived in several ways. One way is to derive these equations directly from the microscopic dynamics using the connection formulas (3.2-3.4) as done in Marchetti *et al.* [28]. Or alternatively, we can also derive these equations phenomenologically by considering the symmetries of the system as done in Ramaswamy *et al.* [4] and Julicher *et al.* [57] as well as

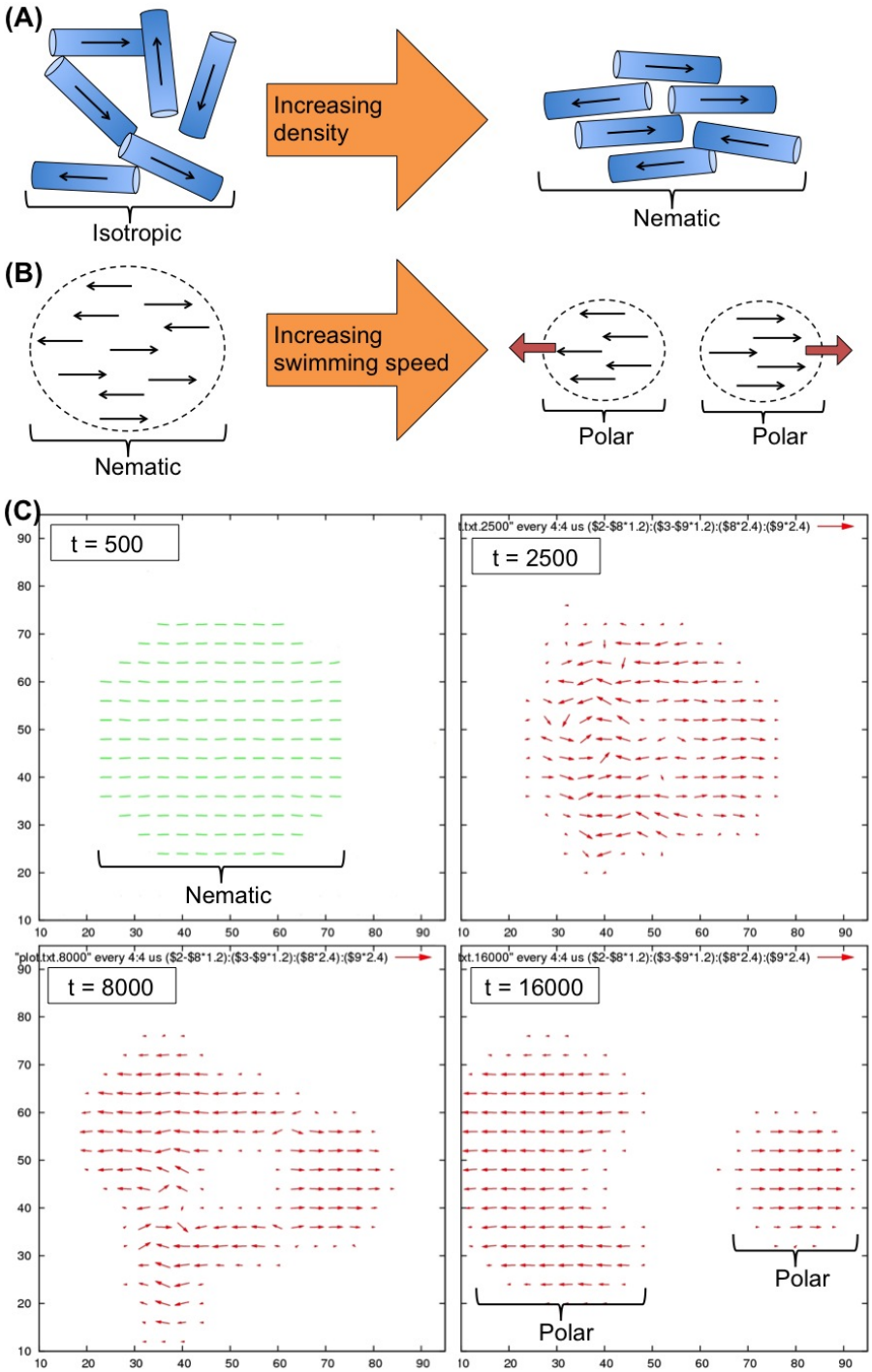

Figure 3.3: **(A)** Equilibrium phase transition from isotropic to nematic state in bacterial suspensions which can be understood due to excluded volume interaction. **(B)** Non-equilibrium phase transition from nematic to polar order is observed at large enough swimming speed. Furthermore, such transition is accompanied by phase separation due to bacteria swimming in opposite directions. **(C)** A simulated non-equilibrium nematic-to-polar phase-separation in a droplet of bacterial suspension.

in this thesis.

We are now going to focus on a specific case of polar active particle suspension in polar phase. Note that we assume the system to be homogenously in polar state - we are not considering isotropic/nematic/polar transition. In this case, the only hydrodynamic fields relevant to us are just c and $\mathbf{p}$ (and the fluid velocity $\mathbf{u}$). To describe the dynamics of c and $\mathbf{p}$ close to equilibrium, we construct the free energy functional as follows:

$$F[c,\mathbf{p}] = \int dV \left\{ \frac{B}{2}(c-c_0)^2 - \frac{a}{2}\left|\mathbf{p}\right|^2 + \frac{b}{4}\left|\mathbf{p}\right|^4 + \frac{\kappa}{2}(\nabla\mathbf{p})^2 \right\} \tag{3.5}$$

where c_0 is the average concentration of the particles and B is the compressional modulus. Here we have assumed that the number density fluctuation is small ($\frac{c-c_0}{c_0} \ll 1$). The terms proportional to $\left|\mathbf{p}\right|^2$ and $\left|\mathbf{p}\right|^4$ are the Landau potential terms which describe equilibrium isotropic-to-polar transition in bacterial suspensions. a and b are the corresponding phenomenological parameters which are taken to be equal and positive ($a = b > 0$) so that the minimum of this Landau terms is at $|\mathbf{p}| = 1$ (corresponding to the polar phase). Finally the term proportional to $(\nabla\mathbf{p})^2$ describes the energy penalty associated with elastic deformations (such as bend, splay and twist) in the $\mathbf{p}$-field. κ is the associated elastic constant. In general, one can have three different elastic constants κ_i's associated with bend, splay and twist deformations in the liquid crystalline phase [35]. However in many cases of passive liquid crystals [35], the values of these three elastic constants are often close to each other so we may assume they are all equal (single elastic constant approximation, $\kappa_{bend} = \kappa_{splay} = \kappa_{twist} = \kappa$). For our bacterial suspensions (and also for the actomyosin systems in the next chapters), we shall also assume single elastic constant approximation for simplicity.

Assuming the bacteria do not reproduce or die on the experimental timescale, the concentration of the swimmers $c(\mathbf{r},t)$ can then be assumed to be conserved. The dynamics of c thus follows the continuity equation:

$$\frac{\partial c}{\partial t} + \nabla\cdot\mathbf{j} = 0 \tag{3.6}$$

where $\mathbf{j}$ is the concentration current which has the following form:

$$\mathbf{j} = \underbrace{c(\mathbf{u} + w\mathbf{p})}_{\text{convective current}} \underbrace{-M\nabla\frac{\delta F}{\delta c}}_{\text{diffusive current}}$$

There are two contributions to the current: convection and diffusion. As well as convected by the velocity of the fluid solvent $\mathbf{u}$, the particles can also swim with velocity $w\mathbf{p}$ relative to the solvent. Here $w \geq 0$ is a nonequilibrium parameter which tends to force the system out of equilibrium (if its value is not zero). (Note that the swimming velocity $w\mathbf{p}$ is a local average over all the particles which are not always perfectly aligned in the same direction.) Finally the convective current is thus equal to $c(\mathbf{u} + w\mathbf{p})$. The second contribution to the current is due to passive diffusion of particles from regions of high chemical potential to regions of low chemical potential. The diffusive current can thus be written as a gradient of the chemical potential: $-M\nabla\frac{\delta F}{\delta c}$, with the proportionality constant M (also called mobility). From the free energy functional (3.5), the chemical potential is worked out to be: $\frac{\delta F}{\delta c} = B(c - c_0)$. Thus we may also relate the mobility M to the diffusion constant D *via* $D = MB$. In particular, since we have been using bacterial suspension as an example of polar active fluid, we may relate this diffusion constant (assumed to be density-independent) to that of run-and-tumble motion of bacteria [58, 23].

The dynamics of dense bacterial suspension in the polar phase is very similar to that of liquid crystals (at least in equilibrium limit). Consequently, the time-evolution of the polarisation field $\mathbf{p}(\mathbf{r}, t)$ can be modelled to follow closely that of the director field in liquid crystals [29, 59, 35].

$$\frac{\partial \mathbf{p}}{\partial t} + (\mathbf{u} + w\mathbf{p}) \cdot \nabla\mathbf{p} = -\underline{\underline{\Omega}} \cdot \mathbf{p} + \xi\underline{\underline{v}} \cdot \mathbf{p} - \frac{1}{\Gamma}\frac{\delta F}{\delta \mathbf{p}} \tag{3.7}$$

The only difference with standard liquid crystals equation is the nonequilibrium term $\sim w\mathbf{p}$ appearing on the left hand side of the equation to signify particles' swimming along the direction of $\mathbf{p}$. $\underline{\underline{v}}$ and $\underline{\underline{\Omega}}$ in the equation above are the

symmetric and anti-symmetric parts of the velocity gradient tensor $\nabla\mathbf{u}$:

$$\begin{aligned} \underline{\underline{v}} &= \frac{1}{2}\left[(\nabla\mathbf{u}) + (\nabla\mathbf{u})^T\right] \\ \underline{\underline{\Omega}} &= \frac{1}{2}\left[(\nabla\mathbf{u}) - (\nabla\mathbf{u})^T\right] \end{aligned} \tag{3.8}$$

The parameter ξ (dimensionless) is related to the geometry of the active polar particles: $\xi > 0$ for rod-like particles and $\xi < 0$ for oblate particles. ξ also tells us whether the particle tends to align to a shear flow ($|\xi| > 1$) or tumble as in red blood cells ($|\xi| < 1$). In the case of bacterial suspension, we choose ξ to be in the flow-aligning regime and positive (for rod-shape). Finally, Γ is a relaxational constant related to the rotational viscosity of the liquid crystals. Basically terms proportional to $\frac{\delta F}{\delta c}$ and $\frac{\delta F}{\delta \mathbf{p}}$ in Eqns. (3.6) and (3.7) tend to relax the system towards the free energy minimum, *i.e.* towards equilibrium, whereas active terms such as the swimming speed w and the dipolar force ζ tend to force the system away from the free energy minimum, *i.e.* out of equilibrium. (Note that ζ is another active/nonequilibrium parameter which will be explained shortly.) Consequently, such active terms cannot be written as a derivative of the free energy functional. Other than being driven out of equilibrium internally through w and ζ, the system can also be forced out of equilibrium externally by imposing an external shear. In fact, we will look at the effect of an external shear on active fluids in section 3.3.3.

As an aside, Eqn. 3.7 can also be written in a more familiar form as (see Bray [42]):

$$\frac{D\mathbf{p}}{Dt} = -\frac{\delta F}{\delta \mathbf{p}} \tag{3.9}$$

where $\frac{D}{Dt}$ is the material derivative or the time derivative taken as one follows the trajectory of the particles. In contrast, $\frac{\partial}{\partial t}$ is the time derivative of some coarse grained field taken at a fixed position in space. In this case, the material derivative has the form:

$$\frac{D}{Dt} = \frac{\partial}{\partial t} + (\mathbf{u} + w\mathbf{p}) \cdot \nabla + \underline{\underline{\Omega}} \cdot - \xi \underline{\underline{v}} \cdot \tag{3.10}$$

(see Appendix B for further discussion about the roles of $\underline{\underline{v}}$ and $\underline{\underline{\Omega}}$).

Finally the fluid velocity $\mathbf{u}(\mathbf{r}, t)$ must satisfy the momentum balance equation

(Navier-Stokes):

$$\rho\left\{\frac{\partial}{\partial t}+\mathbf{u}\cdot\nabla\right\}\mathbf{u}=-\nabla P+\eta\nabla^2\mathbf{u}+\nabla\cdot\underline{\underline{\sigma}}^p+\nabla\cdot\underline{\underline{\sigma}}^a \tag{3.11}$$

plus the incompressibility condition:

$$\nabla\cdot\mathbf{u}=0 \tag{3.12}$$

There are two contributions to the hydrodynamic stress: passive stress ($\underline{\underline{\sigma}}^p$) due to the elastic deformation of the liquid crystalline phase and active stress ($\underline{\underline{\sigma}}^a$) due the permanent force dipole in each particle. The form of the passive stress is well known in liquid crystals literature [35]:

$$\sigma^p_{\alpha\beta}=\frac{1}{2}\left(p_\alpha h_\beta-p_\beta h_\alpha\right)-\frac{\xi}{2}\left(p_\alpha h_\beta+p_\beta h_\alpha\right)-k\partial_\alpha p_\gamma\partial_\beta p_\gamma \tag{3.13}$$

where $\mathbf{h}=-\frac{\delta F}{\delta\mathbf{p}}$ is the molecular field. The Greek alphabets, throughout this thesis, represent the Cartesian coordinates and we have adopted the Einstein summation convention. The active stress (derived below) has the form:

$$\sigma^a_{\alpha\beta}=-\zeta c p_\alpha p_\beta \tag{3.14}$$

where ζ is another activity parameter proportional to the strength of the force dipoles (see below for more details).

3.1.4 Derivation of the active stress

We shall now derive the expression for the active stress $\underline{\underline{\sigma}}^a$ exerted by the active particles on the fluid solvent. Note that this term is the non-equilibrium part of the momentum balance equation in Eqn. (3.11). Following the derivation of Ramaswamy *et al.* [4], we first consider the force density acting on the fluid solvent due to a single force dipole of magnitude F (see Fig. 3.4(A)). This force density can be written as:

$$\mathbf{f}_i(\mathbf{r})=+F\hat{\nu}_i\delta(\mathbf{r}-\mathbf{r}_i-\frac{l}{2}\hat{\nu}_i)-F\hat{\nu}_i\delta(\mathbf{r}-\mathbf{r}_i+\frac{l}{2}\hat{\nu}_i)$$

where $\hat{\nu}_i$ is the polarity, $\mathbf{r}_i$ is the centre of mass and l is the size the active particle. We have also assumed that the centre of mass $\mathbf{r}_i$ is equidistant from the two point forces (see Fig. 3.4(A)).

The force density due to a collection of force dipoles is then given by:

$$\mathbf{f}(\mathbf{r}) = \left\langle \sum_i \left\{ +F\hat{\nu}_i \delta(\mathbf{r} - \mathbf{r}_i - \frac{l}{2}\hat{\nu}_i) - F\hat{\nu}_i \delta(\mathbf{r} - \mathbf{r}_i + \frac{l}{2}\hat{\nu}_i) \right\} \right\rangle$$

with the angle bracket representing a coarse grained average. To proceed, we Taylor-expand the delta function as follows:

$$\delta(\mathbf{r} - \mathbf{r}_i \pm \frac{l}{2}\hat{\nu}_i) = \delta(\mathbf{r} - \mathbf{r}_i) \pm \frac{l}{2}\hat{\nu}_i \cdot \nabla\delta(\mathbf{r} - \mathbf{r}_i) + O(l^2\nabla^2)$$

Note that l has a microscopic lengthscale whereas ∇ has an inverse macroscopic lengthscale and thus $l\nabla$ is a small parameter in the Taylor expansion above. Substituting the Taylor expansion of the delta function into the equation of $\mathbf{f}(\mathbf{r})$, we have:

$$\begin{aligned} \mathbf{f}(\mathbf{r}) &= \nabla \cdot \left\langle -Fl \sum_i \hat{\nu}_i \hat{\nu}_i \delta(\mathbf{r} - \mathbf{r}_i) + O(\nabla^2) \right\rangle \\ &= \nabla \cdot \left\{ -Flc \left(\underline{\underline{\mathbf{Q}}} + \frac{1}{3}\underline{\underline{\mathbf{I}}} \right) + O(\nabla^2) \right\} \end{aligned}$$

where we have used the microscopic definition of $\underline{\underline{\mathbf{Q}}}$ (see Eqn. 3.4). Therefore we identify the active stress to be:

$$\underline{\underline{\sigma}}^a = -\zeta c \left(\underline{\underline{\mathbf{Q}}} + \frac{1}{3}\underline{\underline{\mathbf{I}}} \right) + O(\nabla^2) \tag{3.15}$$

where $\zeta = Fl$ is the activity parameter proportional to the strength of the force dipoles. $\zeta > 0$ indicates extensile while $\zeta < 0$ indicates contractile.

For a uniaxial body, we can write $\underline{\underline{\mathbf{Q}}}$ as

$$\underline{\underline{\mathbf{Q}}} = S \left(\hat{n}\hat{n} - \frac{1}{3}\underline{\underline{\mathbf{I}}} \right)$$

where $\hat{n}$ is the largest (normalised) eigenvector of $\underline{\underline{\mathbf{Q}}}$ and S is the eigenvalue (also the degree of nematic order). In polar phase, $\mathbf{p}$ is usually aligned parallel to the

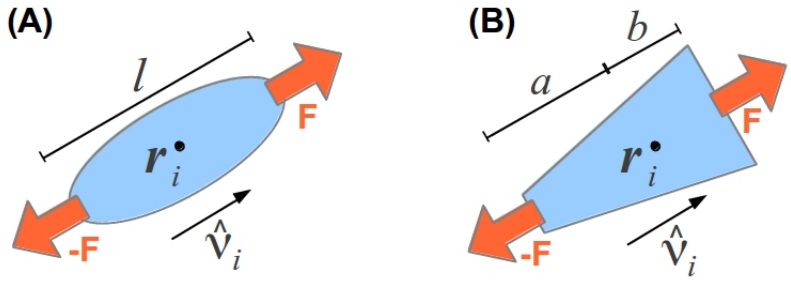

Figure 3.4: Geometry of the force dipole considered in the derivation of the active stress (see main text). **(A)** Here the shape of the active particle is symmetric about its midpoint and the centre of mass $\mathbf{r}_i$ is equidistant from the two point forces. $\hat{\nu}_i$ is the orientation of the active particle (also the direction of swimming in the case of movers). **(B)** Here we have an example of an asymmetric particle where the centre of mass $\mathbf{r}_i$ is no at the middle of the two point forces.

director field $\hat{n}$ so that the dynamics of $\underline{\underline{\mathbf{Q}}}$ becomes redundant (see appendix A). In this case, we can rewrite the formula for the active stress above (3.15) in terms of $\mathbf{p}$:

$$\underline{\underline{\sigma}}^a = -\zeta c \mathbf{pp} + O(\nabla^2) \tag{3.16}$$

where we have approximated $\underline{\underline{\mathbf{Q}}} \simeq S(\mathbf{pp} - \underline{\underline{\mathbf{I}}}/3)$ since $\mathbf{p}$ will saturate to point either parallel or anti-parallel to the director field $\hat{n}$ (except when the system is close to nematic-polar transition, see appendix A). Note that terms of order $O(\nabla)$ vanish in the expression of the active stress above. This is because the centre of mass of each force dipole $\mathbf{r}_i$ is equidistant from the two point forces (see Fig. 3.4(A)). However this is no longer the case if we consider a highly asymmetric swimmer such as in Fig. 3.4(B). Here, the centre of mass $\mathbf{r}_i$ is no longer equidistant from the two point forces - it has a distance b from the front and a distance a from the back. In this case, we expect terms proportional to $\sim (b-a)\nabla$ in the expression of the active stress above.

3.2 Hydrodynamic instabilities and NESS in quasi-1D active fluid

In the introduction we briefly mentioned how active fluids at rest in 1D can become hydrodynamically unstable and lead to a non-equilibrium steady state

(NESS). In that system, the fluid is confined to a 1D box and the polarisation field $\mathbf{p}$ as well as the velocity field $\mathbf{u}$ are also assumed to point in one direction (x-axis if referring to Fig. 1.6). We refer to that case as strict-1D.

Recently hydrodynamic instabilities in quasi-1D active fluids have also been studied analytically in Voituriez *et al.* [36] and numerically in Yeomans *et al.* [60]. In quasi-1D systems, while the hydrodynamic fields still depend on one coordinate, the vector fields (such as $\mathbf{p}$ and $\mathbf{u}$) can now point in any directions in 3D. In this section, we are going to review the linear stability analysis in Voituriez *et al.* [36] and use it to explain the origin of the critical exponent $= 0.5$ which is found almost universally in this thesis.

3.2.1 Initial instabilities

Let us consider a homogenous concentration of extensile particles in quasi-1D. By this we mean that the polarisation and the velocity can have any direction in 3D but the dynamics only depend on one-coordinate (say the z-axis). For simplicity, we assume the concentration of the particles to be constant and thus we ignore the dynamics of $c(z,t)$. Suppose the active particles are confined in between two parallel walls at $z = 0$ and at $z = L$ (see Fig. 3.5). Let us assume non-slip boundary conditions for the fluid velocity $\mathbf{u}(z,t)$ at the walls: $\mathbf{u}(z = 0, t) = \mathbf{u}(z = L, t) = 0$. For the polarisation field $\mathbf{p}(z,t)$, we assume free boundary conditions at the walls so that: $\frac{\partial \mathbf{p}}{\partial z}\big|_{z=0} = \frac{\partial \mathbf{p}}{\partial z}\big|_{z=L} = 0$. Of course this is only a toy model where in actual experiments [51, 52], the swimmers are usually anchored parallel to the walls. Later in the simulations below, we shall change the anchoring to parallel.

The equations we need to solve are summarised below:

$$\frac{\partial \mathbf{p}}{\partial t} + (\mathbf{u} + w\mathbf{p}) \cdot \nabla \mathbf{p} = -\underline{\underline{\Omega}} \cdot \mathbf{p} + \xi \underline{\underline{v}} \cdot \mathbf{p} + \frac{\mathbf{h}}{\Gamma} \tag{3.17}$$

$$-\nabla P + \eta \nabla^2 \mathbf{u} + \nabla \cdot (\underline{\underline{\sigma}}^p + \underline{\underline{\sigma}}^a) = 0 \tag{3.18}$$

$$\nabla \cdot \mathbf{u} = 0 \tag{3.19}$$

where we neglect the inertial term in the Navier-Stokes equation (since the Reynolds number for bacteria is typically around $Re \sim 10^{-5}$ and thus we may neglect the bacteria's inertias (Stokes' limit)). $\mathbf{h} = -\frac{\delta F}{\delta \mathbf{p}}$ is the molecular field. One obvious solution to the equations above (3.17-3.19) is when the particles

are not moving and aligned parallel to each other in the y-direction (rest state solution): $\mathbf{p}_0 = (0, 1, 0)$ and $\mathbf{u}_0 = (0, 0, 0)$ (see Fig. 3.5(A) left).

To see if this 'rest state' solution is stable, we add some arbitrary perturbations $\delta\mathbf{p}(z,t)$ and $\delta\mathbf{u}(z,t)$ to the rest state solution above. If these initially small perturbations decay to zero, the 'rest state' solution is then shown to be stable and the system remains at rest with uniform polarisation and zero velocity. However if these initially small perturbations grow exponentially, the 'rest state' solution is then shown to be hydrodynamically unstable and may evolve to a steady state where the fluid velocity is no longer zero - and thus we have a spontaneous flow transition. Following the derivation of Voituriez *et al.* [36], an active fluid in quasi-1D is shown to be hydrodynamically unstable and exhibit spontaneous flow transition at large enough activity. Here we outline the derivation of Voituriez *et al.* for extensile active fluid.

We substitute the perturbed solution:

$$\begin{aligned}
\mathbf{p}(z,t) &= \mathbf{p}_0 + \delta\mathbf{p}(z,t) = \begin{pmatrix} \delta p_x(z,t) \\ 1 \\ \delta p_z(z,t) \end{pmatrix} \\
\mathbf{u}(z,t) &= \mathbf{u}_0 + \delta\mathbf{u}(z,t) = \begin{pmatrix} \delta u_x(z,t) \\ \delta u_y(z,t) \\ 0 \end{pmatrix}
\end{aligned}$$

to the hydrodynamic equations above (3.17-3.19). Note that $p_y = 1$ since $|\mathbf{p}| \simeq 1$ and $u_z = 0$ from the incompressibility condition (3.19). Neglecting terms of order $\sim O(\delta^2)$, we obtain the linearised equations:

$$\begin{aligned}
\frac{\partial}{\partial t}\begin{pmatrix} \delta p_x \\ 0 \\ \delta p_z \end{pmatrix} &= -\frac{1}{2}\begin{pmatrix} 0 \\ 0 \\ \partial_z \delta u_y \end{pmatrix} + \frac{\xi}{2}\begin{pmatrix} 0 \\ 0 \\ \partial_z \delta u_y \end{pmatrix} + \frac{\kappa}{\Gamma}\begin{pmatrix} \partial_z^2 \delta p_x \\ 0 \\ \partial_z^2 \delta p_z \end{pmatrix} \\
0 &= -\begin{pmatrix} 0 \\ 0 \\ \partial_z P \end{pmatrix} + \eta\begin{pmatrix} \partial_z^2 \delta u_x \\ \partial_z^2 \delta u_y \\ 0 \end{pmatrix} - \frac{\kappa(\xi - 1)}{2}\begin{pmatrix} 0 \\ \partial_z^3 \delta p_z \\ 0 \end{pmatrix} - \zeta c \begin{pmatrix} 0 \\ \partial_z \delta p_z \\ 0 \end{pmatrix}
\end{aligned}$$

From these equations, it is rather straightforward to show that δp_x and δu_x always decay to zero and thus we are only left with $\delta p_z(z,t)$ and $\delta u_y(z,t)$. We can then

expand δp_z and δu_y in Fourier modes as follow:

$$\begin{aligned}\delta p_z(z,t) &= \sum_{n=1}^{\infty} \tilde{P}_n(t) \cos\left(\frac{n\pi z}{L}\right) \\ \delta u_y(z,t) &= \sum_{n=1}^{\infty} \tilde{U}_n(t) \sin\left(\frac{n\pi z}{L}\right)\end{aligned}$$

where we have used Cosines expansion for δp_z and Sines expansion for δu_y to satisfy the boundary conditions $\frac{\partial \delta p_z}{\partial z}\big|_{z=0,L} = 0$ and $\delta u_y|_{z=0,L} = 0$ at the walls. The mode $n = 1$ is shown in Fig. 3.5(A) right, from which, we can see that elastic deformations in the polarisation field is accompanied by a non-zero fluid velocity - thus a spontaneous flow. Substituting these Fourier expansion into the linearised equations, the amplitudes of the perturbations $\widetilde{P}_n(t)$ and $\widetilde{U}_n(t)$ can be shown to have the following forms:

$$\begin{aligned}\widetilde{P}_n(t) &= \widetilde{P}_n(0) e^{\omega_n t} \\ \widetilde{U}_n(t) &= \widetilde{U}_n(0) e^{\omega_n t}\end{aligned}$$

where

$$\omega_n = \frac{\zeta c(\xi - 1)}{2\eta} - \frac{\kappa n^2 \pi^2 \{(\xi-1)^2 + \frac{4\eta}{\Gamma}\}}{4\eta L^2}$$

The rest state is then shown to be unstable if the perturbation grows exponentially or $\omega_n > 0$ for some n's. Furthermore we can also see that for a fixed value of ζ, mode $n = 1$ is the most unstable mode since ω_1 has the largest positive value. Correspondingly, the critical value of activity ζ_c (above which the rest state becomes unstable) can be found by setting $\omega_1 = 0$; from which we obtain [36]:

$$\zeta_c = \frac{\kappa \pi^2 \{(\xi-1)^2 + \frac{4\eta}{\Gamma}\}}{2cL^2(\xi - 1)}$$

One more thing to note is that the critical activity also scales with the system size L as: $\zeta_c \sim 1/L^2$. This means that increasing the system size may equally make the rest state solution becomes unstable. The origin of scaling with the inverse system size squared can be roughly explained in the following way. First we recall that the hydrodynamic interaction between the bacteria is long range. Secondly in our systems, this hydrodynamic interaction is only limited by the distance

between the walls since the hydrodynamic velocity has to vanish at the walls (non-slip boundary condition). Thus increasing the distance between the walls (or the system size) will then increase the effective range of the hydrodynamic interaction between the bacteria, making it more likely to induce macroscopic instabilities.

3.2.2 Final steady states

Voituriez *et al.* showed that the rest state solution is hydrodynamically unstable beyond some critical activity ζ_c (the value of ζ_c itself depends on the system size L and various other parameters such as the elastic constant k). Furthermore it can also be shown that mode $n = 1$ corresponding to the Poiseuille-like flow (see Fig. 3.5(A) right) is the most unstable mode. Subsequently this mode will dominate over short times but what does the final steady state look like? To answer this question, we have to go beyond linear order approximation in the δ-expansion. First we make expansion around the critical point as follows: $\zeta = \zeta_c + \delta\zeta$. We then look at mode $n = 1$ solution close to this critical point by considering higher order terms if necessary. It can then be shown that the amplitude of mode $n = 1$ satisfies a Landau equation [61]:

$$\frac{d\widetilde{U}_1(t)}{dt} = -a\delta\zeta\widetilde{U}_1 + b\left|\widetilde{U}_1\right|^2\widetilde{U}_1 \tag{3.20}$$

for some positive constants a and b. (The Landau equation above came from the Navier-Stokes equation by making a polynomial expansion around the critical point.) The solution of this Landau equation is again rather straightforward. For $\delta\zeta < 0$, $\widetilde{U}_1(t)$ will decay exponentially and thus mode $n = 1$ (as well as all the other modes $n = 2, 3, ...$) vanishes and the rest state is recovered. For small $\delta\zeta > 0$, however, $\widetilde{U}_1(t)$ will increase exponentially before saturating to a steady state value $\widetilde{U}_1(t \to \infty)$ which is non-zero. All the other modes are unimportant here because they are overshadowed by mode $n = 1$. The final steady state will therefore look like mode $n = 1$ shown in Fig. 3.5(A) right.

To find the steady state amplitude $\widetilde{U}_1(t \to \infty)$ at activity larger than the critical activity ($\delta\zeta > 0$), we set $\frac{d}{dt} \to 0$ in Eqn. (3.20) from which we recover the

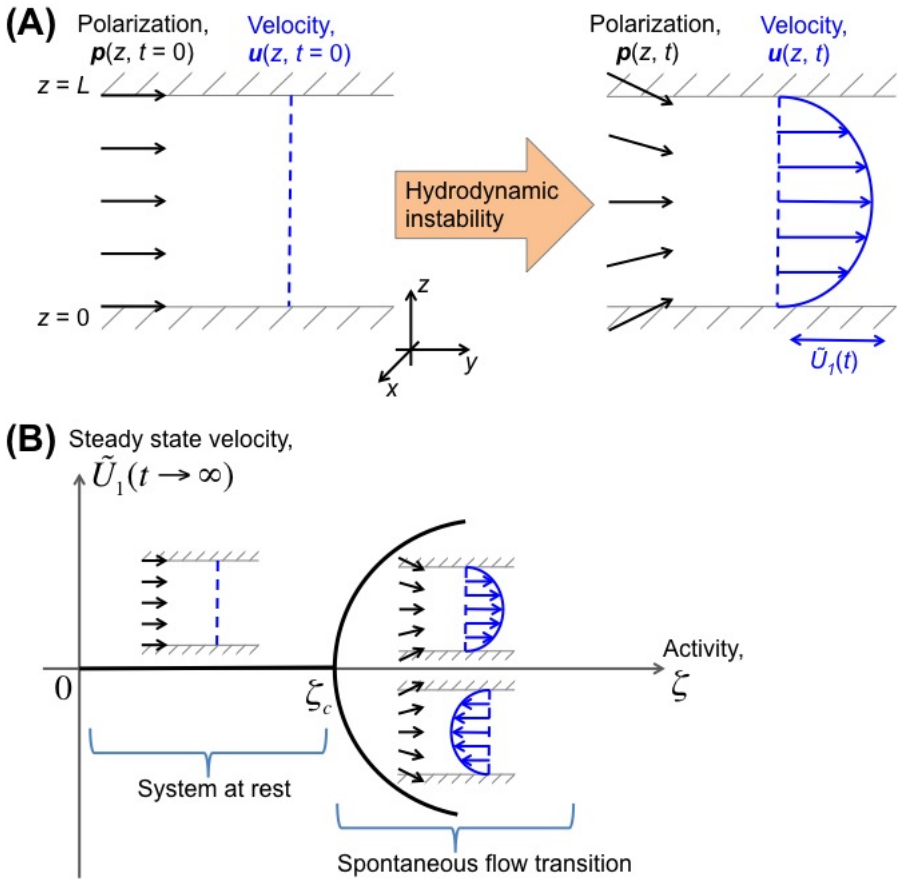

Figure 3.5: Illustration of hydrodynamic instabilities in quasi-1D active fluid. **(A)** An active fluid at rest (left) is shown to be unstable with respect to splay instability (right) at large enough activity. This instability is also accompanied by a macroscopic fluid flow which is similar to a Poiseuille flow (blue colour). **(B)** Plot of the steady state fluid velocity ($t \to \infty$) as a function of the activity ζ. Below the critical value ζ_c the fluid remains at rest whereas above ζ_c, the initial instability evolves to a steady state fluid flow which also looks like a Poiseuille flow.

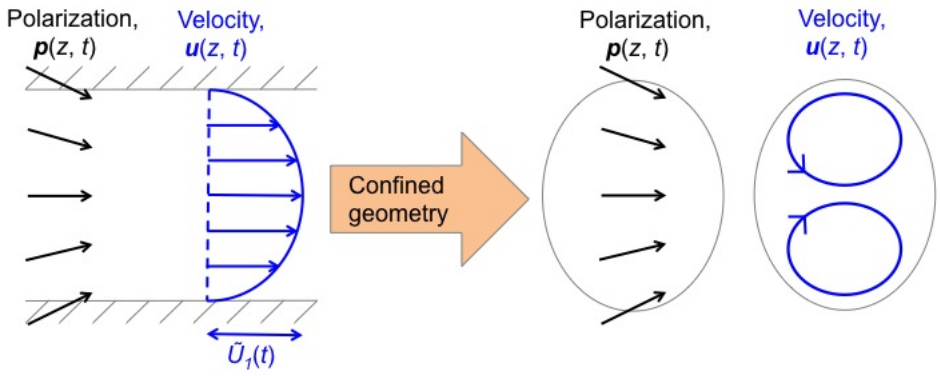

Figure 3.6: The effect of a spontaneous flow transition in a confined geometry. Here if we imagine the active fluid to be confined to an ellipsoid geometry, the fluid flow at steady state becomes a pair of vortices. Remarkably the mean field exponent of 0.5 is still preserved (as we will show in chapter 5).

mean field exponent = 0.5:

$$\widetilde{U}_1(t \to \infty) \sim \pm\sqrt{\delta\zeta}$$

This steady state amplitude is plotted against the activity in Fig. 3.5(B). Also notice that the value of $\widetilde{U}_1(t \to \infty)$ can either be positive or negative signifying a spontaneous symmetry breaking with $\widetilde{U}_1 > 0$ corresponds to a spontaneous flow to the right and $\widetilde{U}_1 < 0$ corresponds to a spontaneous flow to the left (see Fig. 3.5(B)).

Finally we shall briefly mention what happens to active fluids in a confined geometry. For instance, we can imagine a droplet of active fluid as shown in Fig. 3.6. Here, the Poiseuille-like steady state flow found in quasi-1D will transform into a pair of fluid vortices. The reasons why this is the case are quite simple. The fluid cannot escape the elliptical confinement and there can be no fluid sources/sinks (due to incompressibility condition $\nabla \cdot \mathbf{u} = 0$). Therefore the only possible solution is that of rotational flows. Remarkably even in a confined geometry, the mean field exponent = 0.5 is still preserved as we shall see in chapter 5.

3.3 Hydrodynamic instabilities and NESS in quasi-2D active fluid

The stability analysis above predicts a mean field scaling of the critical activity with the inverse system size squared: $\zeta_c \sim 1/L^2$. Furthermore, it also predicts a mean field exponent of half for the most unstable mode: $\widetilde{U}_1 \sim \sqrt{\zeta - \zeta_c}$. In this section, we will show that these scaling laws are indeed observed in strict- and quasi-2D simulations. On the other hand, quasi-1D simulations have been done extensively in [60], in which, they showed that there can only be one steady state in a quasi-1D extensile active fluid. This steady state looks like a Poiseuille flow or hydrodynamic mode $n = 1$ dicussed in the previous section (see Fig. 3.5(B)). However in quasi-2D or strict-2D, we show below that there could be more than one steady state with phase transitions leading from one steady state to another. But first, we establish a quasi-2D geometry as follows.

The macroscopic variables (such as the polarization and the fluid velocity) are defined on the y-z plane and we assume translational symmetry in the x-direction. We also define a non-slip wall at $z = 0$ and at $z = L$ and a periodic boundary condition at $y = 0$ and $y = L$ (see Fig. 3.7). Later we will also consider the effect of shear by introducing wall velocities in the direction indicated in the figure. Topologically, this geometry is similar to the double cylinder (Couette) geometry used in many rheological measurements.

At the walls, we assume strong parallel anchoring condition for the polarization field: $\mathbf{p}(z = 0) = \mathbf{p}(z = L) = \hat{y}$. We also assume a non-slip condition for the fluid velocity: $\mathbf{u}(z = 0) = \mathbf{u}(z = L) = 0$. The appropriate boundary condition for the concentration field c is the no-flux condition:

$$\begin{aligned} \mathbf{j} \cdot \hat{z} &= 0 \quad (\text{at } z = 0, L) \\ \implies \left.\frac{\partial c}{\partial z}\right|_{z=0,L} &= 0 \end{aligned}$$

Note that even though the polarization vector $\mathbf{p}$ and the fluid velocity $\mathbf{u}$ only depend on two coordinates y and z, they can still point in any direction in 3D,

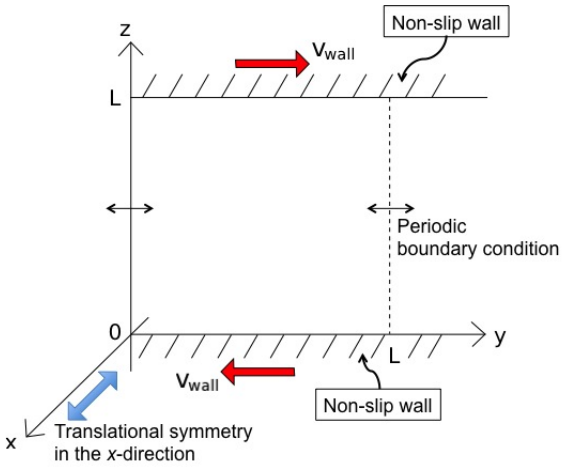

Figure 3.7: Quasi-two dimensional geometry. Extensile active fluid is confined in between two parallel non-slip walls at $z = 0$ and $z = L$ while periodic boundary condition is assumed at $y = 0$ and $y = L$. Furthermore the system is assumed to be invariant under translation in the x-direction (no x-dependence on the dynamics).

i.e.

$$\mathbf{p} = \begin{pmatrix} p_x(y,z,t) \\ p_y(y,z,t) \\ p_z(y,z,t) \end{pmatrix} \quad \text{and} \quad \mathbf{u} = \begin{pmatrix} u_x(y,z,t) \\ u_y(y,z,t) \\ u_z(y,z,t) \end{pmatrix}$$

We refer to this case as 'quasi-2D' as opposed to 'strict-2D' where the directions of $\mathbf{p}$ and $\mathbf{u}$ are also confined on the same 2D plane.

3.3.1 Mapping simulation units to physical units

To solve the hydrodynamic equations, we used a hybrid lattice Boltzmann scheme as described in chapter 2. The parameters used in our simulations are chosen to correspond roughly to those of bacterial suspensions. The lattice Boltzmann method typically defines a lengthscale (λ), timescale (τ) and mass scale (μ) which are in turn constrained by the Reynolds number of the problem (around $Re \sim 10^{-5}$). In simulation units, these scales are defined to be equal to one: $\lambda = \tau = \mu = 1$. To explore the mapping into physical units, we now suppose these scales to be: $\lambda = 4\,\mu$m, $\tau = 10\,$ms, and $\mu = 0.1\,\mu$g in physical units - which are also roughly the typical size/velocity/mass of a swimming bacterium.

For example, the swimming speed of the bacteria is typically around $w \simeq$

	Simulation units	Physical units
Fluid viscosity, η	2.5	$6.3 \times 10^{-3}\,\mathrm{kg\,m^{-1}s^{-1}}$
Average concentration of swimmers, c_0	1	$0.016\,\mu\mathrm{m}^{-3}$
Diffusion constant, $D = MB$	0.1	$1.6 \times 10^{-6}\,\mathrm{cm^2s^{-1}}$
Effective elastic constant, k	0.04	$0.16\,\mathrm{pN}$
Shape factor, ξ	1.1	dimensionless
Active stress due to dipolar force, ζc_0	$0 - 0.03$	$0 - 0.0075\,\mathrm{Pa}$
Swimming speed, w	$0 - 0.02$	$0 - 8\,\mu\mathrm{m\,s}^{-1}$

Table 3.1: Typical values of the parameters used in the simulations.

$2\,\mu\mathrm{m}/s$. To convert this to the simulation units, we first write w in terms of λ, τ, and μ:

$$\begin{aligned} w &= 2\,\mu\mathrm{m}/s \\ &= 0.005\frac{4\,\mu\mathrm{m}}{10\,\mathrm{ms}} \\ &= 0.005\frac{\lambda}{\tau} \end{aligned}$$

and thus in simulation units, $w \simeq 0.005$ (since $\lambda = \mu = \tau = 1$). Other parameters are also set within reasonable order of magnitude (similar to other models of bacterial suspensions [24]) and they are summarised in Table 3.1.

3.3.2 NESS in a suspension of polar shakers

We begin by studying the behaviour of a suspension of extensile shakers (*i.e.* $w = 0$ but $\zeta > 0$). In particular we are interested in the steady state solution ($\frac{\partial}{\partial t} \to 0$) to Eqns. (3.6-3.12). One obvious solution is the no-flow or 'rest' state solution:

$$\begin{aligned} c(y,z,t) &= c_0 \\ \mathbf{p}(y,z,t) &= \hat{y} \\ \mathbf{u}(y,z,t) &= 0 \end{aligned}$$

which is the only stable solution at low activity. However at large enough activity (above some critical activity ζ_{c1}), the rest state becomes linearly unstable and the system undergoes a spontaneous flow transition to a steady flow state,

characterised by the appearance of fluid vortices similar to Rayleigh-Benard convection flow in the introduction.

The spontaneously flowing steady state is an intrinsically non-equilibrium hydrodynamic state since the system is continuously dissipating energy *via* the fluid viscosity. In fact we can make use of this fact to obtain an order-of-magnitude estimate of the typical fluid velocity in the spontaneously flowing state. To do this, we balance the viscous force with the active force coming from ζ:

$$\begin{aligned} \eta\nabla^2\mathbf{u} &\sim \nabla\cdot\underline{\underline{\sigma}}^a \\ \implies u^* &\sim \frac{(\zeta-\zeta_{c1})cL}{\eta} \end{aligned} \tag{3.21}$$

where we use the approximation $\nabla \sim \frac{1}{L}$, with L being the system size. Other than some simple scaling analysis, analytic solutions including linear analysis becomes intractable in 2D and thus we have to rely on numerical simulations. The numerical method that we use is explained in chapter 2.

At large enough activity $\zeta > \zeta_{c1}$, the rest state becomes hydrodynamically unstable. This means that any small perturbations introduced to the system will grow exponentially. Physically, such a small perturbation may come from thermal or active fluctuations. Numerically, we add this pertubation manually by adding some random numbers to the macroscopic fields such as $\mathbf{p}$ or $\mathbf{u}$. Although the initial perturbation is random, at a later stage, the system will pick up the most unstable mode from the perturbed system. The characteristic wavelength of this most unstable mode typically depends on the system size L and more importantly on the activity parameter ζ. This unstable mode continues to grow until the system stabilises to a steady flowing state. The system is then said to have undergone a spontaneous flow transition from the rest state to this steady flowing state. To characterise this spontaneous flow transition, we define the 'amplitude' of the unstable mode as:

$$A(t) = \left\{\frac{1}{V}\int d^3r\,(\nabla\mathbf{p})^2\right\}^{1/2} \tag{3.22}$$

where V is the volume of the simulation box. Note that A has the dimension of inverse length characterising the amount of deformation in the polarisation

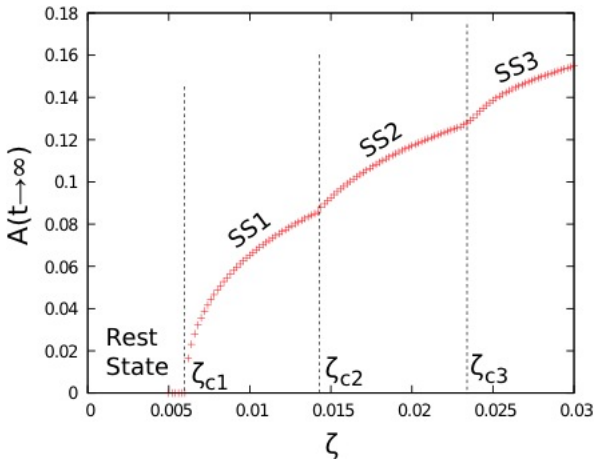

Figure 3.8: The bifurcation diagram: plot of steady state amplitude $A(t \to \infty)$ as a function of activity ζ in simulation units. The plot shows three distinct steady states (labelled SS1, SS2, and SS3) well separated by three critical points (ζ_{c1}, ζ_{c2}, and ζ_{c3}). Below the first critical point ζ_{c1}, the rest state is stable.

vector $\mathbf{p}$ which is also related to the typical magnitude of the fluid velocity since $\mathbf{u}$ is also strongly coupled to $\mathbf{p}$. Thus by definition, A is equal to zero when the system is at rest and non-zero when the system spontaneously flows.

Fig. 3.8 shows the plot of the steady state amplitude $A(t \to \infty)$ as a function of the activity ζ. For low activity $\zeta < \zeta_{c1}$, the rest state is stable and thus any finite perturbation introduced at $t = 0$ will quickly decay to zero and the system reestablishes the rest state. Therefore $A(t \to \infty)$ is zero for $\zeta < \zeta_{c1}$. However past this threshold, the rest state becomes linearly unstable with respect to any small perturbations. Consequently, the amplitude $A(t)$ will increase exponentially in the beginning but then converge to some finite value $A(t \to \infty)$ as the system reaches a steady state. Furthermore from Fig. 3.8, the transition from this rest state to the first steady state (SS1) is a continuous one - similar to a second order phase transition - with again a mean field exponent of 0.5:

$$A(t \to \infty, \zeta) \sim (\zeta - \zeta_{c1})^{0.5} \quad \text{, for } \zeta \text{ close to } \zeta_{c1} \tag{3.23}$$

In nonlinear dynamics, this is also known as a supercritical Hopf bifurcation [61]. The plot of steady state 1 (SS1) is shown in Fig. 3.9(A). Again, the steady state fluid velocity consists of vortices on the y-z plane. However unlike the Rayleigh-Benard convection, there is also an out-of-plane component (x-component) of the

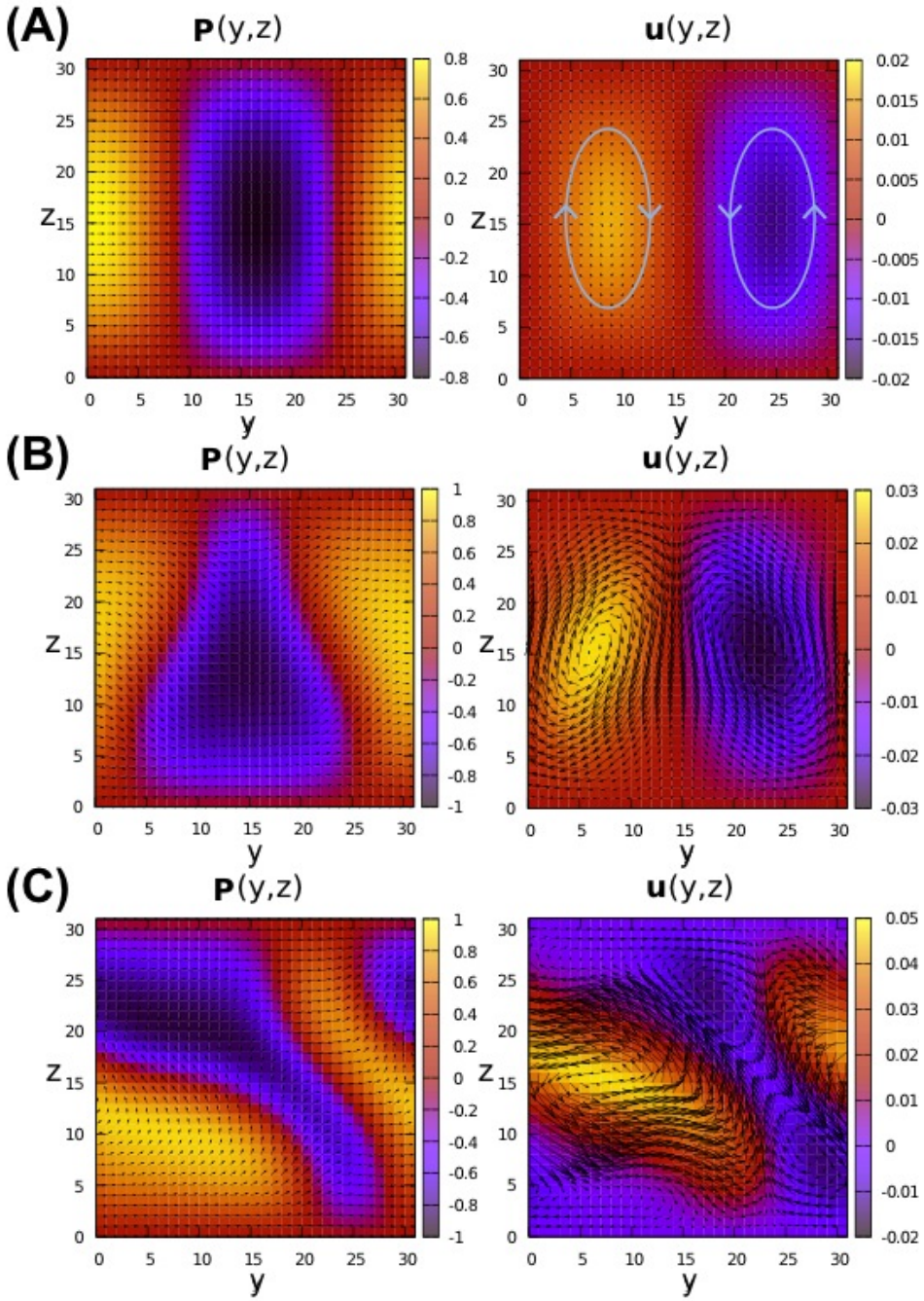

Figure 3.9: **(A)** Plot of the steady state polarization (left) and fluid velocity (right) of steady state 1 (SS1), which has the characteristics of two convection rolls. The contour plot represents the out-of-plane or x-component of the vector fields while the arrows represent the in-plane or y- and z- components of the vector fields. **(B)**, **(C)** Similar plots for steady state 2 (SS2), which has two squashed rolls, and steady state 3 (SS3), which has two even more squashed rolls, respectively.

steady state fluid velocity which is two/three orders of magnitude larger than the in-plane components. So we observe a non-equilibrium phase transition to a steady state in which the fluid is flowing (mostly in the x-direction). As usual, this spontaneously flowing state is also accompanied by large elastic deformation in the polarization field $\mathbf{p}(y, z)$ (Fig. 3.9(A) left). Also notable is that the polarization field is twisted to point in either $+x$-direction or $-x$-direction, *i.e.* out-of-plane.

Using some simple scaling analysis, we can also make an order-of-magnitude estimate of this critical point ζ_{c1}. First we recall that the spontaneous flow transition from the rest state to SS1 is accompanied by some forms of elastic deformation. Therefore spontaneous flow transition must occur if the active stress $\underline{\underline{\sigma}}^a$ is large enough to overcome the elastic stress $\underline{\underline{\sigma}}^p$. Thus at the critical point ζ_{c1}, we approximately have:

$$\underline{\underline{\sigma}}^a \sim \underline{\underline{\sigma}}^p$$

Using Eqns. (3.13) and (3.14), we have: $\sigma^p_{\alpha\beta} = \kappa\partial_\alpha p_\gamma \partial_\beta p_\gamma + ... \sim \frac{\kappa}{L^2}$ and $\sigma^a_{\alpha\beta} = -\zeta c p_\alpha p_\beta \sim \zeta c_0$ (where we have used the approximation $\nabla \sim \frac{1}{L}$). We then obtain the following scaling relation at the critical point:

$$\zeta_{c1} \sim \frac{\kappa}{c_0 L^2} \tag{3.24}$$

Like quasi-1D active fluids, the critical activity also scales with the system size as $\zeta_{c1} \sim \frac{1}{L^2}$. This is again confirmed in numerical data in Fig. 3.10.

Further increase in the activity leads to more transitions which are still continuous (see Fig. 3.8). First we observe a transition from steady state 1 (SS1) to steady state 2 (SS2) at $\zeta = \zeta_{c2}$ and then another transition from steady state 2 (SS2) to steady state 3 (SS3) at $\zeta = \zeta_{c3}$ (see Fig. 3.9 for the plots of SS1-SS3). These transitions are detected by a kink in the bifurcation plot (plot of $A(t \to \infty)$ against ζ). Just like second order phase transition in equilibrium physics, these transitions are also accompanied by a spontaneous symmetry breaking (first along the y-axis as one crosses ζ_{c2} and then along the z-axis as one crosses ζ_{c3}).

The plots of the steady states (SS1-SS3) are given in Fig. 3.9. From this figure, steady state 1 (SS1) has two symmetric convection rolls similar to the Rayleigh-Benard example in the introduction. Steady state 2 (SS2) also has two rolls but squashed along the y-axis, breaking the symmetry along this axis. Finally steady

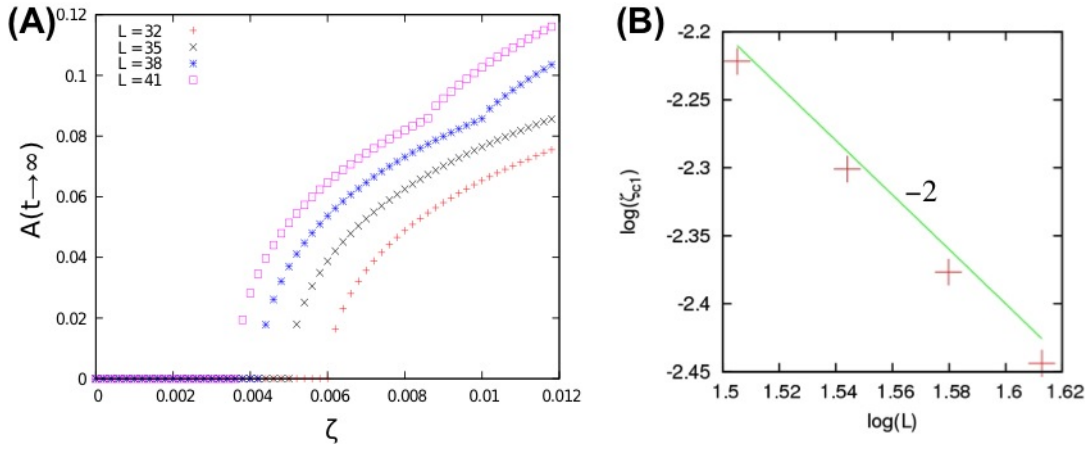

Figure 3.10: **(A)** The bifurcation plot is shifted to the left as the system size L is increased. **(B)** Log-log plot of the critical activity ζ_{c1} (where the system first becomes unstable) as a function of the system size L showing the expected scaling relation: $\zeta_{c1} \sim \frac{1}{L^2}$ (see main text).

state 3 (SS3) has two even more squashed rolls, breaking the symmetry along the y- and z-axes.

3.3.3 NESS in a suspension of polar shakers under imposed shear

We now turn to the effect of an imposed shear flow on the physics of quasi-2D extensile polar shakers. Fig. 3.11(A) shows the bifurcation diagram in the presence of an imposed shear. Like before, we can still characterise the stability of different steady states (including the rest state) by looking at the steady state amplitude $A(t \to \infty)$ as a function of activity ζ. In general the presence of a small imposed shear ($v_{wall} \lesssim 0.0032 = 1.2\,\mu$m/s, red curve in Fig. 3.11(A)) does not change the bifurcation or the positions of the critical points very much. The only noticeable difference is perhaps the steady state patterns now look like a distorted version of those without shear (compare Fig. 3.11(B) to Fig. 3.9(B)).

At larger shear flow ($v_{wall} \gtrsim 0.0032$, blue curve in Fig. 3.11(A)), however, SS2 and SS3 disappear altogether and SS1 is the only stable steady state left after the rest state. We can then construct the phase diagram (shown in Fig. 3.11(C)) showing the stability regions of steady states SS1-SS3 in the parameter space v_{wall}-ζ. In particular from the phase diagram, we see that the transition line separating

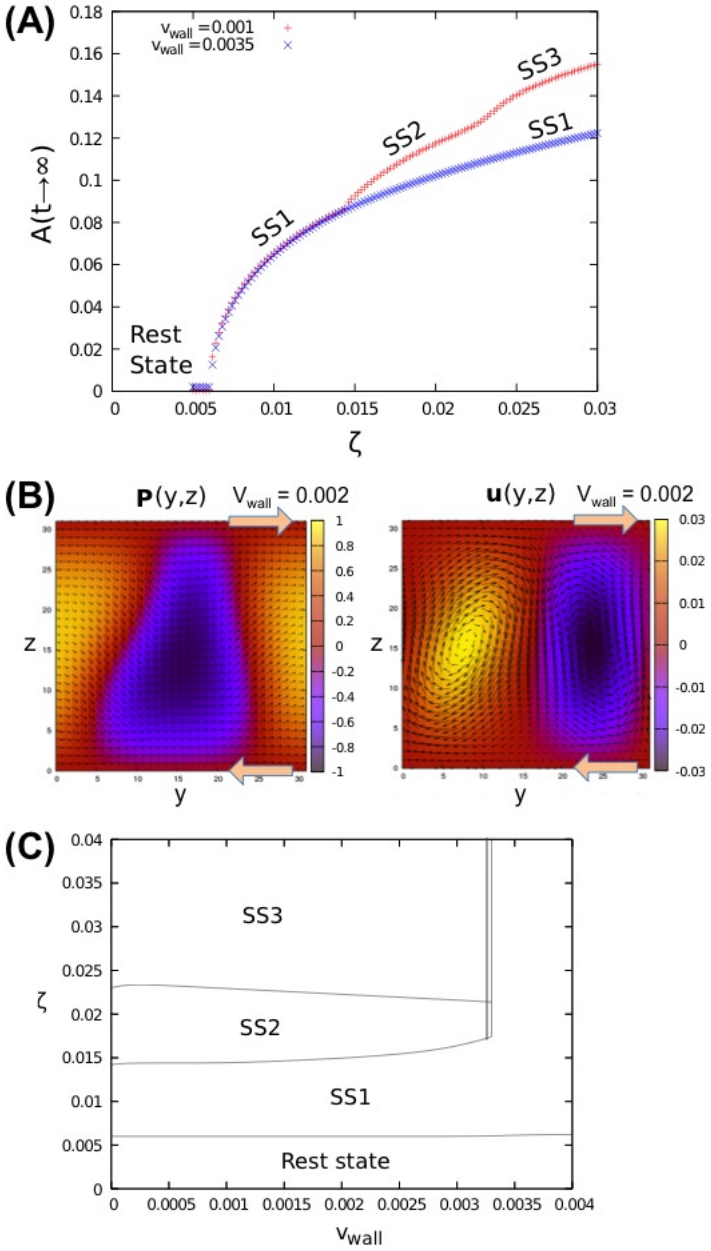

Figure 3.11: **(A)** Plot of the steady state amplitude $A(t \to \infty)$ against the activity ζ in the presence of an imposed shear. The top curve shows the bifurcation with wall velocity $v_{wall} = 0.001$ and the bottom curve shows the bifurcation with wall velocity $v_{wall} = 0.0035$. **(B)** Shows steady state 2 (SS2) in the presence of an imposed shear ($v_{wall} = 0.002$) which looks like a distorted version of SS2 without shear (*cf.* Fig. 3.9(B)). **(C)** The phase diagram in the parameter space v_{wall}-ζ showing the stability regions of steady states SS1-SS3. Single lines represent continuous (second-order) transitions while double lines represent discontinuous (first-order) transitions. The phase boundaries were determined on a grid with $\Delta v_{wall} = 10^{-4}$ and $\Delta\zeta = 2 \times 10^{-4}$.

rest state from SS1 does not change very much with increasing v_{wall}. This means that the presence of an imposed external shear does not change the stability of the rest state very much. In addition, we also observe a first order transition line at $v_{wall} \simeq 0.0033$ (represented by a double line in the phase diagram). As one crosses this transition line, the steady state amplitude $A(t \to \infty)$ becomes discontinuous, and as such, the transition does not involve a simple spontaneous symmetry breaking anymore.

3.4 Hydrodynamic instabilities and NESS in strict-2D active fluid

While the quasi-2D geometry might be relevant in a rheological measurement of active fluids such as one in [62], other experiments on bacterial suspensions are performed in a strict-2D/thin-film geometry. Physically, the bacteria are trapped in a liquid/air interface so that large out-of-plane velocity component/polarisation is now forbidden. Mathematically in such geometry, the vector fields still depend on two coordinates: y and z, but in addition, their directions are also confined to the y-z plane, *i.e.*

$$\mathbf{p} = \begin{pmatrix} 0 \\ p_y(y,z,t) \\ p_z(y,z,t) \end{pmatrix} \quad \text{and} \quad \mathbf{u} = \begin{pmatrix} 0 \\ u_y(y,z,t) \\ u_z(y,z,t) \end{pmatrix}$$

Below we are going to consider first the case of extensile particles without swimming (shakers) and then the case of extensile swimmers (movers).

3.4.1 NESS in a suspension of polar shakers

The stability/bifurcation diagram for the strict-2D extensile shakers is shown in Fig. 3.12(A). Similarly as before, we find that the rest state becomes unstable above some critical activity ζ_c and this hydrodynamic instability eventually develops into a non-equilibrium steady state (labelled SS-a in the figure). The steady state polarisation $\mathbf{p}$ and velocity $\mathbf{u}$ for SS-a is shown in Fig. 3.12(B). Again, we observe in-plane fluid vortices in the steady state but note that there is no out-of-plane flow in strict-2D.

At even larger activity (above a second critical activity ζ^*, see Fig. 3.12(A)), SS-a now becomes unstable and is replaced by SS-b. As can be seen from Fig. 3.12(B,C), SS-a consists of two convection rolls whereas SS-b consists of four convection rolls. Furthermore, the steady state amplitude $A(t \to \infty)$ also becomes discontinuous at ζ^*; signifying a first order phase transition from SS-a to SS-b. If we compare steady state velocity in SS-a (Fig. 3.12(B) right) to that of SS-b (Fig. 3.12(C) right), it is quite clear that the transition from SS-a to SS-b involves a spatial period-doubling (from two rolls to four rolls) rather than a spontaneous symmetry breaking. Thus this transition is distinguished from the second order transition obtained above where $A(t \to \infty)$ remains continuous.

3.4.2 NESS in a suspension of polar shakers under imposed shear

We also study the effect of an imposed shear on NESS in strict-2D geometry. Here we still assume that the particles are not swimming (shakers). As we did for the quasi-2D case, we can map the stability of the NESS to the parameter space $\zeta - v_{wall}$ (this is shown in Fig. 3.13(A)). In general, the effect of shear is initially similar to the one observed in the quasi-2D geometry, in that the steady states are slightly distorted in the direction of shear. Also, in this thin film geometry case, the stability of the rest state is not changed much by the presence of an external shear. However, there is one qualitative difference with the quasi-2D results, in that in the thin film geometry we find a new shear-induced steady state. This is labelled SS-c in Fig. 3.13. This new steady state is effectively 1D with variations of the velocity and polarisation profiles along the z-direction only (see Fig. 3.13(C)) and is only observed at high shear rate.

The transition lines in the phase diagram (in Fig. 3.13(A)) are all first order except for those from the rest state to SS-a and from SS-b to SS-d which are continuous. As before the second-order transition lines are characterised by a spontaneous symmetry breaking. For example, the reflection symmetry (about the z-axis) in SS-b is lost when the system evolves into SS-b (compare the polarisation pattern of SS-b in Fig. 3.12(C) to that of SS-d in Fig. 3.14(A)).

Finally, at large values of activity (see the upper region in the phase diagram Fig. 3.13(A)), the system becomes turbulent without reaching a steady state [63, 24]. In this turbulence phase, the polarisation field and the velocity

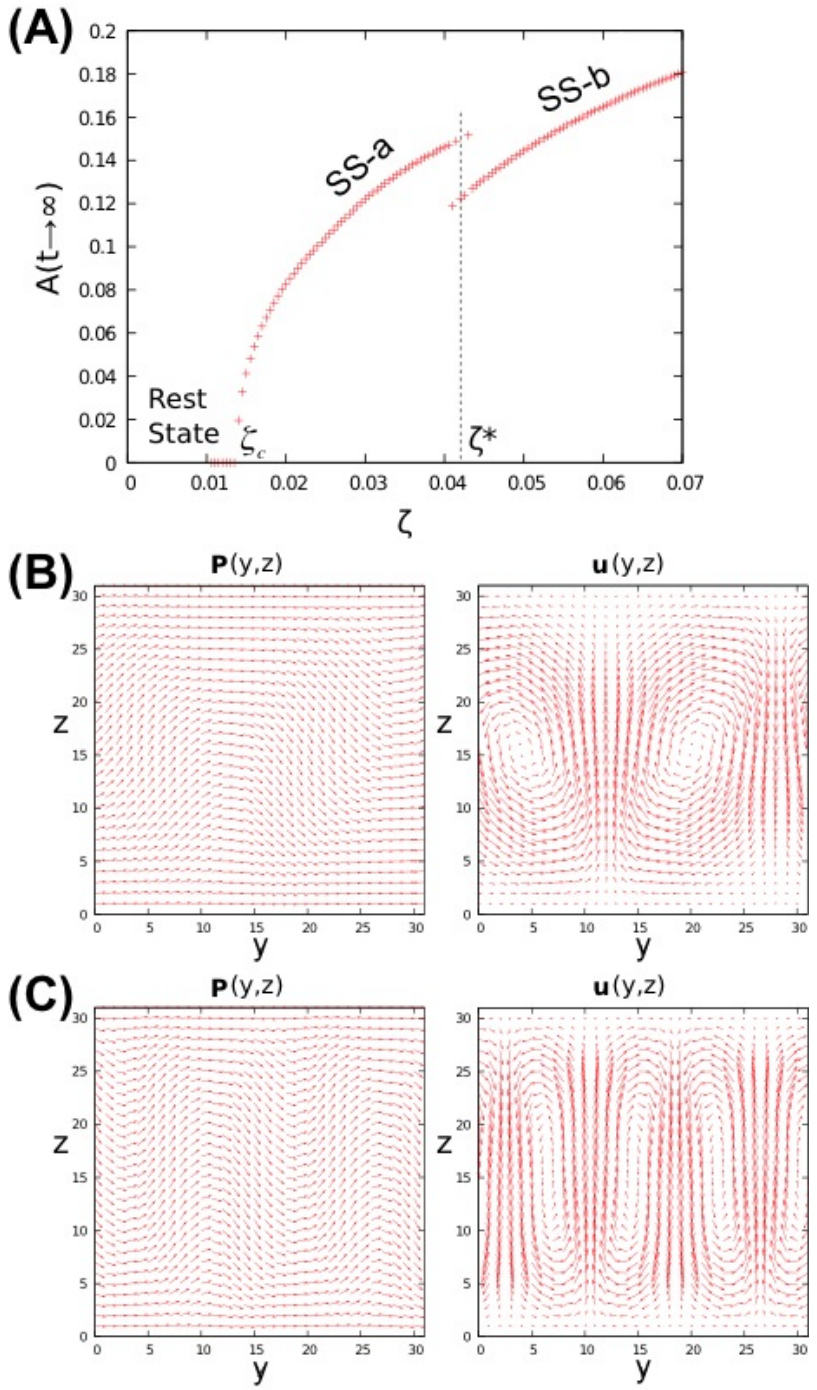

Figure 3.12: **(A)** The bifurcation diagram for thin-film or strict-2D geometry. Notice that the steady state amplitude $A(t \to \infty)$ becomes discontinuous at the second critical activity ζ^*, signifying a first order transition from steady state A (SS-a) with two rolls to steady state B (SS-b) with four rolls. **(B)**, **(C)** Plots of steady state polarisation $\mathbf{p}$ and velocity $\mathbf{u}$ in SS-a and SS-b respectively.

field are changing rapidly and continuously (see Fig. 3.14(B)), similar to what one normally sees in a bacterial suspension under microscope. Another way to obtain this turbulence phase is by increasing the system size L (since we have a scaling law between the critical activity and the system size: $\zeta_c \sim 1/L^2$). This turbulence phase is also observed in quasi-2D systems at large activity (although this is not shown in the phase diagram for the quasi-2D system Fig 3.11(C)).

3.4.3 NESS in a suspension of polar movers

We now turn our case to a suspension of movers where in addition to extensile dipolar force $\zeta > 0$, the particles are also now swimming with some speed $w > 0$. This is a more realistic model of bacterial suspensions such as *P. mirabilis* shown in Fig. 1.2(A). We shall first consider the effect of a finite but small swimming speed. By this we mean that the swimming speed w is much smaller than the typical fluid flow generated by the spontaneous flow transition u^* (see Eqn. (3.21)). In this case, the bifurcation and the positions of the critical points do not change much but the steady states now become travelling wave solutions. For example, let us consider SS-a with an addition of small swimming speed w (see Fig. 4.2(A)). After the initial perturbations, the system finally settles into a travelling wave steady state (approximately at time $t = 53000$). The final steady state pattern still looks very much like SS-a except the pattern is now moving to the right (travelling wave). The direction of travel also coincides with the global average of the polarization $\mathbf{p}$. (Recall that $\mathbf{p}$ is the direction of swimming.) To see signatures of the travelling wave steady state, one can look at the trajectories of the swimmers (green and blue lines in the figure) which look like a helix. Note that the steady state amplitude $A(t \to \infty)$ is still constant for travelling wave solutions since the polarisation pattern is not changed; it is merely advected to the right by the swimming velocity.

Finally for the case of large swimming speed ($w >> u^*$), the travelling wave steady states can drive a large concentration gradient (of up to 50% for $w \simeq 0.02 = 8\,\mu$m/s, see Fig. 4.2(B)). This large density fluctuations are not uncommon and they are often observed in self-propelled particles [6, 7, 8, 9].

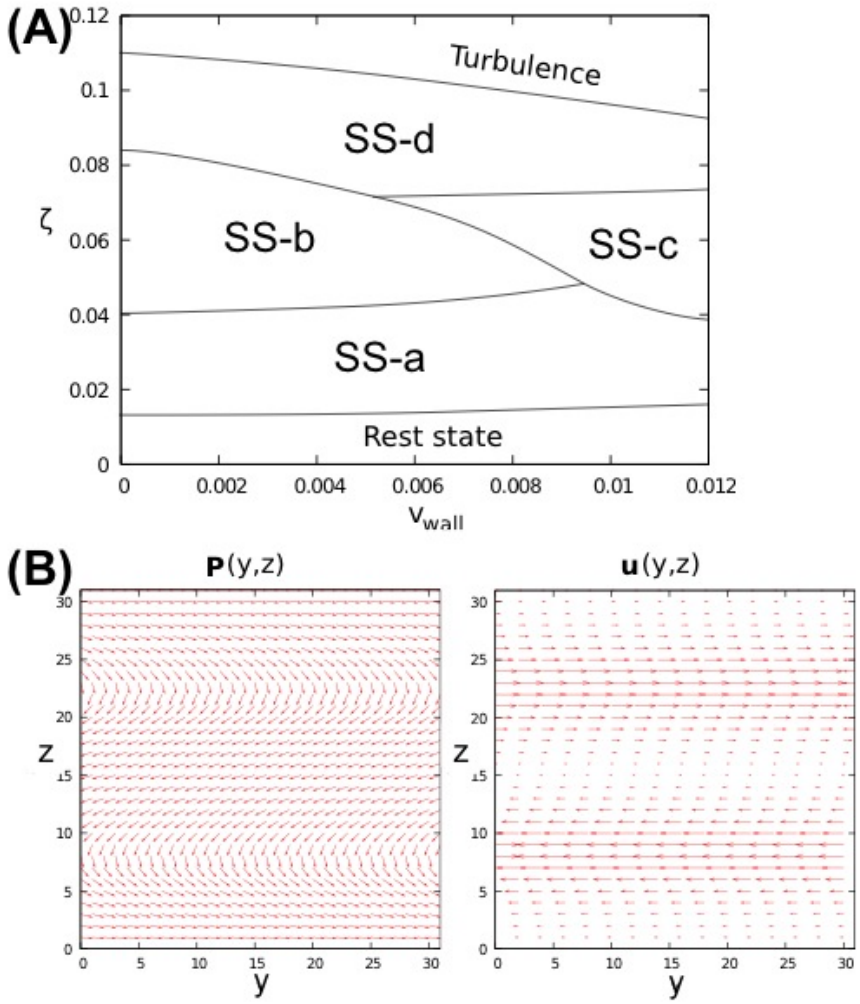

Figure 3.13: **(A)** The phase diagram for thin-film geometry showing distinct steady states labelled SS-a, SS-b, SS-c and SS-d. All transitions are first order except for rest-state to SS-a and SS-b to SS-d. The phases were determined on a grid with $\Delta V_{wall} = 5 \times 10^{-4}$ and $\Delta\zeta = 5 \times 10^{-4}$ and boundaries drawn between the points on this grid. **(B)** Steady state c in thin film geometry which appears under high shear rate. This steady state has the characteristic of two bands of opposite flows. The plots show the steady state polarization vector (left) and fluid velocity vector (right). The maximum magnitude of the fluid velocity is 0.09 (in simulation units).

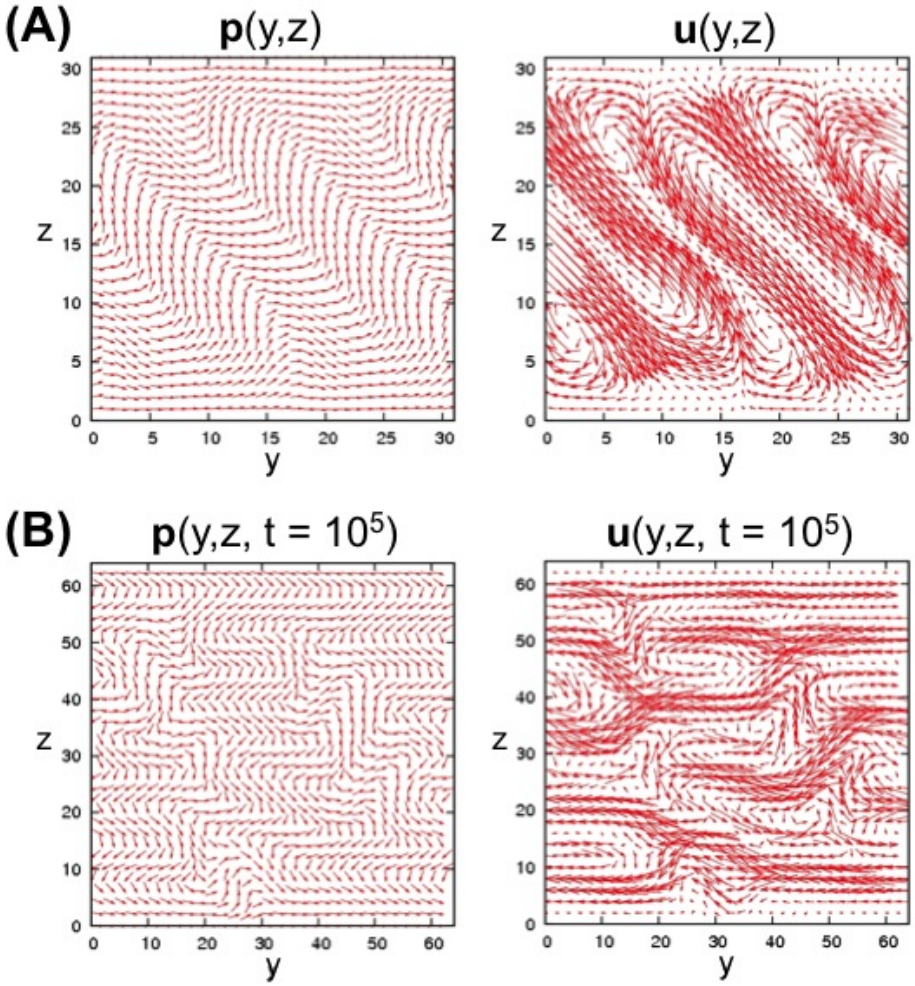

Figure 3.14: **(A)** Steady state polarisation and velocity fields for steady state d (SS-d). **(B)** A snapshot of the turbulent state, observed at high activity/system size. (In this case, we doubled the system size to increase the resolution.) The fluid velocity scale in this figure is 0.1 (in simulation units).

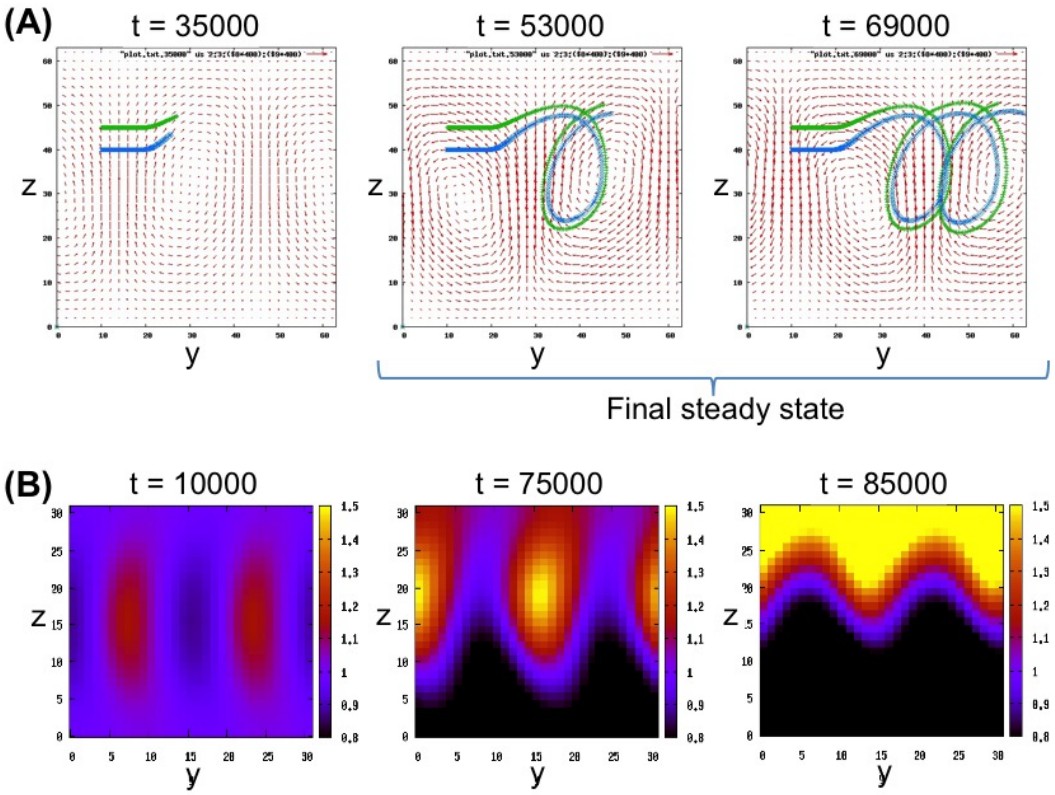

Figure 3.15: **The effect of swimming on NESS in polar active fluids.** **(A)** For the case of small swimming speed, the steady states become travelling wave solutions. Here shows the velocity field of SS-a with an addition of small swimming velocity. The system reaches a 'steady state' solution at $t = 53000$ and the final steady state pattern looks very much like SS-a except that it is now moving to the right (travelling wave). The green and blue lines show the trajectories of two swimmers. **(B)** For the case of large swimming speed, the swimming can induce a large concentration fluctuation (up to 50% for $w \simeq 0.02 = 8\,\mu$m/s). The contour plot represents the concentration of the swimmers. This large density fluctuations are also observed in self-propelled particles [6, 7, 8, 9].

3.5 Summary

In conclusion, we find that extensile active fluids in a quasi-/strict-2D geometry can have more than one NESS - in contrast to quasi-/strict-1D extensile fluids which have been shown to posess only one NESS. Different NESS can be distinguished and characterised by measuring their steady state amplitudes $A(t \to \infty)$. In particular transitions from one steady state to another can be described as either continuous or discontinuous depending on how the value of $A(t \to \infty)$ changes across the phase boundary. This is analogous to first order and second order phase transitions in equilibrium thermodynamics.

In quasi-2D active fluids, we also learnt that the steady states are often characterised by a large out-of-plane velocity component. This large out-of-plane fluid flow is mutually accompanied by a large twist in the polarisation field. Finally in the case of swimming, these steady state patterns become travelling wave solutions. This travelling wave solution is perhaps the easiest case to verify experimentally by plotting the trajectory of one swimmer which will have a spiral motion (see Fig. 4.2(A)). The direction of wave is roughly in the same direction as the average polarisation. And if the swimming speed is large, we may also observe large density fluctuations.

Chapter 4

Designing a crawling cell using soft materials

Some eukaryotic cells have been observed to be able to move in various media. One obvious example is provided by the keratocyte cells which are able to crawl on a 2D substrate (such as glass slides) [25, 64]. Most notably, this crawling motion is often accompanied by lamellipodial protrusion - a thin sheet of actomyosin which extends from the cell body. Other types of cells, in particular tumour cells, can also move inside a 3D matrix (such as tissues and polymeric gels) [12]. Such abilities for cells to move can either be beneficial (*e.g.* in the case of wound healing [26, 27]) or pathological (*e.g.* in the case of tumour migration [16]). However despite its biological importance, some aspects of cell motility are still poorly understood.

In this chapter, we aim to build a minimal hydrodynamic model of a crawling cell using ideas from soft matter physics such as binary liquid and liquid crystals. The simplest model of a cell is probably just a droplet sitting on a surface. However, a passive droplet will not be able to move on its own. To make it move, we have to add some non-equilibrium physics into it. This is provided by actin polymerisation and actin-myosin contraction inside the cell cytoskeleton. Secondly, the actin filaments inside the cell cytoskeleton are also polarised to point roughly in the same direction. Thus we can also treat the filaments as *polar* liquid crystals with a macroscopic polarisation which points in the same direction of motion (crawling). Using this simple model, we are able to reproduce a thin layer of protrusion in a crawling droplet which is qualitatively similar to

lamellipodial protrusion in real biological cells. This hydrodynamic model of a crawling cell has some advantages over the microscopic ones (which have already existed since the past few decades). Our hydrodynamic model allows us to study cell motility over much larger lengthscales. For instance, our model can be used to predict different morphologies/shapes of a eukaryotic cell. This is in contrast to many microscopic models which typically only consider a single protein filament and thus cannot be used to work out the cell behaviour as a whole.

4.1 Different types of cell motility

The bulk of a eukaryotic cell is mostly made up of a complex network of protein filaments, called the cytoskeleton. This cytoskeleton provides a form of mechanical rigidity for the cell as well as a mean of transporting nutrients across the cell. Since the past two decades, the cell cytoskeleton (in particular the actomyosin part) has also been linked to various types of cell motility [33, 65]. This is already demonstrated in Fig. 1.3(B) of the introduction where an actomyosin extract can move independently of its parent cell.

The cell cytoskeleton consists of different types of protein filaments, cross-linked by various molecular motors and passive linking proteins. Closer to the cell nucleus, we normally find longer and stiffer filaments (*e.g.* microtubules and intermediate filaments) cross-linked by motor proteins (such as kinesins and dyneins). Whereas closer to the cell membrane, we usually find shorter and thinner filaments (actins) cross-linked by motor protesin (myosins). Throughout this thesis we shall mainly focus on the actomyosin due to its dominant role in cell motility [65, 33].

As already mentioned in the introduction, the actomyosin network constitutes an active fluid due to the presence of the following two active processes:

1. Actin polymerisation, and

2. Actin-myosin contraction

Firstly, an actin filament can grow/polymerise at the plus/barbed end and shrink/depolymerise at the minus/pointed end. Typically these actin filaments are also organised to point in the same direction (away from the cell nucleus, see red arrows in Fig. 4.1). Consequently, this coordinated growth of actin filaments

can cause a protrusion in the cell. Secondly, these actin filaments are also cross-linked together by motor proteins, called myosins. The motors are then able to pull the filaments together, causing them to contract. The role of actin-myosin contraction in cell motility is perhaps less clear than for polymerisation but we shall see in the next chapter that actin-myosin contraction alone can also create some directed motion through the formation of large scale fluid flow.

In some cases of cell motility, one of these two processes is more important than the other. For instance in cell crawling, we will show that actin polymerisation (plus focal adhesions) is sufficient to cause movement in the direction of actin polarisation – without any help from actin-myosin contraction. However in other case such as cell swimming, actin polymerisation may not be as effective. Below we are going to distinguish three most common types of cell motility: crawling, swimming and grabbing.

4.1.1 Crawling

Some cells have been known to spontaneously crawl on a 2D substrate such as glass slides [64, 25]. For example in Fig. 4.1(A), we have a keratocyte cell crawling on a glass slide. The crawling speed of keratocyte cells can reach up to $0.2\,\mu$m/s. Note that this speed also depends on how well the cell can 'stick' on the substrate (by forming focal adhesions). Also notice that the actin filaments (indicated by the red arrows in the figure) are, on average, polarised in the same direction of crawling. Furthermore, cell crawling is also accompanied by lamellipodial protrusion - a thin sheet of actomyosin which extends from the cell body (see Fig. 4.1(B)).

The mechanism of cell crawling is often desribed as follows. First the actin filaments form focal adhesions with the substrate (see Fig. 4.1(B)). This allows the filaments to stick to the substrate temporarily. Subsequently actin polymerisation at the plus end (arrow heads in the figures) pushes the cell membrane forward, therefore, creating lamellipodial protrusion. Note that the focal adhesions prevent the filaments from slipping back as they are pushing against the membrane. Finally actin-myosin contraction pulls the cell body towards the lamellipodium. Actually as we shall see later, actomyosin contraction is not necessary to pull the rear of the cell towards the front. A surface tension from the cell membrane is sufficient to do this.

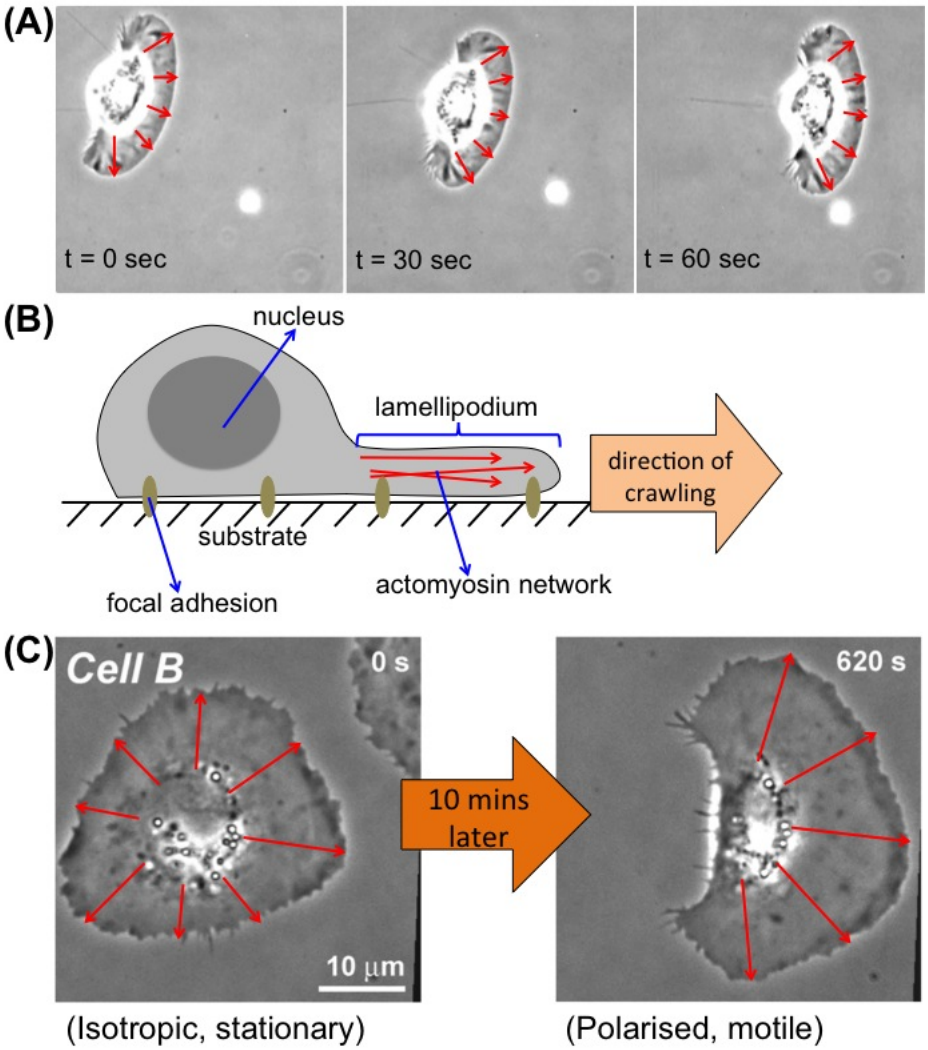

Figure 4.1: **Cell crawling.** **(A)** Keratocyte cell crawling on a 2D glass substrate (viewed from top). The crawling speed is around $\sim 0.2\,\mu$m/s. (Adapted from [10].) **(B)** View from the side showing lamellipodial protrusion in cell crawling. **(C)** On the left, the actin filaments are isotropically distributed and thus the cell is not moving. In order to move, the cell has to be polarised in the direction of motion (the symmetry has to be broken). (Adapted from [11].)

Accordingly, the actin filaments in the cell cytoskeleton have to be polarised globally in one direction in order for the cell to move. For example the cell in Fig. 4.1(C) left will not be able to move. This is because the actin filaments are distributed isotropically away from the nucleus. Therefore the polymerisation force from the filaments will pull the cell body isotropically in all direction, and as a result, there will be no net movement. Normally cells can detect the presence of a chemical gradient and signal the actin filaments to reorganise themselves to point towards the chemical/food source (chemotaxis). However in the case of keratocyte cells [11], an isotropic cell can still spontaneously become polarised (even in uniform chemical concentration) and starts to move in random direction (see Fig. 4.1(C)).

4.1.2 Swimming

Some other cells (such as the breast tumour cell in Fig. 4.2(A)) can also 'swim' in a straight line inside a 3D tissue or polymeric gel [12]. The swimming speed is typically around $\sim 1\,\mu$m/hr which is much smaller than that of crawling. We call this type of motion 'swimming' due to the following two properties: (i) unlike cell crawling, there is no solid surface present and (ii) there is no protrusion coming out from the cell (the cell shape remains roughly spherical as can be seen from the figure). This is in contrast to cell 'grabbing', described in the next subsection, in which the cell forms finger-like protrusion to move inside a 3D environment.

The lack of protrusion in swimming cells suggests that at least one of the following is true:

(i) Actin polymerisation/treadmilling is absent.

(ii) The actin filaments are not polarised (they are randomly distributed).

(iii) The polymerisation rate is not large enough to create a protrusion (this will be discussed further in Sec. 4.4).

(iv) There is a lack of focal adhesions which reduces the ability of the cell to form protrusion (see Sec. 4.4).

All these points indicate that actin polymerisation may be less involved in cell swimming - as compared to crawling and grabbing. Indeed as we shall see in the

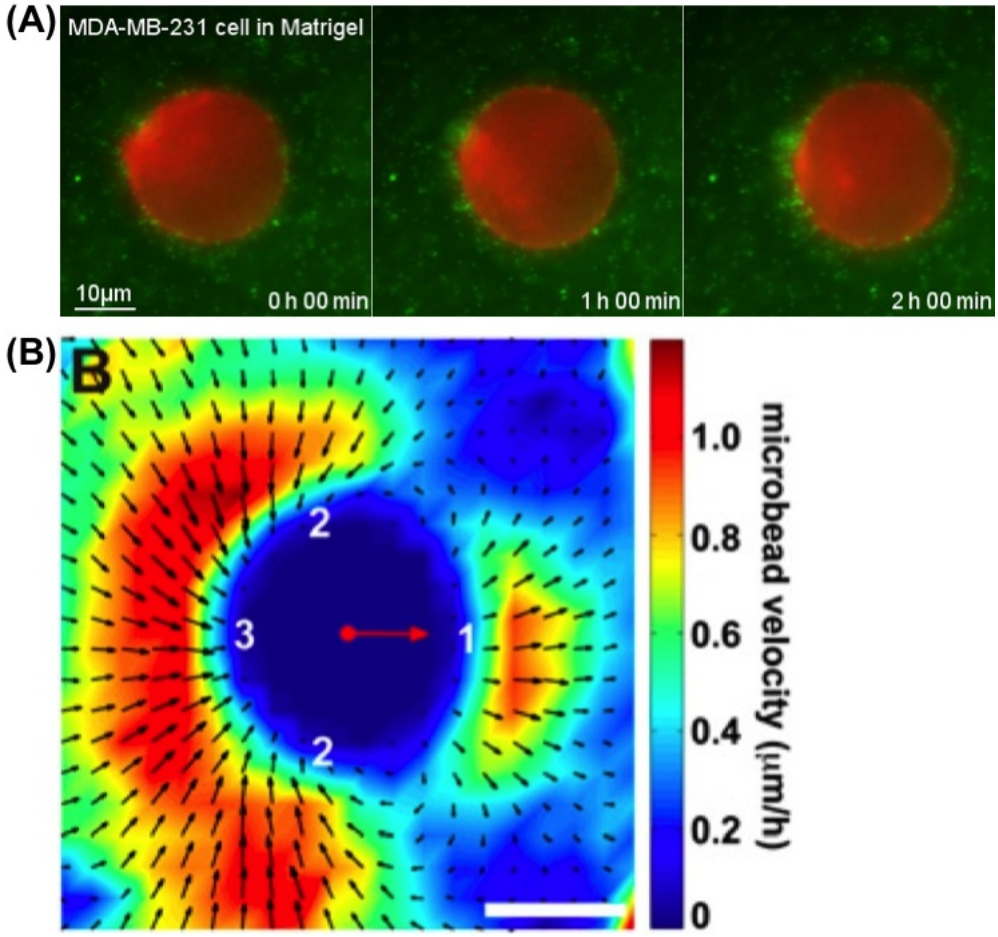

Figure 4.2: **Cell swimming.** **(A)** shows a breast tumour cell (MDA-MB-231) 'swimming' inside a 3D polymeric gel. Here the cell maintains a roughly spherical shape. The swimming speed ($\sim 1\,\mu$m/hr) is much slower compared to crawling. **(B)** shows the fluid velocity around the swimming cell. (Images adapted from [12].)

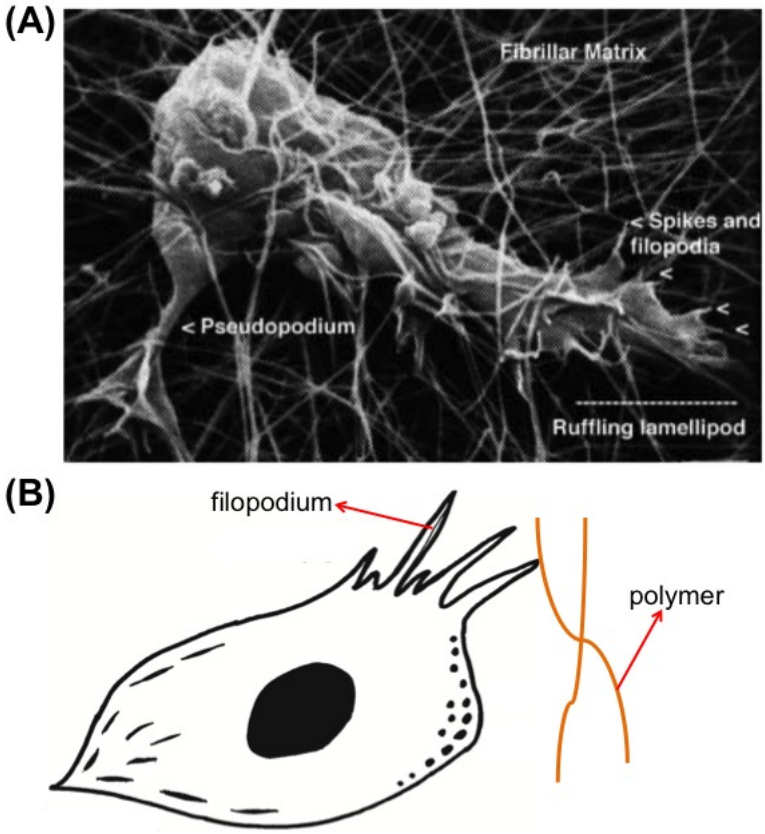

Figure 4.3: **Cell grabbing.** **(A)** a cell can also move inside a polymeric gel by 'grabbing' the polymers. (Adapted from [13]). **(B)** Here the cell forms a finger-like protrusion (filopodia) and the tip of the filopodium will then attach to a polymer *via* focal adhesion.

next chapter (also in Ref. [17]), there exists an alternative route(s) to cell motility without actin polymerisation.

Strictly speaking, tissues and polymeric gels are viscoelastic materials which behave like an elastic solid at short timescale and flow like a viscous liquid at longer timescale. The relaxation timescale for tissues, in particular, is between tens of seconds to several minutes [31]. For the tumour cell in Fig. 4.2, the time it takes for the cell to move a distance of its diameter is $\frac{20\,\mu\text{m}}{1\,\mu\text{m/hr}} = 20\,\text{hrs}$, which is much longer than the viscoelastic timescale. Therefore in cell crawling, we can treat the tissue/matrigel surrounding the cell as viscous fluid with viscosity in the range $10^3 - 10^5\,\text{Pa}\,\text{s}$ [66].

4.1.3 Grabbing

Some other tumour cells can also move around inside a 3D polymeric gel by forming finger-like protrusion (called filopodia [13], see Fig. 4.3). The mechanism for filopodial protrusion is quite similar to that of lamellipodial protrusion in cell crawling. Here, the actin filaments are bundled together and actin polymerisation at the plus end of the bundle forces a finger-like protrusion. These filopodia are then able to form focal adhesions with the polymers inside the gel. Subsequently, the cell contracts and move in the direction of that particular protrusion. In general, filopodia can form at any point on the cell's surface. Thus this type of motion is typically much more random as compared to cell swimming above. Also notice that the cell's shape changes continuously (compared to a swimming cell which remains roughly spherical).

4.2 Microscopic model: Brownian ratchet

In this chapter, we shall focus mainly on cell crawling on a 2D substrate, whereas, cell swimming in a 3D matrix will be discussed more in the next chapter. As already mentioned above, cell crawling is mainly driven by actin polymerisation pushing against the cell membrane. This active process can be described either microscopically using the Brownian ratchet model or macroscopically using the hydrodynamic theory of active fluid. The Brownian ratchet model is first used by Peskin *et al.* [67] in 1993 to describe the mechanism of cell crawling. In particular, the cell velocity can be derived from the polymerisation rate of the actin filaments and the surface tension of the cell membrane. In this section we shall study this microscopic derivation in more detail, in particular, we shall also look at some limitations of this microscopic model. But first, we consider actin polymerisation inside a free solution (not confined by a cell membrane).

4.2.1 Actin treadmilling

An actin filament (F-actin) can propel itself inside a solution of its monomers (G-actin) in a process called treadmilling [14]. As we know, actin filaments are polar with one end labelled the plus/barbed end and the other labelled the minus/pointed end (see Fig. 4.4(A)). Correspondingly, there are two types of

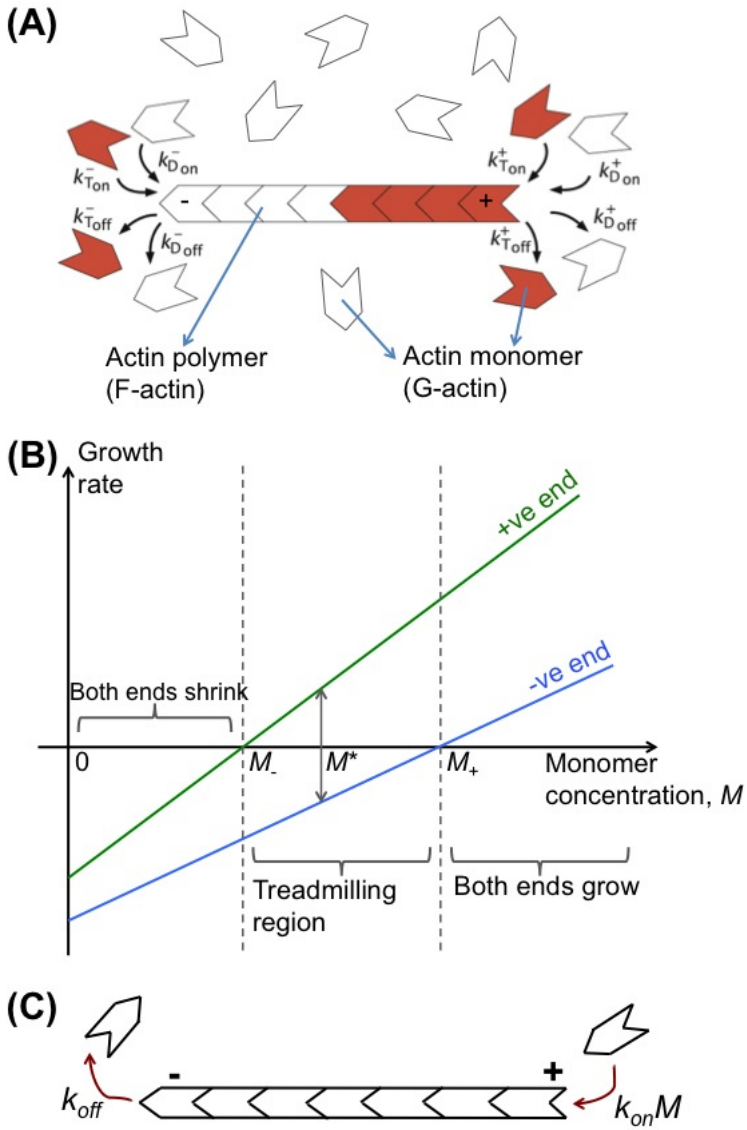

Figure 4.4: **(A)** Model of actin polymerisation and depolymerisation. ATP-bounded actin monomers are coloured red while ADP-bounded actin monomers are coloured white (adapted from [3]). **(B)** The growth rate for the plus (green line) and minus (blue line) ends of actin polymer as a function of monomer concentration M (adapted from [14]). **(C)** A simplified picture of actin treadmilling. Actin monomers polymerise at the plus end and depolymerise at the minus end (at the same rate). Overall, the filament appears to be swimming in the direction of polarisation (in the plus direction).

actin monomers: ATP-bound and ADP-bound actin monomer (distinguished by red and white colour respectively in the figure). Roughly speaking the ATP-bound monomers prefer to attach/polymerise at the plus end of the filament. And then along the filament, the ATP is converted into ADP (releasing chemical energy of $\sim 20\,k_BT$ in the process). Finally, the ADP-bounded monomers detach/depolymerise from the minus end. This process repeats itself and continues until the ATP are depleted from the solution. (In real cells, the ADP inside the actin monomers which have been used to release energy can be recharged in mitochondria to become ATP again.) Effectively the actin filament appears to be swimming in the direction of its polarity with speed = polymerisation rate $\times$ size of the actin monomer. This process is termed actin treadmilling.

However in reality, this process is usually much more complex [3]. Each type of actin monomers can polymerise/depolymerise at either end of the filament - each with a different rate constant k (see Fig. 4.4(A)). In total there are eight reaction rate constants associated with ATP/ADP-actin polymerisation/depolymerisation at either end of the filament. We can then write down the rate equations which determine the growth rate of the plus and minus end of actin filament. Fig 4.4(B) shows the plot of the growth rate of the plus end (green line) and the minus end (blue line) as a function of actin monomer concentration M. Below some critical concentration M_-, the growth rates of both the plus and minus ends are negative. This means that below this concentration, both ends of the actin filament shrink. On the other hand above some other critical concentration M_+, the growth rate of the plus and minus ends are both positive. This means both ends of the filament grow. Interestingly around some concentration M^*, the growth rate of the plus end is positive whereas the growth rate of the minus tip is negative. This means that the actin monomers polymerise at the plus end and depolymerise at the minus end which we identify this as the treadmilling regime.

Fig 4.4(C) shows a simplified picture of actin treadmilling. Actin treadmilling occurs if the concentration of the actin monomers is close to M^*. We shall assume that the polymerisation rate at the plus end ($k_{on}M$) is equal to that of depolymerisation at the minus tip (k_{off}). Consequently the treadmilling velocity of a free actin filament relative to the solvent is given by:

$$V_{free} = k_{on}Ma \tag{4.1}$$

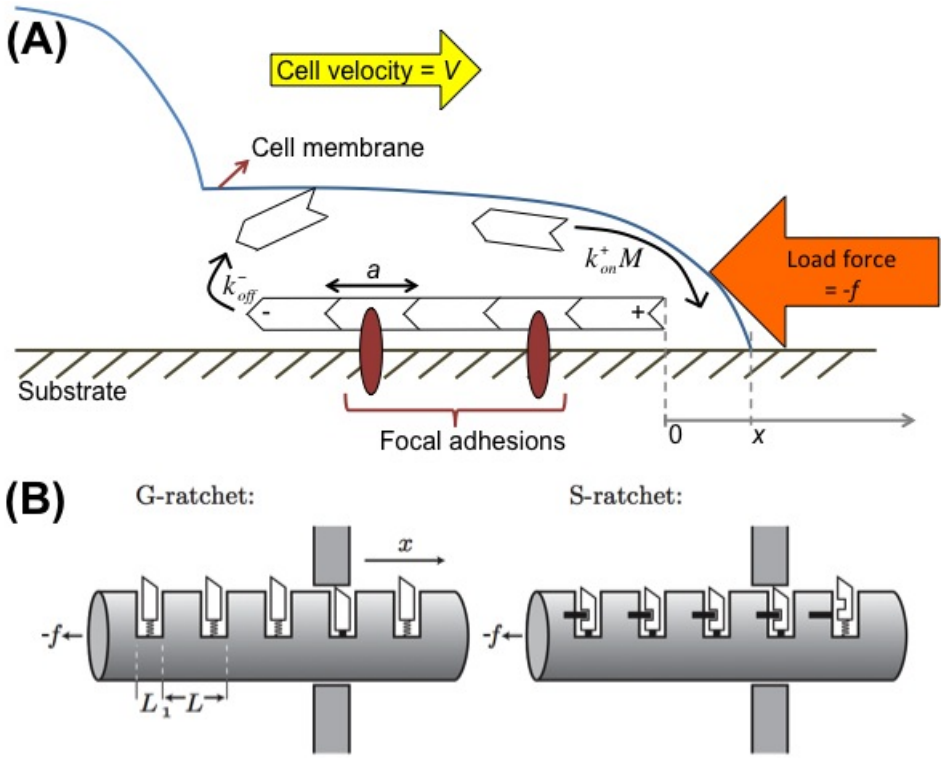

Figure 4.5: **(A)** Brownian ratchet mechanism. The membrane front (whose position is x from the tip of the filament) can diffuse freely. In order for actin monomer to polymerise at the tip of actin polymer, the membrane front has to diffuse at least a distance a from the tip of the filament. **(B)** The ratchet analogy. In his book, Nelson discussed a G-ratchet (left) versus an S-ratchet (right). The Brownian ratchet model in (A) corresponds to an S-ratchet. (image adapted from [15].)

where a is the size of the actin monomer and M is the concentration of actin monomers in the solution. In the case of cell crawling - which is also driven by the same treadmilling process - the cell velocity will actually be less than V_{free} in Eq. (4.1). This is because the filaments are polymerising against a load force from the cell membrane and also the filaments are not perfectly aligned in the same direction ($|p| < 1$).

4.2.2 Brownian ratchet

In this subsection, we review the microscopic derivation of Peskin *et al.* [67] based on Brownian ratchet. We consider a eukaryotic cell crawling on a substrate with some velocity V pushing against a load force $-f$ as shown in Fig. 4.5(A). The

negative sign indicates that the applied load force is in the opposite direction to the cell velocity V. This load force can be in a form of surface tension from the membrane or an external one. In either case, we shall assume that f is constant over the polymerisation timescale. Also on average, the actin filaments are polarised in the same direction as V (which is to the right in Fig. 4.5(A)).

In this microscopic derivation, we shall consider a single actin filament (Fig. 4.5(A)) being held stationary relative to the substrate *via* focal adhesions. The actin monomers make some polymerisation attempts at the plus end of the filament at a rate $k_{on}M$ - where M is the monomer concentration. Alternatively, we may also define the polymerisation timescale to be: $\tau_{on} = \frac{1}{k_{on}M} \sim 0.01\,\mathrm{s}$ [68] such that the actin monomer makes one polymerisation attempt every τ_{on} seconds. In addition, actin monomers also depolymerise from the minus end of the filament at a rate k_{off}. In order for the polymerisation attempt to be successful, the front of the cell membrane has to diffuse by at least a distance a relative to the tip of the filament. This is to allow an actin monomer (whose size is a) to fit in the gap between the tip of the filament and the cell membrane (see figure). The resulting velocity of the cell will then be less than the treadmilling velocity of a free actin filament: $V < V_{free}$. Following Peskin *et al.*, we shall derive microscopically the cell velocity as a function of applied force $V(f)$.

Let $x > 0$ be the position of the membrane relative to the polymerising tip of the filament and $P(x,t)$ be its probability distribution. The time evolution of $P(x,t)$ is governed by the Fokker-Planck equation:

$$\frac{\partial P}{\partial t} + \frac{\partial J}{\partial x} = 0 \tag{4.2}$$

with the probability current given by:

$$J = \underbrace{-D\frac{\partial P}{\partial x}}_{\text{diffusion}} + \underbrace{Pv}_{\text{drift}} \tag{4.3}$$

(Note that the probability density is normalised to one: $\int_0^\infty P(x,t)\,dx = 1$.) The first term in the probability current is the diffusive flux due to thermal fluctuations with D as the diffusion constant of the membrane. The second term is the drift current with v as the drift velocity. We may relate v to the external force $-f$

via:

$$\begin{aligned} -f &= \gamma v \\ &= \frac{k_B T}{D} v \end{aligned} \tag{4.4}$$

where γ is the coefficient of friction between the membrane and the substrate. Notice that we have used Einstein's relation in the last line of the equations above.

Finally we assume the diffusion timescale of the membrane (τ_D) to be much faster than that of polymerisation (τ_{on}) - with τ_D being defined to be the time it takes by the membrane to diffuse a distance a. (Note that $\tau_D \sim (10^{-3} - 10^{-6})$ s compared to $\tau_{on} \sim 0.01$ s [65].) Therefore we can assume a steady state probability in which the probability current is constant:

$$\begin{aligned} J &= C \\ -D\frac{dP}{dx} - \frac{Df}{k_B T} P &= C \end{aligned} \tag{4.5}$$

where C is a constant. The solution of which is:

$$P(x) = \frac{f}{k_B T} \exp\left(-\frac{fx}{k_B T}\right) \tag{4.6}$$

In order for the actin monomer to polymerise at the plus end, the membrane has to diffuse at least a distance a from the tip of the filament. The probability of this happening within time τ_{on} is given by:

$$\begin{aligned} P(x > a) &= \int_a^\infty P(x)\, dx \\ &= \exp\left(-\frac{fa}{k_B T}\right) \end{aligned} \tag{4.7}$$

Notice that there is no dependence on τ_{on} above because we assume the probability distribution has reached steady state faster than τ_{on}. Finally the velocity of the cell is then

$$\begin{aligned} V(f) &= \frac{a \times P(x > a)}{\tau_{on}} \\ &= \underbrace{k_{on} M a}_{V_{free}} \exp\left(-\frac{fa}{k_B T}\right) \end{aligned} \tag{4.8}$$

Putting $k_{on}M = 100\,\mathrm{s}^{-1}$, $a = 3\,\mathrm{nm}$, and $f = 1\,\mathrm{pN}$ [67], we obtained a reasonable estimate of the cell's velocity: $V \simeq 0.15\,\mu\mathrm{m}/s$. However there are also some limitations to the Brownian ratchet model above. The Brownian ratchet model predicts that the cell's velocity V should decrease exponentially with the load force f. In other words, the shape of the curve $V(f)$ is concave up for all range of f. However repeated experiments on keratocyte cells [69, 70] show that the curve $V(f)$ looks more like a concave down. This may be due to the fact that only one actin filament is considered throughout the microscopic derivation. The interactions between the actin filaments, for instance, are not accounted for in this Brownian ratchet model.

In his book, Nelson [15] provides a ratchet analogy to the crawling mechanism that was described above. Fig. 4.5(B) shows two distinct cylindrical ratchets passing through a hole (a G-ratchet and an S-ratchet). Each cylindrical ratchet contains a series of triangular teeth which are pointed to the right. These teeth, when they are fully released, will prevent the cylinder from going to the left (see figure). In the G-ratchet (picture on the left), the teeth are only held by springs. At first, we might think that thermal fluctuations in the cylinder may allow the cylinder to move to the right but not to the left (since the teeth on the right hand side of the hole prevents the cylinder from going in that direction). However this becomes a perpetual motion which continuously converts thermal energy into work done against the springs and Feynman [71] showed that this is not possible. The Brownian ratchet model of cell crawling that was described above actually corresponds to an S-ratchet (shown in the picture on the right). The difference from the G-ratchet is that the teeth are held by an active bolt which automatically opens when the cylinder passes through the hole to the right. In this case, the cylinder will be able to move to the right indefinitely.

4.3 Hydrodynamic model: active droplet

The Brownian ratchet model above calculates the cell velocity by considering a single actin filament polymerising against the cell's membrane. However as we have seen from the previous chapter, cooperative behaviour between the active particles (actin filaments and motor proteins in this case) can also give rise to large scale fluid vortices. To account for this hydrodynamic interaction between

the filaments, we shall now introduce an alternative model of cell crawling based on the hydrodynamic theory of active fluid [57, 72]. More specifically, we consider a droplet of active matter (*i.e.* actomyosin) as a simple representation of a cell crawling on a solid substrate. In reality, a eukaryotic cell contains more than just actomyosin; it also contains microtubules, nucleus and other macromolecules. However since cell crawling is often characterised by lamellipodial protrusion, which is made up mostly of actomyosin, a droplet of just actomyosin provides a reasonable approximation to cell crawling. In particular, we are able to reproduce a thin layer of protrusion from the droplet, similar to lamellipodial protrusion in real cells.

Note that in our hydrodynamic model below, we approximate the cell membrane by a liquid-liquid interface with some effective surface tension $\widetilde{\gamma}$. This surface tension (which is positive) represents the energy costs of increasing the surface area of the cell. In this binary liquid representation, we have thus neglected the bending rigidity associated with lipid bilayer in the cell membrane.

4.3.1 Actin-myosin contraction

The process of actin treadmilling is similar to that of swimming in self-propelled particles and thus actin treadmilling is a type of active or non-equilibrium process (consuming energy from ATP→ADP conversion). More importantly, this actin-treadmilling process (plus a sufficient amount of focal adhesions) causes the cell to move in the direction of average orientation of the actin filaments (see Brownian ratchet above). And if the actin polymerisation rate is large enough, this can also create a lamellipodial protrusion as commonly observed in cell crawling (this will be discussed more in the next section). Apart from actin treadmilling, there is actually another active process inside the cell cytoskeleton: actin-myosin contraction. The role of actomyosin contraction in cell crawling is perhaps not as obvious as actin treadmilling. However as we shall see from the next chapter, actin-myosin contraction can also give rise to a translational motion (without any actin polymerisation/treadmilling involved). This may provide an alternative route to cell motility in 3D environment such as swimming, in which protrusion is not always observed. Hydrodynamically, the processs of actomyosin contraction generates an internal active stress which can be shown to be contractile [73]. The arguments for which are presented below.

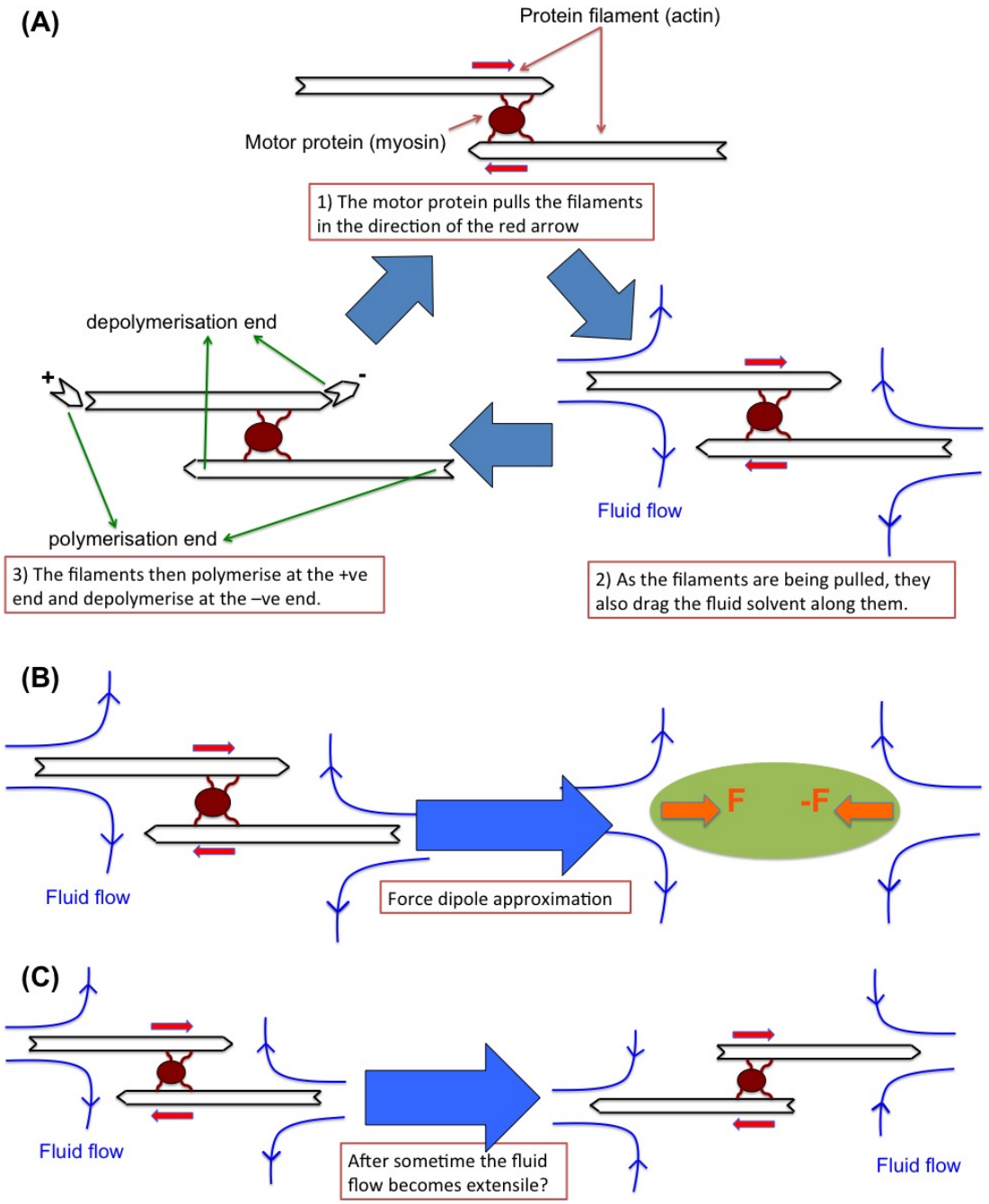

Figure 4.6: **Actin-myosin contraction.** **(A)** The active process of actin-myosin contraction inside eukaryotic cells. **(B)** The whole process of actin-myosin contraction can be approximated to first order as a contractile force dipole. **(C)** However if we allow the motor to continue pulling, the flow generated will become extensile (see main text for discussion).

The process of actin-myosin contraction is described in Fig. 4.6(A). For simplicity, we only consider two actin filaments cross-linked by a motor protein (myosin). The motor pulls the filaments together (in the direction of the red arrows), causing them to contract. As the filaments are pulled towards the centre, they also drag the fluid around them and thus create a quadrupolar fluid flow (shown by the blue lines in the figure). Comparing this fluid flow to the ones in Fig. 1.4 in the introduction, we recognize that the whole process can be approximated as a contractile force dipole (see Fig. 4.6(B)). Consequently, the active contribution to the hydrodynamic stress due to actomyosin contraction is similar to the contractile active stress that we derived in the previous chapter:

$$\sigma^a_{\alpha\beta} = -\zeta c p_\alpha p_\beta \tag{4.9}$$

where $\zeta < 0$ for contractile and $|\zeta|$ is proportional to the strength of the pulling force. c is the concentration of the actin-myosin pairs. As usual, the Greek indices indicate the Cartesian coordinates.

Note that the force dipole is only a first order approximation to the whole process of actomyosin contraction. The actin filament, for instance, can also be cross-linked by more than one motor protein. Furthermore if we look closely at the cartoon, the action of a motor protein pulling the filaments will, at some point, generate an extensile stress (see Fig. 4.6(C)). On the other hand we also know that the actomyosin network inside the cell cytoskeleton is generally contractile rather than extensile [74]. One simple explanation to the observed behaviour is that the motors can cleverly attach to or detach from the filaments. Another explanation is due to Lenz *et al.* [75, 76] who suggest that the actin filaments tend to buckle under contractile stress. In this case the contractile flow (in Fig. 4.6(C) left) is favoured over the extensile flow (in Fig. 4.6(C) right) (also see Liverpool *et al.* [73]).

4.3.2 Hydrodynamic equations

We consider a droplet of actomyosin as a simple representation of a crawling cell. Inside the droplet, the filaments are assumed to be polarised in one direction, which is in the direction of motion. In the hydrodynamic limit, the dynamics of actin filaments and motors inside the droplet can be described by a few

hydrodynamic fields. These coarse-grained fields of interest are:

(i) the concentration of active material (*i.e.* actomyosin) $c(\mathbf{r}, t)$,

(ii) the polarization field $\mathbf{p}(\mathbf{r}, t)$ which indicates the average orientation of the filaments and finally

(iii) the fluid velocity $\mathbf{u}(\mathbf{r}, t)$.

The droplet is defined such that the concentration of the active matter is finite inside ($c > 0$) and zero outside ($c = 0$). Furthermore since the actin filaments are also polarised, we define the polarization to be finite inside the droplet ($\mathbf{p} \neq 0$) and zero/isotropic outside ($\mathbf{p} = 0$).

To stabilise a droplet with *polar* liquid crystalline phase we introduce a free energy functional as follows:

$$\begin{aligned} F[c, \mathbf{p}] \;=\; & \int d^3r \left\{ V(c) + \frac{k}{2} |\nabla c|^2 \right. \\ & \left. - \frac{\alpha}{2} \frac{(c - c_r)}{c_r} |\mathbf{p}|^2 + \frac{\alpha}{4} |\mathbf{p}|^4 + \frac{\kappa}{2} (\nabla \mathbf{p})^2 + \beta \mathbf{p} \cdot \nabla c \right\} \end{aligned} \tag{4.10}$$

where the potential $V(c)$ has the double well form (Landau potential):

$$V(c) = \frac{a}{4c_r^2} c^2 (c - c_0)^2 \tag{4.11}$$

The minima of this potential are at $c = 0$ and $c = c_0 > 0$ which roughly correspond to the equilibrium values of the concentration field inside and outside the droplet respectively. (The actual equilibrium values of c are calculated by minimising the total free energy.) And then the term proportional to the concentration gradient squared describes an interfacial energy with the proportionality constant $k > 0$ related to the surface tension.

Next, we also have terms proportional to $|\mathbf{p}|^2$ and $|\mathbf{p}|^4$ which describe equilibrium isotropic to polar transition. $\alpha > 0$ is a phenomenological constant which is taken to be positive for stability. Notice that the coefficient of $|p|^2$ changes its sign from positive (isotropic phase) to negative (polar phase) as the concentration of the filaments goes above some critical concentration c_r. We set $0 < c_r < c_0$ so that the interior of the droplet favours polar phase whereas the exterior favours isotropic phase. The second last term propotional to $(\nabla \mathbf{p})^2$

describes the energy penalty due to elastic deformation in the liquid crystalline phase (inside the droplet) with $\kappa > 0$ as the elastic constant. (We assume single elastic constant approximation.)

The equilibrium values of c and $\mathbf{p}$ are obtained by minimising the total free energy in a state of uniform c and $\mathbf{p}$: $\frac{\delta F}{\delta c} = 0$ and $\frac{\delta F}{\delta \mathbf{p}} = 0$. The solutions of which correspond to the passive isotropic phase outside the droplet ($c = 0$, $\mathbf{p} = 0$) and the active polar phase inside the droplet ($c = c_{eq}$, $\mathbf{p} = \mathbf{p}_{eq}$) . In the special case of $c_r = c_0/2$, the expression for c_{eq} and $\mathbf{p}_{eq}$ are:

$$c_{eq} = \frac{c_0}{2} + \frac{c_0}{2}\sqrt{1 + \frac{\alpha}{2a}} \tag{4.12}$$

$$\mathbf{p}_{eq} = \left(1 + \frac{\alpha}{2a}\right)^{1/4} \hat{\mathbf{p}} \tag{4.13}$$

where $\hat{\mathbf{p}}$ is a unit vector indicating the direction of symmetry breaking in the isotropic-to-polar transition. The resulting surface tension γ will depend on a, k, as well as the elastic constant κ. Across the droplet interface, the values of the concentration and polarisation fields vary smoothly from $c = c_{eq}$ and $\mathbf{p} = \mathbf{p}_{eq}$ to $c = 0$ and $\mathbf{p} = 0$. In general, the width of this diffuse interface also depends on a, k and κ. In our simulations, the interfacial width is typically much smaller than the size of the droplet.

Finally the last term in the free energy, $\beta \mathbf{p} \cdot \nabla c$, represents a soft anchoring of $\mathbf{p}$ to the droplet interface. For nonzero value of β, the polarisation field $\mathbf{p}$ will tend to align perpendicularly to the droplet interface. The preferred direction of $\mathbf{p}$ can either point perpendicularly outwards ($\beta > 0$) or inwards ($\beta < 0$).

The time evolutions of the hydrodynamic fields can be derived phenomenologically, in similar fashion to the previous chapter. Since the total number of active particles (actomyosin) is approximately conserved [1], the time evolution of the concentration field $c(\mathbf{r}, t)$ can be written as a convective-diffusion equation:

$$\frac{\partial c}{\partial t} + \nabla \cdot \left(c(\mathbf{u} + w\mathbf{p}) - M \nabla \frac{\delta F}{\delta c} \right) = 0 \tag{4.14}$$

[1] Note that we assume the lengths of the actin filaments have somehow stabilised over the hydrodynamic timescale, *i.e.* actin polymerisation at the plus end is balanced by actin depolymerisation at the minus end.

where the terms inside $\nabla\cdot(\ldots)$ is the concentration current which has three parts: (i) convection by the fluid solvent $c\mathbf{u}$, (ii) self-advection due to actin treadmilling $cw\mathbf{p}$ and (iii) passive diffusion $-M\nabla\frac{\delta F}{\delta c}$. The parameter M is the mobility, related to the diffusion constant of the particles by $D \simeq Ma$. And then we also have an activity parameter w (also called self-advection) which is roughly equal to the treadmilling speed of a *free* actin filament relative to the solvent (V_{free}, see Sec. 4.2.1). A nonzero value of w will cause the actomyosin droplet to move in the direction of the polarisation. However the velocity of the droplet itself will be less than w due to effect of the surface tension which resists any increase in the interfacial area of the droplet.

The dynamics of the polarisation field $\mathbf{p}(\mathbf{r},t)$ is borrowed from polar liquid crystal theory, and can be written as (see [35]):

$$\frac{\partial\mathbf{p}}{\partial t} + (\mathbf{u}+w\mathbf{p})\cdot\nabla\mathbf{p} = -\underline{\underline{\Omega}}\cdot\mathbf{p} + \xi\underline{\underline{v}}\cdot\mathbf{p} - \frac{1}{\Gamma}\frac{\delta F}{\delta\mathbf{p}} \tag{4.15}$$

where $\underline{\underline{v}}$ and $\underline{\underline{\Omega}}$ are the symmetric and anti-symmetric parts of the velocity gradient tensor $\nabla\mathbf{u}$. Γ is the rotational viscosity and ξ is a shape factor related to the geometry of the active particles: $\xi > 0$ for rod-like particles and $\xi < 0$ for oblate particles. Here we take ξ positive as seems appropriate for filamentary contractile matter such as actin networks. The parameter ξ also determines whether the particles are shear-aligning (for $|\xi| > 1$) or shear-tumbling (for $|\xi| < 1$). In this thesis we assume $\xi > 1$.

Momentum balance in our system is enforced through the incompressible Navier-Stokes equation,

$$\begin{aligned} \nabla\cdot\mathbf{u} &= 0 \\ \rho\left(\frac{\partial}{\partial t} + \mathbf{u}\cdot\nabla\right)\mathbf{u} &= -\nabla P + \eta\nabla^2\mathbf{u} + \nabla\cdot\left(\underline{\underline{\sigma}}^p + \underline{\underline{\sigma}}^a\right) \end{aligned} \tag{4.16}$$

where P is the isotropic pressure and η is the viscosity; we have assumed single viscosity approximation. (In general there are more than one shear viscosities associated with the liquid crystalline phase depending on the alignment of the liquid crystals with respect to the shear flow [35]). There are two contributions to the hydrodynamic stress: active/non-equilibrium $\underline{\underline{\sigma}}^a$ and passive/equilibrium $\underline{\underline{\sigma}}^p$. The active stress comes from the dipolar force due to actin-myosin contraction

and has the form:

$$\sigma^a_{\alpha\beta} = -\zeta c p_\alpha p_\beta \tag{4.17}$$

Here ζ is the activity parameter which is negative for contractile particles (pullers) and positive for extensile particles (pushers). The magnitude of the activity $|\zeta|$ is proportional to the strength of the dipolar force. In the case of actomyosin ζ is negative, indicating contractile. (Note that the active stress above is only nonzero if $\zeta \neq 0$ and the polarisation field is not uniform, *ie.* splayed/bent.) The passive stress $\underline{\underline{\sigma}}^p$ consists of an elastic stress due to elastic deformation in the liquid crystalline phase and a surface tension: $\underline{\underline{\sigma}}^p = \underline{\underline{\sigma}}^{elastic} + \underline{\underline{\sigma}}^{interface}$. The elastic stress tensor has the same form as that in liquid crystals literature [35]:

$$\sigma^{elastic}_{\alpha\beta} = \frac{1}{2}(p_\alpha h_\beta - p_\beta h_\alpha) - \frac{\xi}{2}(p_\alpha h_\beta + p_\beta h_\alpha) - \kappa \partial_\alpha p_\gamma \partial_\beta p_\gamma \tag{4.18}$$

where $h_\alpha = -\frac{\delta F}{\delta p_\alpha}$ is the molecular field. The interfacial stress between the passive and active phase is similar to that of binary liquid [77] and has the following form:

$$\sigma^{interface}_{\alpha\beta} = \left(f - c\frac{\delta F}{\delta c} \right) \delta_{\alpha\beta} - \frac{\partial f}{\partial(\partial_\beta c)} \partial_\alpha c \tag{4.19}$$

where f is the free energy density.

The passive hydrodynamic stress/Ericksen stress $\sigma^p_{\alpha\beta}$ can also be derived in the following way (see Julicher *et al.* [57] for more details). Suppose we translate a volume of material by a small amount (by stretching it for instance),

$$c(\mathbf{r}) \rightarrow c(\mathbf{r} - \delta\mathbf{r}) \tag{4.20}$$

$$\mathbf{p}(\mathbf{r}) \rightarrow \mathbf{p}(\mathbf{r} - \delta\mathbf{r}) \tag{4.21}$$

The corresponding change in the material volume is $V \to V + \delta V$ and the change in the free energy due to this elastic deformation is

$$\begin{aligned}
\delta F &= \int_{V+\delta V} dV\, f(c+\delta c, \nabla c + \delta\nabla c, \mathbf{p}+\delta\mathbf{p}, \nabla\mathbf{p}+\delta\nabla\mathbf{p}) \\
&\quad - \int_V dV\, f(c, \nabla c, \mathbf{p}, \nabla\mathbf{p}) \\
&\quad \vdots \\
&= \oint_{\partial V} dS_\beta \left\{ (f-\mu c)\delta_{\alpha\beta} - \frac{\partial f}{\partial(\partial_\beta c)}\partial_\alpha c - \frac{\partial f}{\partial(\partial_\beta p_\gamma)}\partial_\alpha p_\gamma \right\} \delta r_\alpha \\
&\quad + \int_V dV \left\{ c\partial_\alpha \mu + h_\beta \partial_\alpha p_\beta \right\} \delta r_\alpha
\end{aligned} \tag{4.22}$$

where $\mathbf{h} = -\frac{\delta F}{\delta \mathbf{p}}$ is the molecular field and $\mu = \frac{\delta F}{\delta c}$ is the chemical potential. However we also know that the change in the free energy density can be written as (see Landau-Lifshitz [78]):

$$\begin{aligned}
\delta f &= -s\delta T + \sigma^p_{\alpha\beta}\epsilon_{\alpha\beta} \\
&= \sigma^p_{\alpha\beta}\frac{\partial \delta r_\alpha}{\partial r_\beta}
\end{aligned} \tag{4.23}$$

where s is the entropy density and $\epsilon_{\alpha\beta} = \partial\delta r_\alpha/\partial r_\beta$ is the strain tensor. (Physically the term $\sigma^p_{\alpha\beta}\epsilon_{\alpha\beta}$ is like the work done on the system by the surrounding.) In the last line, we have assumed the temperature T to be constant (isothermal process). The total change in the free energy is then

$$\begin{aligned}
\delta F &= \int \sigma^p_{\alpha\beta}\frac{\partial \delta r_\alpha}{\partial r_\beta}\, dV \\
&= \oint \sigma^p_{\alpha\beta}\delta r_\alpha\, dS_\beta - \int (\partial_\beta \sigma^p_{\alpha\beta})\delta r_\alpha\, dV
\end{aligned} \tag{4.24}$$

We can now compare Eqn. (4.22) to Eqn. (4.24). From the $\oint d\mathbf{S}$ terms, we obtain the Ericksen stress:

$$\sigma^p_{\alpha\beta} = \underbrace{(f-\mu c)\delta_{\alpha\beta} - \frac{\partial f}{\partial(\partial_\beta c)}\partial_\alpha c}_{\text{surface tension}} \underbrace{-\frac{\partial f}{\partial(\partial_\beta p_\gamma)}\partial_\alpha p_\gamma}_{\text{elastic stress}} \tag{4.25}$$

which consists of elastic and interfacial stresses (*cf.* Eqns. (4.18-4.19)). Actually the elastic stress in Eqn. (4.18) also contains terms proportional to $\frac{1}{2}(p_\alpha h_\beta - p_\beta h_\alpha)$ and $\frac{1}{2}(p_\alpha h_\beta + p_\beta h_\alpha)$. These can be obtained separately through torque balance (see appendix B). Finally comparing the $\int dV$ terms, we obtain the Gibbs-Duhem relation:

$$\partial_\beta \sigma^p_{\alpha\beta} = -c\partial_\alpha \mu - h_\beta \partial_\alpha p_\beta \tag{4.26}$$

The derivation above can also be easily extended to a free energy functional which depends on more than one order parameter (such as $\mathbf{p}$ and $\underline{\underline{\mathbf{Q}}}$).

Using the Gibbs-Duhem relation above (4.26), we can also write the momentum balance equation in (4.16) as

$$\rho\left(\frac{\partial}{\partial t} + \mathbf{u}\cdot\nabla\right)\mathbf{u} = -\nabla P + \eta\nabla^2\mathbf{u} + \nabla\cdot\underline{\underline{\sigma}}^a - c\nabla\mu - \mathbf{h}\cdot\nabla\mathbf{p} \tag{4.27}$$

This has some numerical advantages and disadvantages. First of all, writing the Ericksen stress as a force density $\sim -c\nabla\mu - \mathbf{h}\cdot\nabla\mathbf{p}$ has been shown to reduce spurious velocities in the hybrid lattice Boltzmann scheme [79]. On the other hand, since the conservation of momentum is not explicitly stated, this can also cause some losses in the global momentum numerically.

4.3.3 Choice of parameters

To establish an approximate correspondence between the natural simulation units (lattice Boltzmann units) and those of typical cell experiments, we choose the length-scale, time-scale and force-scale to be: $L = 1\,\mu$m, $T = 10\,$ms, and $F = 100\,$nN respectively. In lattice Boltzmann/simulation units these three scales are all defined to be equal to one exactly: that is, the lattice parameter is taken as the unit of length and the timestep the unit of time. The variables and parameters used in our model are given in the Table 4.1 with their respective values in simulation and physical units. These parameters have been chosen to be roughly in the same order of magnitude to the ones quoted in [18, 19]. Note that, in line with standard practice in lattice Boltzmann simulations, we chose the fluid mass density ρ to be much larger than the actual mass density of a real solvent (water) [80]. This is acceptable so long as the role of inertia (characterized by the Reynolds number) remains small; the procedure speeds up the computations

Model variables and parameters	Simulation units	Physical units
Effective shear viscosity, η	5/3	$1.67\,\mathrm{kPa}\cdot\mathrm{s}$
Effective elastic constant, κ	0.04	$4\,\mathrm{nN}$
Shape factor, ξ	1.1	dimensionless
Treadmilling speed, w	$0-0.03$	$3\,\mu\mathrm{m/s}$
Average concentration of actomyosin, c_0	2	$2\,\mu\mathrm{m}^{-3}$
Critical concentration, c_r	1	$1\,\mu\mathrm{m}^{-3}$
Effective diffusion constant, $D = Ma$	0.007	$0.7\,\mu\mathrm{m}^2/\mathrm{s}$
Rotational viscosity, Γ	1	$1\,\mathrm{kPa}\cdot\mathrm{s}$
Activity, $\lvert\zeta\rvert$	$0-0.01$	$(0-1)\,\mathrm{nN}\cdot\mu\mathrm{m}$
Surface tension (approximate), $\widetilde{\gamma}$	0.05	$5\,\mathrm{nN}/\mu\mathrm{m}$
Mass density, ρ	1	$10^{12}\,\mathrm{kg/m}^3$

Table 4.1: Typical values of the physical quantities used in our simulations. This choice of parameters are made to be consistent to other physical estimates in [18, 19].

by several orders of magnitude. The choice of the force density scale above gives the Reynolds number of about $Re \simeq 0.03$ which is small enough for the flow to be laminar though much larger than the actual experimental value which is of the order of $Re \sim 10^{-12}$.

4.4 Protrusion transition in cell crawling

Having established a hydrodynamic model of active droplet above, we shall now investigate the effect of activity on the behaviour of a droplet sitting on a solid surface. Recall that there are two active processes inside a droplet of actomyosin:

(i) actin polymerisation/treadmilling, which is quantified by the self-advection parameter $w \geq 0$ in our coarse-grained model and

(ii) actin-myosin contraction, which can be quantified by the activity parameter $\zeta \leq 0$.

Note that ζ is negative (contractile) for actomyosin systems. In the case of $w = 0$ and $\zeta = 0$ we recover an equilibrium/passive droplet which assumes a half-spherical shape (for the case of neutral wetting condition, which is adopted throughout this thesis). Afterwards, we consider some non-zero values of w and ζ which effectively forces the droplet to be out-of-equilibrium. As we shall see in this

chapter and also the next chapter, the presence of these two active processes can produce some deformations both in the polarisation field as well as in the droplet shape. In particular, when we localise the treadmilling effect to a small region of the droplet, this can create a thin layer protrusion similar to lamellipodial protrusion in real crawling cells as we shall see below.

4.4.1 Boundary condition at the substrate

To emulate focal adhesions which prevent the filaments from slipping, we apply non-slip boundary condition at the substrate ($z = 0$):

$$\mathbf{u}(z = 0) = 0 \tag{4.28}$$

If the focal adhesions were absent, we will have instead a slip boundary condition[2],

$$\begin{aligned} u_\perp(z = 0) &= 0 \\ \left.\frac{du_\parallel}{dz}\right|_{z=0} &= 0 \end{aligned} \tag{4.29}$$

where $u_\perp$ is the velocity component perpendicular to the substrate (*i.e.* u_z) and $u_\parallel$ is the velocity component parallel to the substrate (*i.e.* u_x and u_y). Experimentally, the focal adhesions can be weakened by coating the glass slide by some enzyme before putting the keratocyte cell on top [10]. Therefore ideally in our simulations, we will also need a mixture of non-slip and full-slip boundary condition. Mathematically we define the partial slip condition to be (see Wolff *et al.* [50]):

$$\begin{aligned} u_\perp(z = 0) &= 0 \\ \frac{u_\parallel(z = 0)}{u'_\parallel(z = 0)} &= 3\eta\frac{s}{1 - s} \end{aligned} \tag{4.30}$$

where s is the 'slip parameter' defined such that: $s \to 0$ corresponds to non-slip condition and $s \to 1$ corresponds to full-slip condition. Correspondingly we can think of $1/s$ as the amount of focal adhesions that the cell makes with the

[2]This is because the cell membrane prevents the fluid inside the cell to be in direct contact with the surface. Thus effectively, there will be a thin layer of water/air between the cell and the surface which allows the cell membrane to slip relative to the surface.

substrate - if there is less focal adhesion, the filaments are more likely to slip. Numerical implementation of the partial-slip condition is already discussed in chapter 2.

The boundary condition for the polarisation $\mathbf{p}$ is taken to be a strong anchoring, parallel to the substrate, *i.e.*

$$\begin{aligned} p_\perp(z=0) &= 0 \\ \left.\frac{\partial p_\parallel}{\partial z}\right|_{z=0} &= 0 \end{aligned} \tag{4.31}$$

This is because close to the surface, the actin filaments tend to align parallel to the surface due to focal adhesions (see Fig. 4.5(A)). The boundary condition between the polarisation field $\mathbf{p}$ and the droplet interface, on the other hand, is provided by a coupling term $\sim \beta\mathbf{p}\cdot\nabla c$ in the free energy (soft anchoring, see Eq. 4.10). For positive values of the coupling parameter $\beta > 0$, the polarisation field will tend to point perpendicularly outwards from the droplet interface and for negative values $\beta < 0$, the polarisation field will tend to point perpendicularly inwards. In the case of cell crawling, the actin filaments are normally pointed outwards and therefore we need to have $\beta > 0$.

And finally, the boundary condition for the actomyosin concentration c is such that the concentration flux across the surface is zero (no-flux condition),

$$j_\perp(z=0) = -M\left.\frac{\partial \mu}{\partial z}\right|_{z=0} = 0 \tag{4.32}$$

where $\mathbf{j} = c(\mathbf{u} + w\mathbf{p}) - M\nabla\mu$ is the concentration current. Note that $u_\perp = 0$ and $p_\perp = 0$ on the surface. A second condition on c is the wetting condition defined such that

$$\left.\frac{\nabla c}{|\nabla c|}\cdot\hat{z}\right|_{z=0} = \cos(180^\circ - \theta) \tag{4.33}$$

where θ is the wetting angle. For simplicity, we assume neutral wetting condition ($\theta = 90^\circ$). A sufficient condition for c to ensure neutral wetting condition on the surface is:

$$\left.\frac{\partial c}{\partial z}\right|_{z=0} = \left.\frac{\partial^2 c}{\partial z^2}\right|_{z=0} = 0 \tag{4.34}$$

Another possible wetting condition is to have a hydrophilic substrate ($\theta > 90^\circ$) though this is beyond the scope of this thesis.

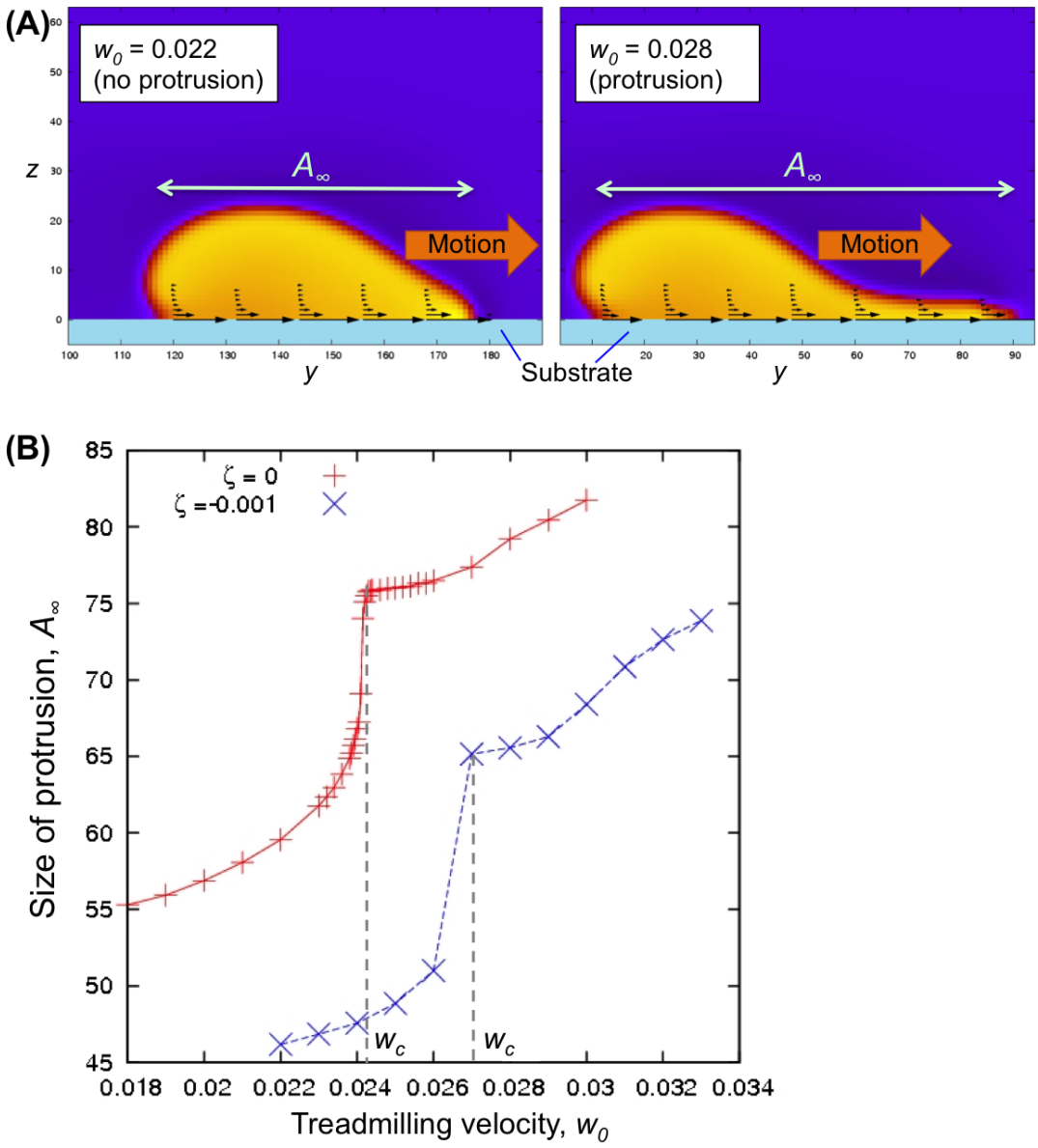

Figure 4.7: **Simulations of cell crawling in 2D. (A)** shows a droplet of actomyosin crawling in the direction of actin treadmilling (black arrows). If the value of actin polymerisation/treadmilling speed w_0 is large enough, we may observe a thin layer of protrusion similar to lamellipodial protrusion (right). Notice that the treadmilling velocity (black arrows) is localised at the surface. (The other parameters are set to be zero $\beta = 0$ and $\zeta = 0$.) **(B)** shows the plot of the protrusion size A_∞ (at steady state) as a function of treadmilling speed w_0. We observe a protrusion transition at critical treadmilling speed w_c. The crosses/blue curve shows the effect of actomyosin contractility on the protrusion transition. (Here we set $\beta = 0$.)

4.4.2 2D simulation of cell crawling

To reproduce lamellipodial protrusion like in real crawling cells, we localise the treadmilling velocity $w\mathbf{p}$ to be close to the substrate (see black arrows in Fig. 4.7(A)):

$$w(z) = w_0 \exp\left(-\frac{z}{z_0}\right) \tag{4.35}$$

In our simulations, z_0 is fixed and we only vary the value of w_0. Note that the substrate is defined on the plane $z = 0$ and the droplet occupies the region $z \geq 0$. Here w_0 roughly corresponds to the velocity of a self-polymerising actin filament in a free solution (which is equal to polymerisation rate $\times$ monomer size, see Sec. 4.2.1). The velocity of an actin filament confined to a cell membrane (and thus the velocity of the crawling cell itself) will be less than w_0. Here we hypothesize that actin polymerisation/treadmilling is localised only near the surface. One possibility why this might be the case is due to the biochemical feedbacks from the focal adhesions [81]. Since focal adhesions are mostly formed at the cell-surface contact, biochemical signalling from these focal adhesions might in turn increase the polymerisation activity of the actin filaments near the surface. Likewise, to produce a finger-like protrusion/filopodial protrusion in cell grabbing (see Fig. 4.3), we might need to localise actin treadmilling to a particular spot on the cell surface. However the nature of the localisation in filopodial protrusion is a little bit different. Here the actin filaments are bundled tightly together giving rise to a high degree of local polarisation ($|\mathbf{p}| \simeq 1$).

In our 2D simulations, the substrate is defined on the line $z = 0$ (see Fig. 4.7). We initialize a half-circular droplet on the upper plane $z \geq 0$ with the polarisation field $\mathbf{p}$ initally pointing uniformly in the y-direction. We set the coupling parameter β to be zero indicating that there is no anchoring of $\mathbf{p}$ to the droplet interface. The role of soft anchoring between $\mathbf{p}$ and the droplet interface will only become relevant in the 3D case which will be discussed in the next section. We then set a positive value of w_0 at $t = 0$ which causes the droplet to move/crawl in the direction of the macroscopic polarisation $\mathbf{p}$ (or the y-direction, see Fig. 4.7(A)). Interestingly if w_0 is large enough, we also observe a thin layer of protrusion which extends from the front of the crawling droplet (see Fig. 4.7(A) right). This is similar to lamellipodial protrusion in real biological cells and the characteristic thickness of the protrusion, in this case, is given by z_0.

We can now plot the protrusion size A_∞ as a function of polymerisation rate/treadmilling speed w_0 (this is shown by the red curve in Fig. 4.7(B)). Here A_∞ is defined as the length of the droplet measured from the rear to the protruding front (see Fig. 4.7(A)) and A_∞ is measured only after the droplet reaches a steadily moving state. The plot of A_∞ against the polymerisation rate w_0 suggests a crossover behaviour/protrusion transition at $w_0 = w_c$ (see Fig. 4.7(B)). Below this critical polymerisation rate $w_0 < w_c$, the droplet is still crawling in the direction of macroscopic polarisation $\mathbf{p}$ but without any significant protrusion (the droplet front is more rounded, see Fig. 4.7(A) left). However when the polymerisation rate is higher than the critical value $w_0 > w_c$, we observe a significant lamellipodial-like protrusion (see Fig. 4.7(A) right).

Effect of contractility

We now look at the effect of actomyosin contraction on lamellipodial protrusion. In general for 2D cases, the shape of the protrusion is not much affected by the addition of actomyosin contraction, on top of actin treadmilling. This suggests that actomyosin contraction is not required to pull the cell body towards to protruding front. Apparently, surface tension alone is enough to maintain the shape of a crawling cell. The only difference is the critical value w_c which becomes higher in the presence of actomyosin contraction (see the blue curve in Fig. 4.7(B)). This means to produce the same observable protrusion, we need to supply a higher rate of actin polymerisation. In the case of 3D droplets, addressed in detail below, the addition of actomyosin contraction can also, in some cases, produce an oscillatory state in which the droplet shape changes periodically without reaching a steady state.

Effect of wall slip

As already mentioned above, focal adhesions play an important role in cell crawling. The lack of focal adhesions can cause the actin filaments to slip backwards as they polymerise against the cell membrane and consequently, actin treadmilling becomes less effective. To emulate the presence or lack of these focal adhesions we introduce a mixture of non-slip and full slip boundary condition at the surface (see previous subsection for more detail). We define a slip parameter

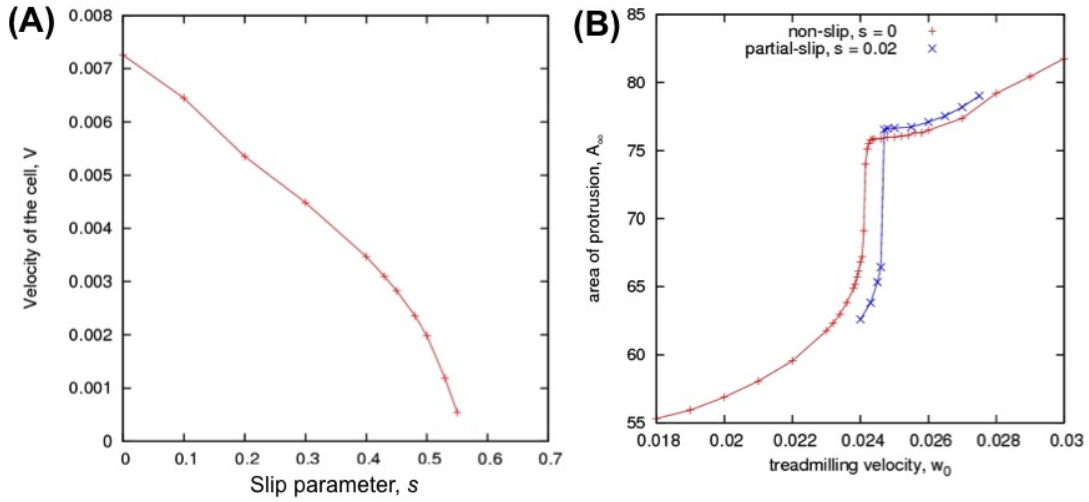

Figure 4.8: **The effect of wall slip on cell crawling.** **(A)** For the same 2D simulations of a crawling cell in Fig. 4.7, we now add partial slip boundary condition to the surface. The slip parameter s is defined such that $s = 0$ corresponds to non-slip and $s = 1$ corresponds to full slip boundary condition. (Alternatively, we can also think $1/s$ as the amount of focal adhesions that the cell makes with the surface - if we have less focal adhesions, the filaments are more likely to slip.) Here we plot the cell's velocity V as a function of the slip parameter s. **(B)** shows the plot of the protrusion size A_∞ as a function of the treadmilling velocity w_0 for non-slip limit ($s = 0$, red curve) and partial-slip ($s = 0.02$, blue curve).

s such that $s = 0$ corresponds to non-slip condition and $s = 1$ corresponds to full-slip condition. Correspondingly, we can also think $1/s$ as the amount of focal adhesions that the cell makes with the surface - if we have less focal adhesions, the filaments are more likely to slip.

Since the slip velocity at the surface will be in the opposite direction to that of actin polymerisation, the cell crawling speed will generally decrease with increasing amount of slip (see Fig. 4.8(A)). The cell velocity eventually drops to zero at $s \simeq 0.55$. This is again consistent with the idea that actin polymerisation becomes less effective with fewer focal adhesions. Furthermore, we can also look at the effect of partial slip on the protrusion transition. Fig. 4.8(B) shows the plot of the protrusion size as a function of polymerisation rate for both the non-slip case ($s = 0$, red curve) and partial-slip case ($s = 0.02$, blue curve). As we can see from the figure, a small amount of slip ($s = 0.02$) shifts the critical polymerisation rate w_c to the right. This means we need a higher value of w_0 to produce the same observable protrusion. For larger amount of slip ($s \gtrsim 0.05$ for the given surface tension in Table 4.1), however, the protrusion is no longer stable and tends to break off from the parent droplet.

4.4.3 3D simulation of cell crawling

Finally we consider a few cases of thin-layer protrusion in 3D active droplets. Fig. 4.9(A) shows one such case. Here the substrate is defined on the x-y plane and non-slip boundary condition is assumed on the substrate. We set the polymerisation rate/treadmilling speed w_0 to be larger than the critical value w_c and thus a thin layer of protrusion is observed along the perimeter of the cell (see figure). However in this picture, we also set the coupling parameter β to be very large and this forces the polarisation field to point perpedicularly outwards at the droplet interface. Consequently the cell will not able to move because the the polarisation field is isotropically distributed (see red arrows in the figure). This is rather similar to the image shown in Fig. 4.1(C) left.

Fig. 4.9(B) shows a similar droplet but now with a lower value of β. In this case the polarisation field is less anchored to the interface and this breaks the isotropy in the orientational configuration. Consequently, the droplet will now be able to move in the direction of the global polarisation (which is the x-direction in the figure). The lamellipodia-like protrusion is still observed since the treadmilling

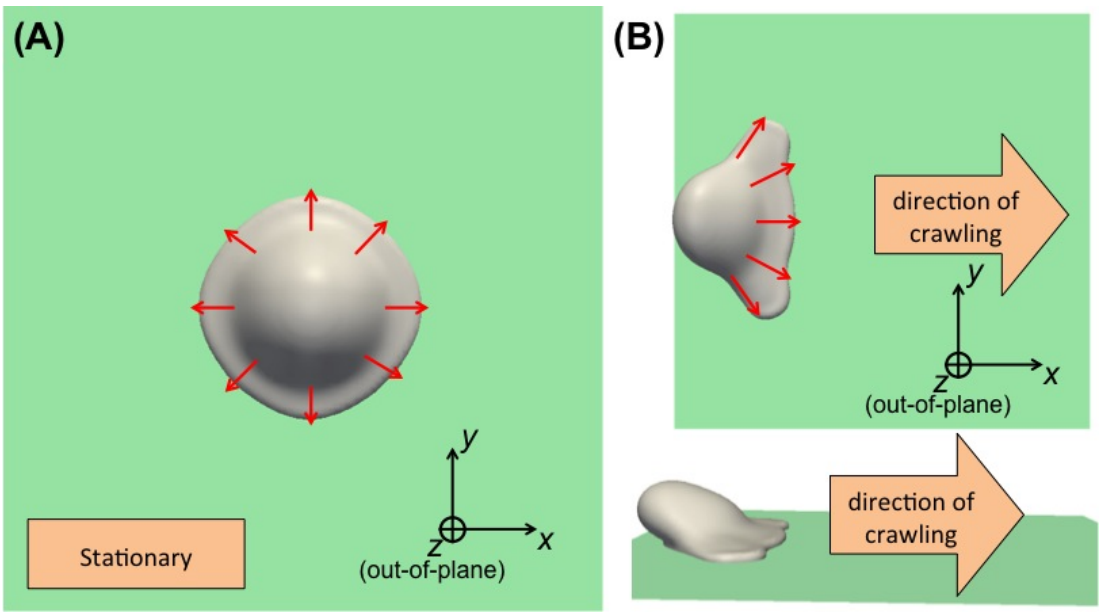

Figure 4.9: **Simulations of cell crawling in 3D. (A)** ($w_0 = 0.035$, $\zeta = -0.001$, and $\beta = 0.02$) Here the treadmilling speed w_0 is larger than the critical value w_c and thus protrusion is observed. However since the polarisation field $\mathbf{p}$ is isotropically distributed (red arrows), the droplet is not moving. Note that the value of the coupling parameter β is large enough to force the polarisation field to point perpendicularly to the droplet interface. **(B)** ($w_0 = 0.04$, $\zeta = -0.001$, and $\beta = 0.001$) Upon decreasing the value of β, the polarisation field is now less anchored to the interface. Therefore, the droplet will now start to move in some random direction (the x-direction in this case). (Images courtesy of A. Tiribocchi.)

speed is still larger than the critical value. In addition, the lamellipodium still maintains a broad and thin structure with the actin polarisation inside splayed in the direction of motion. This splay deformation of the actin polarisation is due to a finite value of β or possibly ζ as we shall see later, actomyosin contraction can also induce splay deformation. This again looks rather similar to the image shown in Fig. 4.1(C) right except that the spontaneous symmetry breaking illustrated in Fig. 4.1(C) is mediated by an external chemical concentration gradient (chemotaxis) rather than a soft anchoring β. (In eukaryotic cells, the value of β is unlikely to vary a lot without changing the interfacial chemistry.) In principle, it is still possible to simulate the effects of chemotaxis by treating the chemical concentration gradient as an 'external field' which couples to the polarisation field in the free energy [82].

As already implied above, the presence of a soft anchoring ($\beta > 0$) will cause the polarisation field $\mathbf{p}$ to be slightly splayed in the direction of motion (in the extreme case such as in Fig. 4.9(A), a large value of β can cause the polarisation field to point radially outwards from the centre of the droplet - thus creating a hedgehog defect at the centre). Furthermore, as we shall see in the next chapter, the presence of a contractile stress ($\zeta < 0$) will also induce a splay deformation in the direction of motion. The splay deformation induced by the soft anchoring term and that by the contractility, however, are not identical to each other (as we can see from Fig. 4.10). Combinations of both β and ζ can therefore give rise to some interesting protrusion morphologies (provided $w_0 > w_c$), as shown in Fig. 4.10. For instance in Fig. 4.10(A), we have $\beta = 0.001$, $\zeta = -0.0015$ and $w_0 = 0.04 > w_c$. The combination of these three parameters gives rise to a rather broad and thin protrusion, similar to a lamellipodial protrusion in real cells. Switching off the contractility (Fig. 4.10(B)), however, the droplet morphology changes significantly. Here, we have two rather pointed protrusions in the direction diagonal to the direction of motion. The shape of the protrusions is somewhat intermediate between a lamellipodium and a filopodium and we may classify such protrusions as pseudopodia [16]. Finally switching off soft anchoring term and restoring the contractility (Fig. 4.10(C)), we have a single pointed protrusion which resembles a pseudopod.

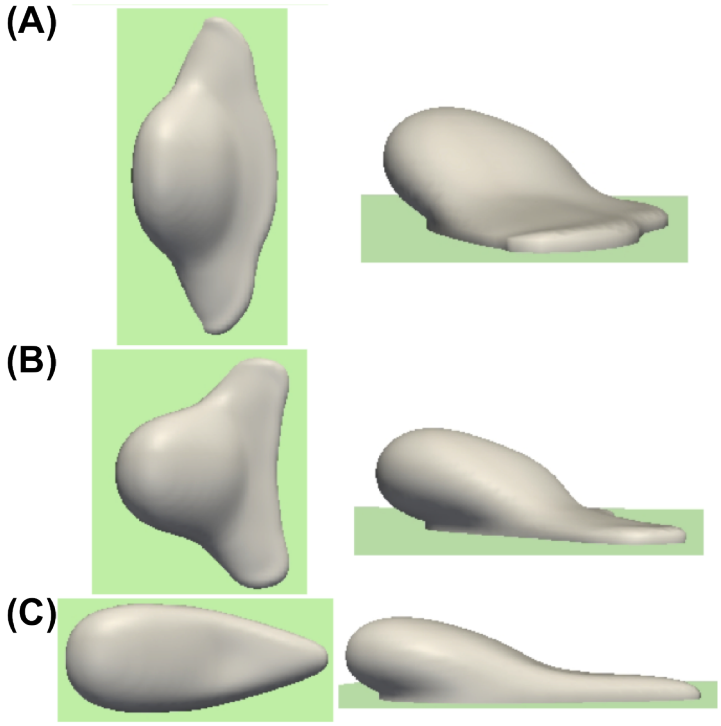

Figure 4.10: **Different morphologies of simulated cell crawling on a 2D substrate.** **(A)** ($w_0 = 0.04$, $\zeta = -0.0015$, and $\beta = 0.001$) In this simulation run, the protrusion is rather broad and thin similar to a lamellipodial protrusion in real cells. Here the presence of contractile activity ($\zeta < 0$) and soft anchoring ($\beta > 0$) may help the polarisation field to splay in the direction of motion thus contribute to the broad protrusion (also similar to the one shown in Fig. 4.9(B)). **(B)** ($w_0 = 0.04$, $\zeta = 0.0$, and $\beta = 0.001$) In this simulation run, we switched off the contractility ($\zeta = 0$) while keeping the other parameters (w_0 and β) unchanged. We now see a significant change in the droplet morphology in which the protrusion is no longer broad. Instead, we now have two rather pointed protrusions in the direction diagonal to the direction of motion. The shape of the protrusion is somewhat intermediate between a lamellipodium and a filopodium, and we may classify such protrusions as pseudopodia [16]. **(C)** ($w_0 = 0.04$, $\zeta = -0.001$, and $\beta = 0$) Finally switching off the soft anchoring term ($\beta = 0$), we now have a single pointed protrusion which may look like a pseudopod. (Images courtesy of A. Tiribocchi.)

4.5 Summary

In conclusion, the mechanism for cell motility is very diverse and can be described in many ways, either microscopically or macroscopically. However the physics of cell motility can be simplified greatly if we only consider a droplet of actomyosin matter (neglecting other molecules such as microtubules and cell nucleus). For example, many phenomena associated with cell motility such as lamellipodial and filopodial protrusion can be explained in terms of just two active processes inside the actomyosin solution, namely, actin polymerisation and actin-myosin contraction.

In this chapter we established a simple hydrodynamic model for such actomyosin droplet. In particular the two active processes inside the actomyosin network, actin polymerisation and actin-myosin contraction, can be easily coarse-grained to first order as a swimming term and a contractile stress respectively. Furthermore, the actin filaments are also ordered giving rise to a macroscopic polarisation. This makes the hydrodynamic description of actomyosin solution very similar to that of bacterial suspensions in the previous chapter. As we have seen above, our hydrodynamic model is indeed consistent with the microscopic model. In particular we find that the cell's velocity typically goes down with decreasing focal adhesions, consistent to Brownian ratchet picture.

In addition, our hydrodynamic model can have some advantages over the microscopic model. In particular, our hydrodynamic model allows us to study the cell dynamics over much larger lengthscales - not just a single actin filament. Using this simple model of an active droplet, we show numerically that a crawling droplet - driven by actin polymerisation - can produce a thin layer of protrusion at large enough polymerisation rate, so long as the polymerisation activity is confined to a thin layer near the surface. We also speculate that the reason for this localised polymerization activity might come from biochemical signalling from focal adhesions at cell-surface contact. The appearance of this protrusion can be characterised as a non-equilibrium phase transition which occurs at some critical polymerisation rate. Further simulations in 3D also show that this protrusion can look qualitatively similar to lamellipodial protrusion as observed in real biological cells.

Chapter 5

Spontaneous symmetry breaking as a new route to cellular motility

Tumour cells employ various different strategies to move inside a 3D environment such as tissues *in vivo* or polymeric gels *in vitro* [16]. The most common mechanism for these cells to move in such crowded environments is by forming a finger-like protrusion (called filopodial protrusion) [13]. These filopodia are then used by the cell to 'grab' (by forming focal adhesions) and pull the polymers in the gel - causing the cell to move in the direction of the protrusion. The mechanism for this filopodial protrusion is similar to that of lamellipodial protrusion in cell crawling which involves actin polymerisation/treadmilling and focal adhesion (see previous chapter). In the case of filopodial protrusion, the actin filaments are bundled tightly together giving rise to a large localised actin polarisation. Actin polymerisation at the plus end of the bundle then pushes the cell membrane forward, creating a finger-like protrusion in the direction of actin polarisation. However as we have also seen from the previous chapter, in order to see a significant protrusion, the polymerisation rate of these actin filaments has to be large enough (above some critical value).

Recently however, Poincloux *et al.* [12] discovered that some tumour cells can also move inside a 3D polymeric gel without forming any visible protrusion. We call this new type of tumour cell migration 'swimming'. The lack of any visible protrusion indicates that the role of actin polymerisation (and focal adhesion) may be less involved in the process of cell swimming. In fact it has first been shown by Hawkins *et al.* [17] that actomyosin contraction alone, without any actin

polymerisation, can also generate cellular motion inside a 3D viscous environment. This is due to the presence of actin flows along the cortex/perimeter of the cell which propels the cell forward. And as we will show in this chapter, the presence of this actin flow is mediated by splay instability which also spontaneously breaks a global symmetry.

From the previous chapter, we learnt that the process of actomyosin contraction can also be coarse-grained into an active stress term, characterised by an activity parameter ζ. For actomyosin systems, ζ is negative to indicate a contractile stress (whereas for bacterial suspensions ζ is positive to indicate an extensile stress). The magnitude of ζ is proportional to the pulling force from the motor proteins (myosins). As before, we again consider a droplet of actomyosin as a simple representation of a eukaryotic cell (or more realistically a cell extract as shown in Fig. 1.3(B) of the introduction). Whereas in the previous chapter, we focus mainly on the effects of actin treadmilling, here in this chapter, we shall focus more on the effects of active stresses on the dynamics of polar active droplets. For instance, we consider a purely contractile droplet as a model for cell swimming. Effectively, this is just a droplet of force dipoles which do not swim (or shakers). However as we shall see below, even the presence of a contractile stress alone (without any actin treadmilling) can also create a unidirectional motion. At first, this may sound impossible since a shaker particle, even if it is polar, is not going to move anywhere on its own. It turns out that the spontaneous motion in a droplet of shaker particles is characterised by a *global* spontaneous symmetry breaking (SSB) rather than a *local* one. Finally, we shall also study a droplet of extensile fluid with and without treadmilling/swimming. This may be relevant, for instance, to droplets of bacterial suspensions or microtubule-kinesin systems [83, 84].

5.1 Symmetries and equations of motion

Here we study numerically the effects of active stresses in a droplet of actomyosin/bacterial suspension. Our simulation model comprises a droplet of an active fluid, confined by interfacial tension $\widetilde{\gamma}$, and surrounded by a Newtonian host fluid. The hydrodynamic equations have been derived phenomenologically in the previous chapter and here we will just summarise the main results. The

hydrodynamic variables that we are solving are: (i) concentration of active matter $c(\mathbf{r},t)$, (ii) polarisation field to indicate local average orientation $\mathbf{p}(\mathbf{r},t)$ and (iii) fluid velocity of the solvent $\mathbf{u}(\mathbf{r},t)$. An active droplet is defined such that the concentration of the active material is finite inside the droplet ($c>0$) and zero outside ($c=0$). Furthermore, we also assume the active fluid inside the droplet to be polar so that that the polarisation field is finite inside the droplet ($|\mathbf{p}|>0$) and zero/isotropic outside ($|\mathbf{p}|=0$).

We start from a free energy functional which has the following form:

$$\begin{aligned} F[c,\mathbf{p}] &= \int d^3r \left\{ \frac{a}{4c_r^2}c^2(c-c_0)^2 + \frac{k}{2}\left|\nabla c\right|^2 \right. \\ &\left. -\frac{\alpha}{2}\frac{(c-c_r)}{c_r}\left|\mathbf{p}\right|^2 + \frac{\alpha}{4}\left|\mathbf{p}\right|^2 + \frac{\kappa}{2}(\nabla\mathbf{p})^2 + \beta\mathbf{p}\cdot\nabla c \right\} \end{aligned} \tag{5.1}$$

The time evolutions for $c(\mathbf{r},t)$, $\mathbf{p}(\mathbf{r},t)$ and $\mathbf{u}(\mathbf{r},t)$ are

$$\frac{\partial c}{\partial t} + \nabla\cdot\left[c(\mathbf{u}+w\mathbf{p})\right] = M\nabla^2\frac{\delta F}{\delta c} \tag{5.2}$$

$$\frac{\partial \mathbf{p}}{\partial t} + (\mathbf{u}+w\mathbf{p})\cdot\nabla\mathbf{p} = -\underline{\underline{\Omega}}\cdot\mathbf{p} + \xi\underline{\underline{v}}\cdot\mathbf{p} - \frac{1}{\Gamma}\frac{\delta F}{\delta\mathbf{p}} \tag{5.3}$$

$$\nabla\cdot\mathbf{u} = 0 \tag{5.4}$$

$$\rho\left(\frac{\partial}{\partial t} + \mathbf{u}\cdot\nabla\right)\mathbf{u} = -\nabla P + \eta\nabla^2\mathbf{u} + \nabla\cdot\left(\underline{\underline{\sigma}}^p - \zeta c\mathbf{pp}\right) \tag{5.5}$$

(See previous chapter for parameter definitions.) Note that we assume the viscosity of the active fluid (inside the droplet) to be the same as that of passive fluid (outside the droplet). The three important ingredients in our hydrodynamic model of active droplets are

(i) self-advection/treadmilling (which is a non-equilibrium term), characterised by the parameter $w>0$,

(ii) active stress term (also non-equilibrium), characterised by the the parameter ζ which can be negative (contractile) or positive (extensile) and finally

(iii) soft anchoring of $\mathbf{p}$ to the droplet interface (which is an equilibrium term), characterised by the parameter β which can be negative (pointing inwards) or positive (pointing outwards).

In the case of $w = 0$ and $\zeta = 0$ we recover the equilibrium limit which is just a passive droplet of polar liquid crystals.

We initialized our simulation runs with a circular (or spherical) droplet within which the concentration of active material is taken to be a constant. The polarization field $\mathbf{p}$ within the droplet is initially uniform along the horizontal x-axis while $\mathbf{p}$ outside is zero/isotropic. (Note that initially our system is already in a broken symmetry state, *i.e.* locally polarised.) We also assume periodic boundary condition on each side of the simulation box unless stated otherwise. We shall study the effects of active stresses systematically by first switching off the treadmilling term ($w = 0$) and the coupling term ($\beta = 0$) and therefore we only vary ζ at the moment. When we set these to be zero ($w = \beta = 0$), the equations of motion (5.2-5.5) now become invariant under a *global* inversion symmetry:

$$\mathbf{p}(\mathbf{r}) \to -\mathbf{p}(\mathbf{r}) \quad \text{, for all } \mathbf{r} \tag{5.6}$$

and therefore in order for the droplet to move, it must at least break this global symmetry. Note that this symmetry is different from a *local* inversion symmetry such as when we flip the polarities of all the particles inside a small volume element $dV(\mathbf{r})$:

$$\hat{\nu}_i \to -\hat{\nu}_i \quad \text{, for all } i \text{ inside } dV(\mathbf{r}) \tag{5.7}$$

where $\hat{\nu}_i$ is the polarity of the ith particle. This is the exact definition of nematic order as discussed in chapter 3. In our case, the system is polar ordered (since we are using $\mathbf{p}$ rather than $\underline{\underline{Q}}$) and thus it does not satisfy the local inversion symmetry (5.7). Half-integer defects in our system, for instance, are not allowed since they require the system to be locally nematic. Nevertheless far from defect points, the dynamics of $\mathbf{p}$ should be similar to that of the director field $\hat{\mathbf{n}}$, where $\hat{\mathbf{n}}$ is the largest eigenvector of $\underline{\underline{Q}}$ (see Leslie-Ericksen nematodynamics [35]). On a related subject, droplet motion which is driven by actin treadmilling/bacterial swimming ($w > 0$) requires the system to break the local inversion symmetry (*i.e.* nematic-to-polar transition, see chapter 3 section 3.1.2).

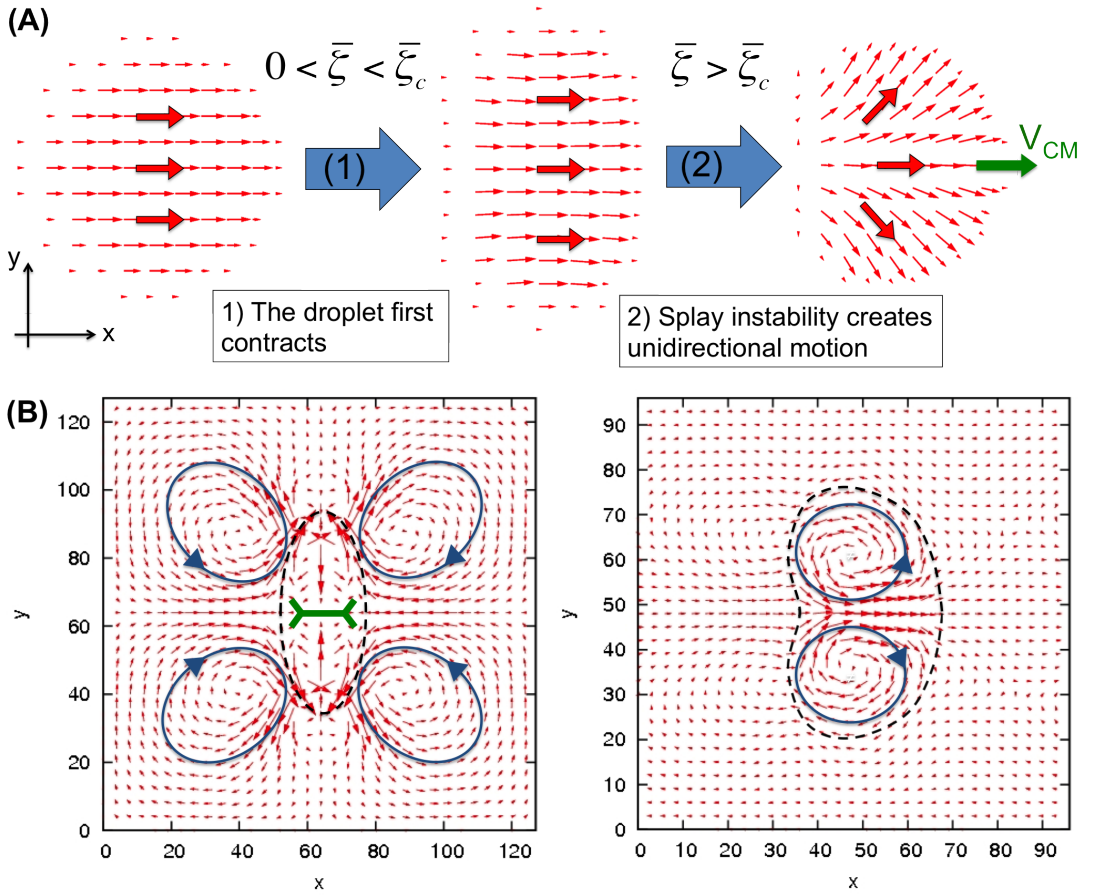

Figure 5.1: **(A)** Steady state configurations of a purely contractile active droplet (without treadmilling and coupling terms). The (red) arrows show the steady state polarization field $\mathbf{p}(\mathbf{r})$. Upon increasing the contractile activity $\bar{\zeta} = -\zeta > 0$, the droplet elongates in the direction perpendicular to $\mathbf{p}$ and then becomes unstable with respect to splay deformation at critical activity $\bar{\zeta}_c$. When it splays, the droplet also spontaneously moves in the direction of the green arrow. **(B)** Left plot shows the steady state velocity field of the droplet at $\bar{\zeta} < \bar{\zeta}_c$ which is quadrupolar, like that around a contractile element (Fig. 1.4 of the introduction). Right plot shows the velocity field of the splayed and moving active droplet which consists of two opposing vortices. The boundary of the droplet itself is given by the dashed line.

5.2 Actomyosin contraction alone can induce motility *via* SSB

In this section we shall consider a droplet of contractile fluid surrounded by a passive viscous fluid as a simple model of a eukaryotic cell inside a tissue/polymeric gel. Although contractile motor stress and actin treadmilling are generally both present in motile cells, it is illuminating to study these two mechanisms separately. We first consider a droplet without treadmilling and coupling term ($w = \beta = 0$) and therefore the system is invariant under the global inversion in Eqn. (5.6). The only parameter we vary at the moment is the activity parameter ζ which is negative for contractile fluid. For convenience we shall define $\overline{\zeta} = -\zeta > 0$.

For low activity $\overline{\zeta}$, below some critical value $\overline{\zeta}_c$, the droplet polarisation field $\mathbf{p}$ remains aligned uniformly along its initial direction $\hat{x}$ and the droplet remains stationary. However the droplet now becomes slightly elongated in the direction perpendicular to the polarisation vector $\mathbf{p}$ as a result of the competition between the contractile stress and the interfacial tension (see Fig. 5.1(A) middle). In this regime, the contractile stress set up a quadrupolar fluid flow around the droplet externally (Fig. 5.1(B) left), so that the whole droplet behaves like a giant contractile shaker (*cf.* Fig. 1.4 in the introduction).

As we increase $\overline{\zeta}$ beyond $\overline{\zeta}_c$, the uniform polarization field $\mathbf{p}$ becomes unstable with respect to a splay deformation (see Ramaswamy [85]). This happens because the contractile stress is large enough to overcome the elastic deformation in the liquid crystalline phase. The splay also creates a state in which the polarisation field $\mathbf{p}$ either fan outwards ($\nabla \cdot \mathbf{p} > 0$) or inwards ($\nabla \cdot \mathbf{p} < 0$). The first is shown in Fig. 5.1(A) right and the second is shown in Fig. 5.2 bottom right. This choice is made at random, spontaneously breaking the global inversion symmetry. As soon as this happens, the droplet starts to move in the direction of splay $(\nabla \cdot \mathbf{p})\mathbf{p}$. This motion is attributed to the formation of a pair of fluid vortices inside the droplet (Fig. 5.1(B) right). Furthermore, if we only look at the flow along the perimeter of the droplet, the fluid flows almost tangentially from the front to the back (see Fig. 5.3), consistent to the cortical actin flow predicted by Hawkins *et al.* [17]. Also note that in order for the droplet to move to the right the droplet has to push the same amount of fluid outside to the left (see Fig. 5.3) so that the

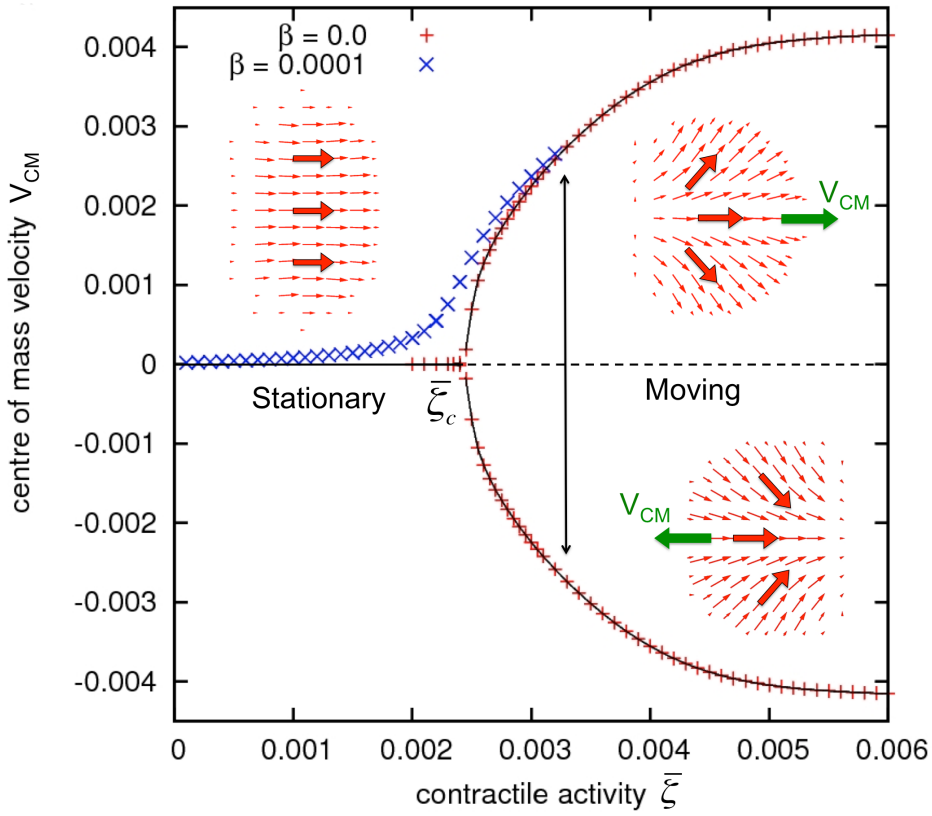

Figure 5.2: Bifurcation diagram showing spontaneous symmetry breaking from a uniform and stationary state to a splayed and moving state as the contractile activity parameter $\bar{\zeta}$ is increased (red curve). The blue curve shows the effect of a soft anchoring of the polarisation field $\mathbf{p}$ to the droplet interface ($\beta = 0.0001$, see text). The presence of a soft anchoring has a similar effect to a weak external field in para-/ferromagnetic transition which destroys the second order transition at the critical point.

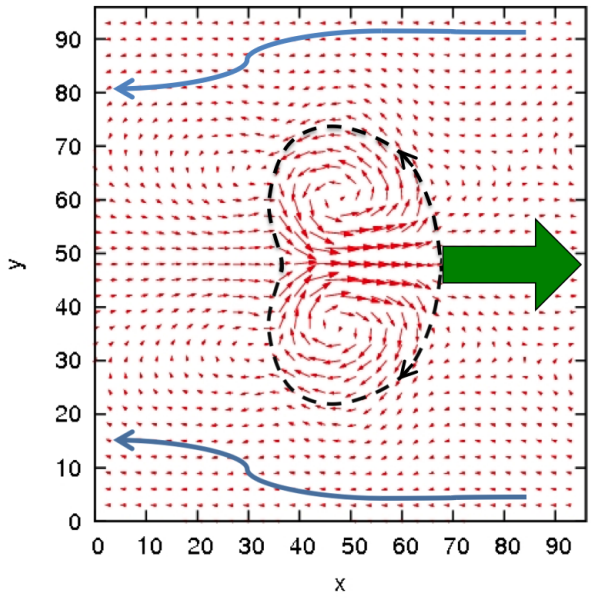

Figure 5.3: In order for the droplet to move to the right, it has to push the fluid solvent outside to the left so that the total momentum (of the droplet and the fluid outside) remains zero. Also notice the tangential fluid flow along the perimeter of the droplet, consistent with that predicted in Hawkins *et al.* [17]

total momentum (of the droplet and the fluid outside) remains zero. This is as expected, since our droplet only consists of force dipoles which should not add any translational/angular momementum to the system. There is also another similar mechanism for self-propulsion in droplets of bromine water. Here, a chemical reaction (Belousov-Zhabotinsky reaction) inside the droplet creates a Marangoni flow along the perimeter of the droplet which, in turn, propels the droplet (see Refs. [86, 87]).

Note that in bulk active contractile fluids, the state of uniform $\mathbf{p}$ is also generically unstable to splay fluctuations in 1D [88, 60], which then lead to the onset of spontaneous flow. At one level, the SSB-induced motility transition described here can be viewed as a manifestation of that bulk instability in a confined geometry (see Fig. 3.6 of chapter 3), albeit with two slight variations. First, spontaneous flows are present on both sides of our transition: as discussed above there is a quadrupolar flow field already in the non-moving state. Second, in bulk the value of the critical activity is nonzero only in finite systems, for which the transition is discontinuous, unlike ours (see below and Fig. 5.2).

To illustrate our symmetry breaking motility mechanism more clearly, we plot the magnitude of the centre of mass velocity of the droplet V_{CM} as a function of activity $\overline{\zeta}$ in Fig. 5.2. This bifurcation diagram shows a continuous non-equilibrium transition from a stationary and uniform state to a moving and splayed state. Moreover, to within numerical accuracy the observations are consistent with a supercritical Hopf bifurcation, for which $V_{CM} \sim (\overline{\zeta} - \overline{\zeta}_c)^{0.5}$. This mean-field like exponent is as expected since there is no noise in our simulations. Accordingly it might change in the presence of activity-generated noise. For example in Berthier and Kurchan [89], one can also have a non-thermal coloured noise which does not satisfy the fluctuation-dissipation theorem.

Finally, we also simulate a few cases of a 3D contractile droplet surrounded by a passive viscous fluid as a more realistic model of cell swimming inside 3D tissues/polymeric gels. Fig. 5.4 shows steady state polarization fields inside a 3D contractile droplet with increasing values of the contractile activity $\overline{\zeta}$ from (A) to (D). As expected, the first steady state encountered is a slightly elongated immotile droplet (Fig. 5.4(A)). The active stress contracts the droplet along $\mathbf{p}$ resulting in a lenticular shape - similar to the 2D picture in Fig. 5.1(A) middle but rotated along the axis of cylindrical symmetry. As we increase $\overline{\zeta}$ beyond a critical $\overline{\zeta}_c$, splay instability spontaneously breaks the global inversion symmetry and causes the droplet to move along $(\nabla \cdot \mathbf{p})\mathbf{p}$. The droplet shape for the motile case is slightly concave as can be seen from the figure, much like a rotated version of the 2D picture in Fig. 5.1(A) right. The internal fluid flow of the 3D motile droplet now resembles a toroidal vortex ring (Fig. 5.4(E)), which can be obtained from rotating the two fluid vortices in the 2D case around the axis of cylindrical symmetry. Interestingly, as $\overline{\zeta}$ is increased further, the droplet becomes increasingly spherical (Fig. 5.4(C)), and finally symmetry is restored, creating an immotile spherical droplet with a 'hedgehog' defect of topological charge 1 (Fig. 5.4(D)).

Thus, we have showed that actomyosin contraction alone can provide an alternative route to cellular locomotion both in 2D and 3D. It is not known experimentally, however, whether cell swimming in a 3D viscous environment is driven solely by actomyosin contraction. One way to verify this experimentally, is to inject the swimming cell with some fluorescent tracer particles and study the internal fluid flow, whether it resembles to the toroidal flow shown in Fig. 5.4(E).

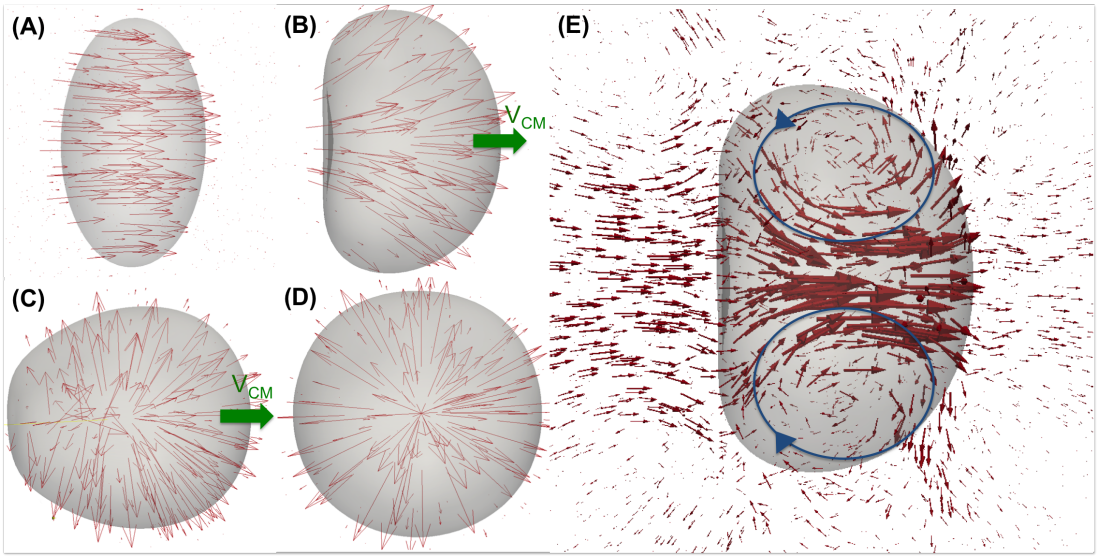

Figure 5.4: Steady state conformations in 3D contractile droplets without self-advection on increasing activity $\overline{\zeta}$ from **(A)** to **(D)**. (B) and (C) are motile with the direction of motion indicated by the green arrows while (A) and (D) are stationary. (E) shows the toroidal fluid flow inside the motile droplet of steady state (B). (Note that the red arrows in **(A)**-**(D)** indicate the polarisation whereas the red arrows in **(E)** indicate the fluid velocity.)

5.2.1 Effect of a soft anchoring at the interface

The coupling term in the free energy equation (5.1), $\sim \beta \mathbf{p} \cdot \nabla c$, represents a soft anchoring of $\mathbf{p}$ to the droplet interface (so that $\mathbf{p}$ will tend to point outwards at the droplet perimeter for $\beta > 0$). Alternatively we can relate the parameter β to a dimensionless ratio $H = \frac{\gamma_1 - \gamma_2}{\gamma_1 + \gamma_2}$ where $\gamma_{1,2}$ are the interfacial tensions with polarity directed along the outward or inward normal. The interfacial tension for this purpose is calculated numerically by computing the excess free energy across the interface - since the analytic expression for the surface tension cannot be found. Here we shall study the effect of a soft anchoring β on the SSB-induced droplet motion, discussed above.

A nonzero value of H (and hence of β) is allowed by symmetry and indeed in a passive system of simple amphiphilic molecules one would expect H value of order unity. For an actomyosin droplet (such as lamellipodia), we expect H (and thus β) to be positive since the plus ends of the actin filaments are in general pointed outwards (see previous chapter). The magnitude of H for actomyosin droplet, however, is expected to be much smaller than that of amphiphiles since

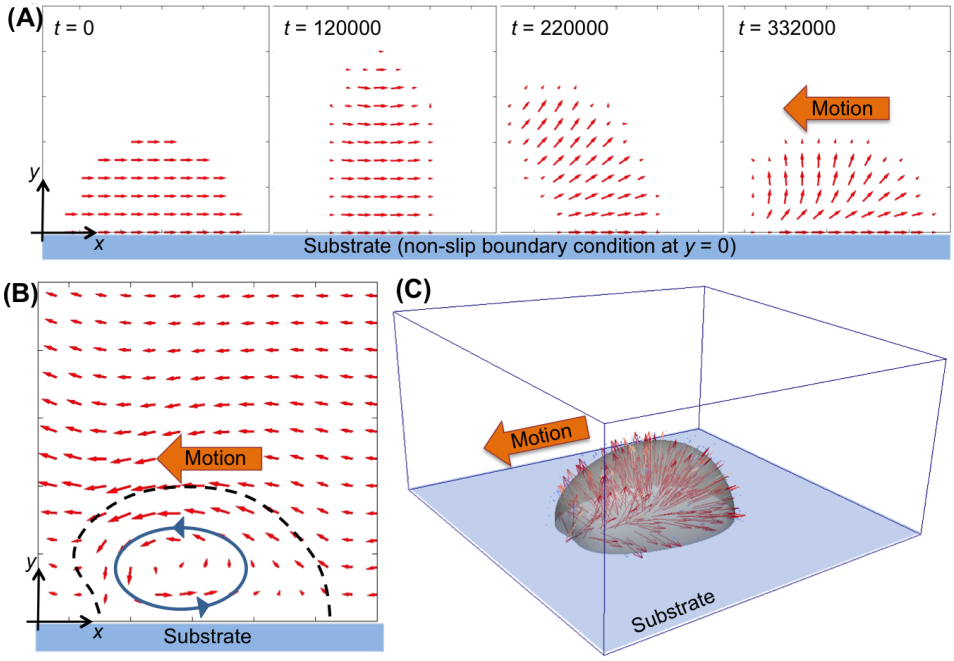

Figure 5.5: **(A)** A purely contractile droplet on a non-slip surface can still spontaneously move. However unlike contractile droplets in bulk fluid, the direction of motion is now opposite to the direction of splay $(\nabla \cdot \mathbf{p})\mathbf{p}$. (The red arrows indicate the polarisation field.) **(B)** shows the fluid velocity inside the droplet which consists of a single fluid vortex (note that the arrows here indicate the velocity field). **(C)** shows the 3D equivalent of a contractile droplet on a non-slip surface (with the red arrows indicate the polarisation field).

there is no obvious chemical mechanism which strongly binds the actin filaments to the lipid bilayer of the cell membrane. In Fig. 5.2 we show the effect of adding a small β term on the SSB transition that leads to motility in the absence of self-advection ($w = 0$). Here, we choose $\beta = 0.0001$ which roughly corresponds to $H = 10^{-4}$. The effect resembles that of applying a weak external field to a ferromagnet undergoing an Ising-type phase transition. Instead of a critical bifurcation, we now have a smooth continuous line on the upper region of the plot V_{CM} versus $\bar{\zeta}$ (see the blue curve in Fig. 5.2). This is because a positive value of β induces a splay deformation in the direction of $\mathbf{p}$, in order to minimize the interfacial energy. And therefore, a small amount of contractility already creates a pair of internal fluid vortices which causes the droplet to move in the direction of splay, *i.e.* $\mathbf{p}$.

5.2.2 Purely contractile droplet on a non-slip surface

We now consider what happens if we place a purely contractile droplet on a non-slip substrate. The contractile stress alone can still induce droplet motion without any actin treadmilling (as shown in Fig. 5.5(A)). The process is still the same as above with the droplet initially elongates in the direction perpendicular to $\mathbf{p}$ and then spontaneously breaks the global inversion symmetry by inducing a splay deformation. And as the polarisation field splays, the droplet also starts to move due to the the formation of an internal fluid flow. However unlike contractile droplets in bulk fluid, the direction of motion is now opposite to that of splay $(\nabla \cdot \mathbf{p})\mathbf{p}$. This is because there is now only one fluid vortex inside the droplet (see Fig. 5.5) instead of two. Accordingly, we may treat a contractile droplet on a surface as a half droplet of that in bulk fluid (compare the polarisation field in Fig. 5.5 to that in the upper half droplet of Fig. 5.4(C)). In the case of full-slip boundary condition, the internal fluid flow inside the droplet on the surface looks exactly the same as that of the half-droplet in bulk fluid. Correspondingly for full-slip boundary condition, the droplet will move in the same direction of splay like that in bulk fluid. However in our case, the fluid velocity of the droplet vanishes at the substrate (non-slip boundary condition). This has the same effect of going into a frame of reference in which the fluid velocity at the centre of the droplet vanishes. Since the magnitude of the fluid velocity at the centre of the droplet in the bulk is typically about twice as large as that of the droplet velocity itself, going into this new frame of reference reverses the direction of motion and therefore the droplet on the surface will move in the direction opposite to that of splay. Obviously, the SSB-induced droplet motion here does not produce any protrusion unlike a droplet motion driven mostly by actin treadmilling.

5.2.3 Cell crawling revisited

Recall that cell crawling on a solid surface is characterized by a lamellipodial protrusion, which is effectively a 2D sheet of actomyosin matter. Therefore our strict-2D simulations of contractile droplet in Fig. 5.1 may also be applicable to a lamellipodium extract crawling on a hard surface (viewed from above). (Recall that a lamellipodium extract can still move on its own independently of its parent cell [33].) To approximate the lamellipodium-surface interaction in

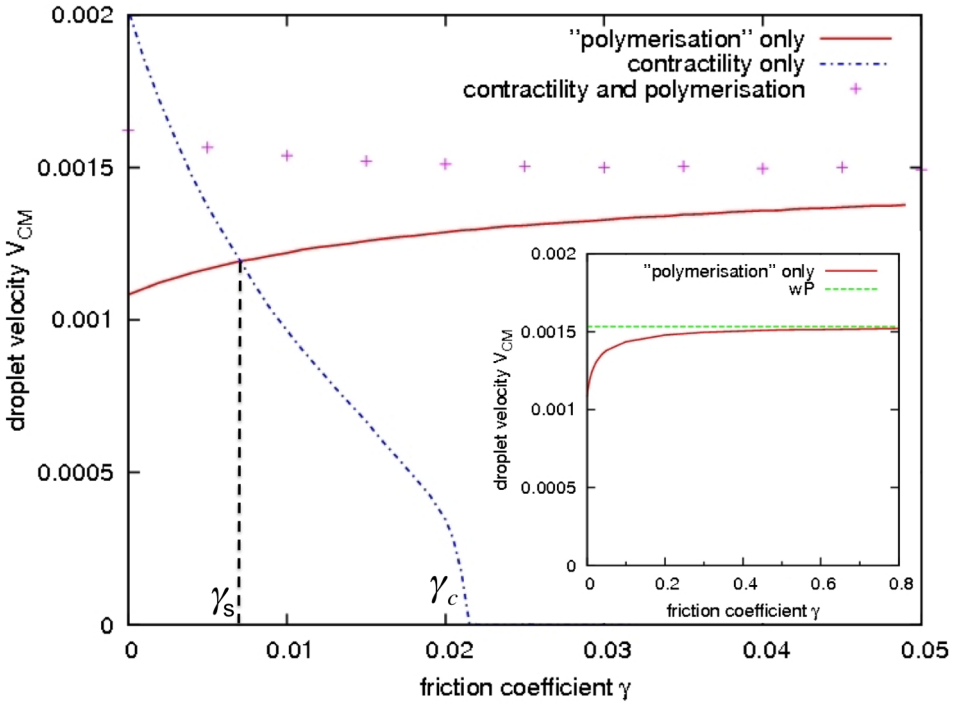

Figure 5.6: Plots of droplet velocity V_{CM} against frictional coefficient γ for motile droplets driven by: contractile stress only ($\overline{\zeta} = 0.0028$ and $w = 0$, dot-dashed blue line) and polymerization/self-advection only ($\overline{\zeta} = 0$ and $w = 0.0015$, solid red line) and both ($\overline{\zeta} = 0.0028$ and $w = 0.0015$, plus points). The inset shows the polymerization-only driven motility in the limit of large friction in which the droplet velocity approaches some steady state value (indicated by the dashed green line in the inset).

strict-2D geometry such as in Fig. 5.1, we introduce an additional friction force density to the momentum balance equation (5.5):

$$\rho\left(\frac{\partial}{\partial t}+\mathbf{u}\cdot\nabla\right)\mathbf{u}=-\nabla P+\eta\nabla^2\mathbf{u}+\nabla\cdot\left(\underline{\underline{\sigma}}^p+\underline{\underline{\sigma}}^a\right)\underbrace{-\gamma\mathbf{u}}_{\text{friction term}} \tag{5.8}$$

where $\gamma > 0$ is the friction coefficient between the substrate and the crawling cell (or roughly, the density of focal adhesions that the lamellipodium forms with the surface). Note in the previous chapter, we approximate the focal adhesions between the cell and the surface by the slip parameter s. This is because in the simulations of chapter 4, the lamellipodium has a finite thickness, characterised by the lengthscale z_0. In Fig. 5.1 however, we are simulating a strictly-2D contractile droplet which does not have any thickness and thus a partial slip boundary condition cannot be implemented.

Fig. 5.6 shows the droplet velocity as a function of friction coefficient γ. The blue dot-dashed line represents a motile droplet driven by contractility only ($\bar{\zeta} = 0.0028$). In this case the direction of motion is in the same direction of splay $(\nabla\cdot\mathbf{p})\mathbf{p}$. As can be seen from the plot, the presence of friction typically reduces the contractility-induced motility so that the droplet velocity eventually drops to zero at large enough friction γ_c. The red solid line in Fig. 5.6, on the other hand, represents a motile droplet driven solely by treadmilling ($w = 0.0012$). The direction of motion, in this case, points in the same direction of actin polarisation $\mathbf{p}$. Here the presence of friction will instead enhance the treadmilling-induced motility with the droplet velocity eventually reaches a steady state value as $\gamma \to \infty$ (see inset)[1]. The intersection of the two plots (found respectively by switching off activity or self-advection) defines a characteristic friction scale γ_s (see figure). For $\gamma < \gamma_s$ contractile stress dominates cell motility, while for $\gamma > \gamma_s$ self-advection is more dominant. In cell crawling, the actin polarisation inside the lamellipodium is also splayed in the same direction of polarisation (See Fig. 4.1 in chapter 4). And therefore, the contractility-induced and treadmilling-induced motility should be complementary to each other. In fact the plus points in Fig. 5.6 shows the droplet velocity driven by both contractility and treadmilling ($\bar{\zeta} = 0.0028$ and $w = 0.0012$) which is typically larger than droplet motion

[1]Conversely when the friction coefficient is reduced, the treadmilling-induced velocity goes down to a finite value at zero friction limit ($\gamma \to 0$). The treadmilling velocity does not go to zero at zero friction because there is still some fluid viscosity which can act as a friction.

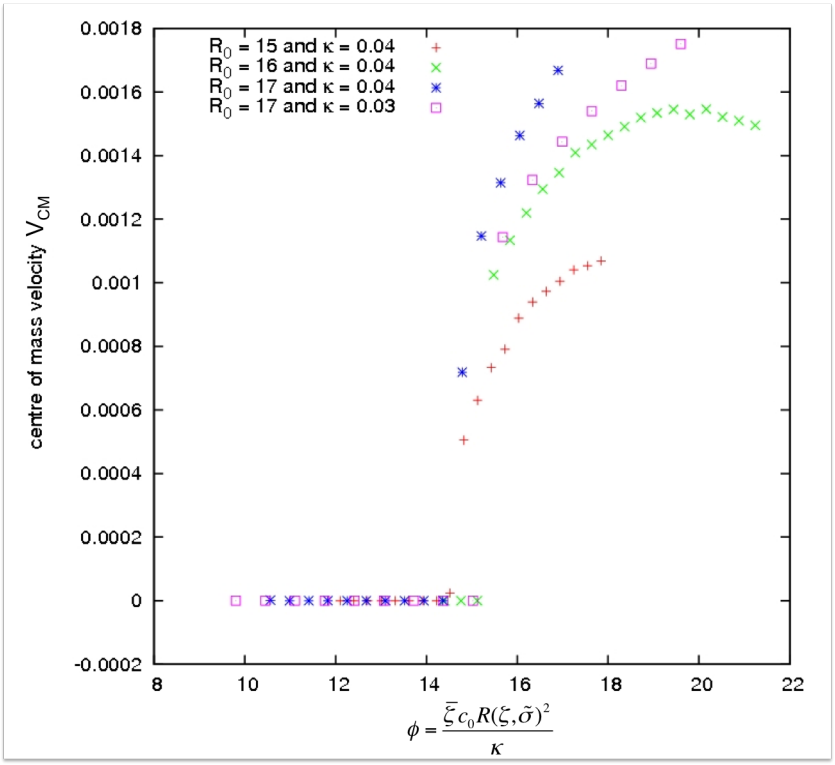

Figure 5.7: Plots of the droplet speed as a function of dimensionless parameter ϕ for different values of initial droplet radius $R_0 = R(\bar{\zeta} = 0, \tilde{\gamma})$ and elastic constant κ. All the four curves have the same critical value at $\phi \simeq 14.5$.

induced by either contractility or treadmilling only[2]. In cell crawling, it is expected that actin treadmilling is more dominant due to the presence of focal adhesions (high friction), whereas in cell swimming, it has been hypothesized that actin treadmilling is probably less dominant (low friction/w).

5.2.4 Simple scaling analysis

In the absence of self-advection and soft anchoring condition, we observe a stationary-to-motile transition at some critical activity $\bar{\zeta}_c$ which is accompanied by SSB of the global symmetry in Eqn. (5.6). As described above, below the critical activity $\bar{\zeta}_c$, the droplet remains stationary while the polarisation field is still uniform inside the droplet. However, the droplet shape is slightly elongated

[2]The only exception being the contractility-driven droplet velocity can be larger than that driven by both mechanisms in the low friction limit. This is because actin treadmilling can also induce a slight splay deformation which points in the opposite direction of actin polarisation.

due the competition between the active stress and the interfacial tension. In general the shortest radius of the elongated droplet is a function of the activity $\overline{\zeta}$ and surface tension $\widetilde{\gamma}$ or $R(\overline{\zeta}, \widetilde{\gamma})$.

At large enough activity, above the critical value $\overline{\zeta}_c$, the droplet becomes motile. This transition may be understood as driven by spontaneous elastic deformations - therefore the critical value $\overline{\zeta}_c$ can be estimated by equating the active and elastic stresses, as follows

$$\underline{\underline{\sigma}}^{active} \sim \underline{\underline{\sigma}}^{elastic} \tag{5.9}$$

From Eqns. (4.17-4.19), we also have $\underline{\underline{\sigma}}^{active} \sim \overline{\zeta} c_0$ and $\underline{\underline{\sigma}}^{elastic} \sim \frac{\kappa}{R^2}$ and hence we arrive at the following scaling law:

$$\overline{\zeta}_c \sim \frac{\kappa}{c_0 R(\overline{\zeta}_c, \widetilde{\gamma})^2} \tag{5.10}$$

which represents a mean-field estimate of the location of the critical point. Note that the surface tension $\widetilde{\gamma}$ will also depend on κ in general. This scaling law also has the same form as that of 1D spontaneous flow transition (see Eq. (3.22) in chapter 3). To test this scaling law, we may plot the droplet speed V_{CM} as a function of a dimensionless quantity:

$$\phi = \frac{\overline{\zeta} c_0 R(\overline{\zeta}, \widetilde{\gamma})^2}{\kappa} \tag{5.11}$$

near the critical point for different values of elastic constant κ and initial radius of the droplet $R_0 = R(\overline{\zeta} = 0, \widetilde{\gamma})$. These plots are shown in Fig. 5.7. We can see from the figure that all the four curves corresponding to different parameters have almost the same critical point $\phi \simeq 14.5$, thereby validating our approximate scaling analysis.

5.2.5 Alternative model with Q-tensor

Finally in this subsection, we shall look at the effects of active stresses on a truly nematic droplet whose hydrodynamic description is described by $\underline{\underline{Q}}$ tensor rather than $\mathbf{p}$. (The appropriate free energy functional and the respective equation of motion for $\underline{\underline{Q}}$ can be found in the appendix A.) In the case of nematic droplet

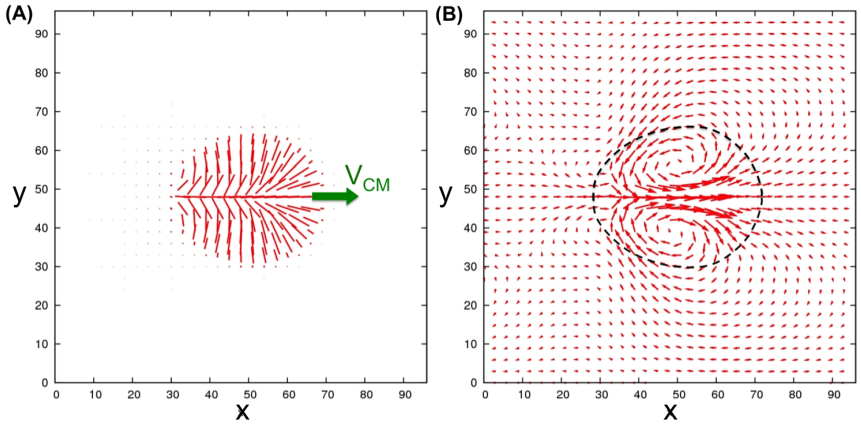

Figure 5.8: A droplet of active nematic ($Q_{\alpha\beta} > 0$ and $p_\alpha = 0$) can also become motile due to the active stress: $\sigma_{\alpha\beta} = \overline{\zeta} c Q_{\alpha\beta}$. **(A)** shows a typical configuration of the director field in a motile contractile droplet ($\overline{\zeta} > 0$) moving to the right. (The motile state shown in this figure corresponds to that in Fig. 5.4(C) of the polar droplet.) **(B)** shows the corresponding velocity field consisting of a pair of vortices inside the droplet. The dashed line represents the droplet interface.

($\underline{\underline{Q}} > 0$ and $\mathbf{p} = 0$), the form of the active stress becomes:

$$\sigma^a_{\alpha\beta} = -\zeta c Q_{\alpha\beta} \tag{5.12}$$

As mentioned above, the dynamics of the director field $\hat{\mathbf{n}}$ (which is defined to be the largest eigenvector of $\underline{\underline{Q}}$) should be similar to that of $\mathbf{p}$, as long as defects are not involved. Indeed for the nematic case, we also observe a SSB which is accompanied by a translational motion in the direction of splay (see Fig. 5.8). The global symmetry being broken in this case refers to a reflection of the whole plane about a line parallel to the y-axis and passes through the centre of mass of the droplet (not that of Eqn. (5.6)). The internal fluid flow generated by this contractile stress still consists of two opposite fluid vortices, similar to that in polar active droplets (Fig. 5.8).

5.3 SSB in extensile droplets can also induce motility

We shall now turn to the case of 2D extensile droplets. Continuum descriptions of extensile active fluids are widely used to describe dense bacterial suspensions [28, 38, 4]. These results may therefore be relevant to bacterial droplets formed by aggregation [90], or possibly by confinement within a droplet emulsion. More recently, Sanchez *et al.* [84] also studied a suspension of microtubules and kinesin motors confined to a droplet. These microtubules are cross-linked by kinesin motors which can walk along the tubules, very much like actomyosin systems except that microtubule-kinesin network is extensile rather than contractile. Although each microtubule is individually a polar filament, microtubule network displays a nematic order rather than polar, in which, there is an equal number of filaments pointing parallel and anti-parallel to each other. We again study the effects of an extensile stress in a 2D polar active droplet by first switching off self-advection/swimming term ($w = 0$) and coupling/anchoring term ($\beta = 0$).

Fig. 5.9(A) shows the steady state configurations of a 2D purely extensile droplet at different ranges of activity. For $\zeta < \zeta_{c1}$ the droplet remains stationary but again elongates symmetrically, this time along the direction of the polarisation field $\mathbf{p}$. In this regime, the extensile stress also creates an external quadrupolar flow field expected of a large, extensile shaker. For ζ beyond the critical value ζ_{c1}, the droplet again becomes unstable, but now with respect to bend deformation as opposed to splay. This instability gives rise to a horizontal vortex pair inside the droplet which causes the droplet to move in a direction of bend $\mathbf{p} \times (\nabla \times \mathbf{p})$ (which can be upwards or downwards according to Fig. 5.9(A)). As can be seen from the figure, this stationary-to-motile transition can still be characterised as a continuous SSB transition, however, the droplet speed V_{CM} attains a maximum value at some intermediate value of activity $\zeta \simeq 0.005$ before falling to zero again at a second critical activity ζ_{c2} (see Fig. 5.9(A)). Beyond the second critical activity threshold ζ_{c2}, the polarization pattern oscillates continuously (resembling a standing wave) without any overall motion.

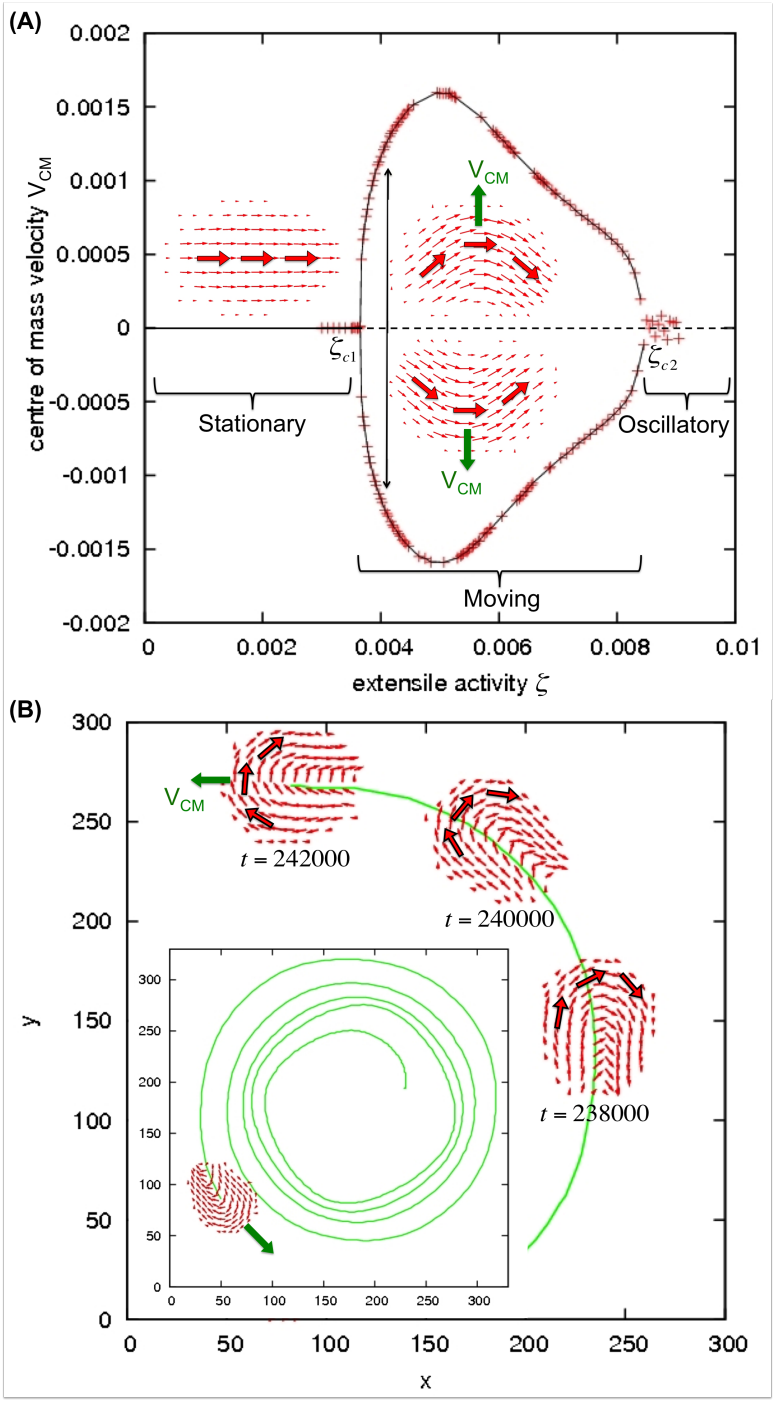

Figure 5.9: **(A)** Plot of center of mass velocity against activity ($\zeta > 0$) for extensile droplet without self-advection. It shows continuous transitions from stationary to motile and then from motile to oscillatory at critical activity ζ_{c1} and ζ_{c2} respectively. Also shown are the steady state polarization field $\mathbf{p}(\mathbf{r})$ for the stationary and motile case (red arrows). **(B)** The presence of both extensile stress and self-advection leads to an outward spiral trajectory (solid green lines).

5.3.1 Effect of treadmilling

Turning finally to the case of nonzero treadmilling/swimming speed ($w > 0$) we find that this, combined with the extensile motility, can give rise to a spiralling motion (see Fig. 5.9(B) inset). This motion arises because the SSB-induced extensile motility is at right angles to the polarization field (Fig. 5.9(B) right). On the other hand, the swimming term transports material along the polarization field locally. When combined, this leads to an outward spiral trajectory as shown in Fig. 5.9(B). (This is perhaps analogous to motion of charged particle in a magnetic field to certain degrees.) The reason why the resulting trajectory is a spiral rather than a circular one is because the presence of the swimming term slightly distorts the internal fluid flow generated by the active stress. More specifically, the pair of fluid vortices inside the droplet is no longer symmetrical about the centre of the droplet. This spiral motion contrasts with the contractile case where both the SSB-induced and the self-advective motion point either in the same direction or opposite direction and consequently only results in a straight line motion.

5.4 Summary

In conclusion, we showed that actomyosin contraction alone can also generate cellular motility due to the formation of a large scale hydrodynamic fluid flow inside the cell. (This internal fluid flow has the form of a vortex pair in 2D and a toroidal flow in 3D.) This motion is triggered by splay instabilities, which also spontaneously break a global inversion symmetry, and the direction of motion is determined by the direction of splay $(\nabla \cdot \mathbf{p})\mathbf{p}$. This is in contrast to another cellular motility driven mainly by actin polymerisation/treadmilling (plus focal adhesion) which transports the cell material locally in the direction of actin polarisation. We therefore hypothesize that cell swimming in a 3D viscous environment may be driven mainly by actomyosin contraction due to the lack of protrusion commonly associated with treadmilling. In the case of cell crawling however, both mechanisms are present and complementary to each other since the direction of splay in cell crawling $(\nabla \cdot \mathbf{p})\mathbf{p}$ is the same as that of actin polarisation $\mathbf{p}$ although actin treadmilling is probably more dominant due to high cell-surface friction.

Finally we also studied droplet motion driven by extensile stresses which interestingly, when combined with self-advection, can give rise to a spiralling motion. Recently droplets of extensile fluids have also been studied experimentally. Particularly, Sanchez *et al.* [84] found that droplets of microtubule-kinesin network can also spontaneously move on their own, although their droplet motion is much more random than ours. This is because the director field inside the droplet is continuously changing with time (resembling turbulence), unlike our simulated version of extensile droplets in Fig. 5.9 within which the polarisation field is static (steady state). (Recall that microtubule-kinesin has nematic order and extensile whereas actomyosin has polar order and contractile.) We hope, in the future, that our simulations may be reproduced in a controlled experiment.

In short summary we showed that even if the individual active particles are not moving (or shakers), inside a droplet, a collection of active particles can exhibit a cooperative behaviour. This is shown by the spontaneously moving state which is driven by internal fluid flow.

Chapter 6

Conclusion

Although microscopically bacterial suspensions and actomyosin solutions look very different from each other, macroscopically, they can look rather similar. In particular, we showed that they both can be described by the same set of hydrodynamic equations. The only difference is perhaps the sign of the internal active stresses (with bacterial suspensions generally being extensile and actomyosin solutions being contractile). This internal active stress plus a swimming/treadmilling term are two defining features in active fluids which drive the system to be out of equilibrium internally. As we have seen in numerous examples, the effects of these active terms ranges from turbulence in the bulk to a steadily moving state in a droplet.

For bacterial suspensions in the bulk we learnt that the internal active stresses can give rise to macroscopic fluid vortices which in our case are static, *i.e.* a non-equilibrium steady state. The turbulent state, on the other hand, is also observed but at a much higher value of activity (or equivalently, system size). We also discovered that in 2D systems, there exist more than one steady state with a non-equilibrium transition leading from one steady state to another. Most notably, some of these non-equilibrium steady states are characterised by a large out-of-plane fluid flow (in the case of quasi-2D geometry). Finally, the presence of self-advection (or swimming) on top of these active stresses can transform the steady state pattern into a travelling wave.

In the second part, we consider a droplet of contractile active fluid as a simple model of eukaryotic cells in a 3D viscous environment or on a 2D solid surface. The droplet motion, in this case, can be driven by actin treadmilling and/or

contractile stresses. As demonstrated in this thesis, contractile stresses alone can also induce motion due to the formation of internal fluid flow. This provides a new route to cellular motility which may be utilised by a swimming tumour cell. Droplet motion induced by actin-treadmilling, on the other hand, is already well understood and is shown to play a dominant role in cell crawling and grabbing. In particular, the formation of lamellipodial protrusion and filopodial protrusion can be attributed to the activity of actin filaments polymerising against the cell membrane. In the future, we hope that our hydrodynamic model of active droplets can be further improved by incorporating: (i) different viscosities for the two fluid phases and (ii) a colloid as a simple representation of cell nucleus. It is also hoped that our simple model can be of further use to study other physical aspects of cell motility such as cell migration through nanopores [91] and eukaryotic chemotaxis [92].

Our hydrodynamic model might also be applicable to other biological systems at larger length scales such as tissues [66]. For instance in tissues, we might treat each cell as a contractile unit which may interact with each other giving rise to a large scale hydrodynamic flow. Recall that in our droplet model of a eukaryotic cell, the contractile stress can elongate the droplet and produce a quadrupolar fluid flow externally (and thus we may treat the whole cell as a single contractile shaker). Experimentally, this large scale hydrodynamic flow has been observed in developing chick embryo [93] and interestingly, this internal fluid flow also looks similar to ours (which consists of a pair of opposite fluid vortices).

Finally, we shall conclude this thesis with some unanswered questions that we shall leave to future work. Firstly, the nematic-to-polar transition (especially in bacterial suspensions) is still largely unexplained. Although we briefly mentioned that this non-equilibrium transition might be driven by the swimming speed of the individual bacteria, the nature of this transition is still unknown (whether it is a first order/second order transition). Even more, equilibrium nematic-to-polar transition is also not well studied in literature. For instance, how will the defect dynamics change close to nematic-to-polar transition? - with the former preferring two half-integer defects and the latter preferring a single integer defect. Secondly, our model for the eukaryotic cells is a rather simple one in which we approximate the presence of a cell membrane by a surface tension. This undoubtedly raises some new questions such as: how can we prevent two cells

from coalescing (if we want to simulate two crawling cells)? and how can we better model the cell-surface interaction? The last question, for instance, might be relevant if we want to simulate a swimming cell passing through a nanopore.

Appendix A

A free energy functional describing equilibrium nematic-to-polar transition

In this appendix, we shall briefly discuss how we may extend the free energy functional described in the main text to account for nematic-to-polar transition. This may be useful to study non-equilibrium nematic-to-polar transition in a dense suspension of microscopic swimmers as described in chapter 3. A free energy functional containing both nematic order parameter ($Q_{\alpha\beta}$) and polar order parameter (p_α) has actually been derived in Pleiner *et al.* [94] and Wittkowski *et al.* [95]. Here in this appendix, we shall discuss how we may apply it to a droplet.

The free energy density is now a function of scalar order parameter c, vector order parameter p_α, and tensorial order parameter $Q_{\alpha\beta}$:

$$\begin{aligned} f(\phi, p_\alpha, Q_{\alpha\beta}) \;=\; & \frac{a}{2c_r^2}c^2(c-c_0)^2 + \frac{k}{2}\left|\nabla c\right|^2 \\ & + \frac{A_0}{2}\left(1-\frac{\gamma(c)}{3}\right)\mathrm{Tr}(\mathbf{Q}^2) - \frac{A_0\gamma(c)}{3}\mathrm{Tr}(\mathbf{Q}^3) + \frac{A_0\gamma(c)}{4}\left(\mathrm{Tr}(\mathbf{Q}^2)\right)^2 \\ & + \frac{K}{2}(\partial_\gamma Q_{\alpha\beta})^2 + \frac{\beta_2}{2}p_\alpha Q_{\alpha\beta}p_\beta \\ & - \frac{\alpha}{2}\left(ct-1\right)\left|\mathbf{p}\right|^2 + \frac{\alpha}{4}\left|\mathbf{p}\right|^4 + \frac{\kappa}{2}(\partial_\alpha p_\beta)^2 \end{aligned} \tag{A.1}$$

c is defined such that $c \simeq c_0$ inside the droplet and $c = 0$ outside the droplet. The k-term is related to the surface tension and this term also creates a smooth

diffuse interface across the droplet. We have a first order equilibrium transition from isotropic to nematic when $\gamma(c) \simeq 2.7$ [59, 96]. We choose $\gamma(c)$ to have the following form:

$$\gamma(c) = 2.5 + 0.5\frac{c}{c_0} \tag{A.2}$$

to ensure that we always have nematic order ($Q_{\alpha\beta} > 0$) inside the droplet and isotropic state outside ($Q_{\alpha\beta} = 0$). The parameter $K > 0$ here represents the effective elastic constant.

Here, we only have the simplest third order coupled term between $Q_{\alpha\beta}$ and P_α. Other higher order coupled terms are also possible [94]. The coupling coefficient β_2 is taken to be negative so that during nematic-to-polar transition, P_α will try to align either parallel or anti-parallel to the director field $\hat{n}_\alpha$. Note that the coupled term also ensures one cannot have polar order ($P_\alpha > 0$) without some nematic order ($Q_{\alpha\beta} > 0$).

Finally, the parameter t gives an equilibrium second order transition from nematic ($t < 0$) to polar state ($t > 0$) inside the droplet. For example, quenching the system from $t < 0$ to $t > 0$ will create domain walls which separate the droplet into regions where P_α is parallel or anti-parallel to $\hat{n}_\alpha$ (see Fig. A.1). Unlike K, the parameter κ in this context is not the elastic constant, but rather plays the role of the rate at which the domain walls coarsen with time. This coarsening kinetics is somehow similar to the Ising model [42]. In addition, we can also have a non-equilibrium nematic-to-polar transition as described in chapter 3. This happens if there is some activity which drives the system to be out-of-equilibrium internally (for example, if the particles are also swimming in the direction of their polarities). In this case, a droplet of swimmers in nematic state can become unstable with respect to small fluctuations and leads to a phase separation into two polar droplets with opposite polarities (see Fig. 3.3 of chapter 3).

The dynamics for the nematic order parameter $Q_{\alpha\beta}$ follows Beris-Edwards equation [59]:

$$\frac{\partial Q_{\alpha\beta}}{\partial t} + (u_\gamma + wP_\gamma)\partial_\gamma Q_{\alpha\beta} - S_{\alpha\beta}(\underline{\underline{\mathbf{Q}}}, \nabla\mathbf{u}) = -\Gamma_Q \nabla \frac{\delta F}{\delta Q_{\alpha\beta}} \tag{A.3}$$

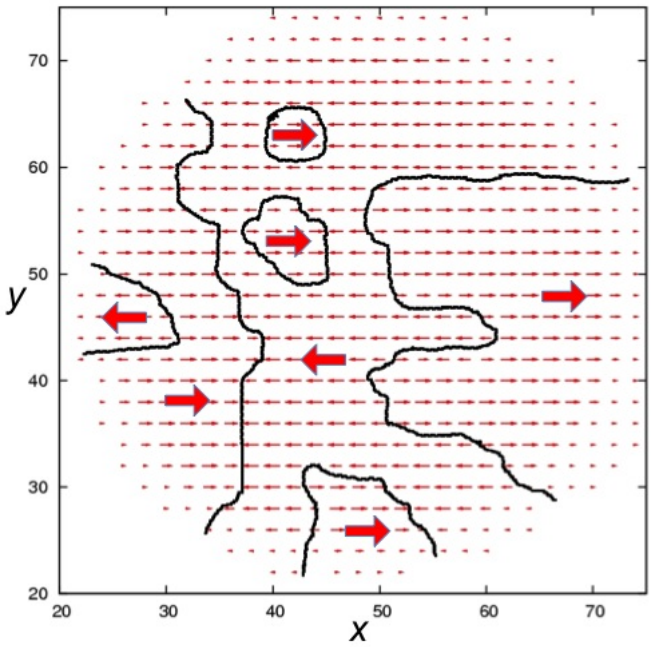

Figure A.1: **Equilibrium nematic-to-polar transition in a droplet.** The droplet is initially in a nematic state with uniform director field aligned horizontally in the x-direction. The system is then quenched from $t < 0$ (favouring nematic phase) to $t > 0$ (favouring polar phase). Outside the droplet, we have a 'vacuum' ($c = 0$) and isotropic state ($Q_{\alpha\beta} = 0$ and $p_\alpha = 0$).

where $\underline{\underline{\mathbf{S}}}$ is the rotational advection which has the following form:

$$\begin{aligned} S_{\alpha\beta}(\underline{\underline{\mathbf{Q}}}, \nabla \mathbf{u}) &= (\xi v_{\alpha\gamma} + \Omega_{\alpha\gamma})(Q_{\gamma\beta} + \frac{1}{3}\delta_{\gamma\beta}) + (Q_{\alpha\gamma} + \frac{1}{3}\delta_{\alpha\gamma})(\xi v_{\gamma\beta} - \Omega_{\gamma\beta}) \\ &\quad -2\xi(Q_{\alpha\beta} + \frac{1}{3}\delta_{\alpha\beta})\mathrm{Tr}(Q_{\alpha\beta}\nabla_\alpha u_\beta) \end{aligned} \tag{A.4}$$

(See main text for the definitions of ξ, $v_{\alpha\beta}$ and $\Omega_{\alpha\beta}$.) The time-evolutions for c, $\mathbf{p}$ and the fluid velocity $\mathbf{u}$ are the same and they are already presented in the main text.

Appendix B

Torque balance in nematic and polar liquid crystals

In the main text we showed that the hydrodynamic stress due to some elastic deformations in the liquid crystals can be written as (*cf.* Eqn. (4.18) from chapter 4):

$$\sigma_{\alpha\beta}^{elastic} = \frac{1}{2}(p_\alpha h_\beta - p_\beta h_\alpha) - \frac{\xi}{2}(p_\alpha h_\beta + p_\beta h_\alpha) - \kappa \partial_\alpha p_\gamma \partial_\beta p_\gamma \tag{B.1}$$

In chapter 4, we also showed how the last term in the expression above can be derived by considering a small translation on the material volume. Here, we shall briefly outline how we may obtain the rest of the terms in the equation above (for more detail, see Ref. [35]).

Suppose we rotate a volume of material V with some angular velocity ω. The fluid velocity inside the volume will then be (assuming the fluid rotates like a rigid body at steady state): $\mathbf{u} = \omega \times \mathbf{r}$. Similarly if the polarisation field $\mathbf{p}$ rotates like a rigid body, the rate of change of $\mathbf{p}$ will be: $\frac{D\mathbf{p}}{Dt} = \omega \times \mathbf{p}$. However in reality, liquid crystals do not rotate like a rigid body (hence the shear-aligning/tumbling parameter ξ) and the rate of change of $\mathbf{p}$ should be [78]:

$$\frac{D\mathbf{p}}{Dt} = \underbrace{-\underline{\underline{\Omega}} \cdot \mathbf{p}}_{\text{rigid body rotation}} + \xi \underline{\underline{v}} \cdot \mathbf{p} \tag{B.2}$$

where $\frac{D}{Dt} = \frac{\partial}{\partial t} + \mathbf{u} \cdot \nabla$ is the material derivative. $\underline{\underline{v}}$ and $\underline{\underline{\Omega}}$ are the symmetric and

anti-symmetric parts of the velocity gradient tensor $\nabla\mathbf{u}$:

$$\begin{aligned} v_{\alpha\beta} &= \frac{1}{2}(\partial_\alpha u_\beta + \partial_\beta u_\alpha) \\ \Omega_{\alpha\beta} &= \frac{1}{2}(\partial_\alpha u_\beta - \partial_\beta u_\alpha) \end{aligned} \tag{B.3}$$

The first term in Eqn. (B.2) represents a rigid body rotation and we can relate $\underline{\underline{\Omega}}$ in that equation to the angular velocity ω *via*

$$2\omega_\alpha = \epsilon_{\alpha\beta\gamma}\Omega_{\beta\gamma} \tag{B.4}$$

where the Levi-Civita symbol is defined to be:

$$\epsilon_{\alpha\beta\gamma} = \begin{cases} 1 & \text{, for } (\alpha,\beta,\gamma) = (1,2,3) = (2,3,1) = (3,1,2) \\ -1 & \text{, for } (\alpha,\beta,\gamma) = (1,3,2) = (3,2,1) = (2,1,3) \\ 0 & \text{, for } \alpha = \beta \text{ or } \beta = \gamma \text{ or } \gamma = \alpha \end{cases} \tag{B.5}$$

Now the rate of change in the free energy is given by (we neglect heat dissipation due to fluid viscosities for simplicity)

$$\begin{aligned} \frac{dF}{dt} &= \frac{d}{dt}\int_V f\, dV \\ &= \int_V \frac{Df}{Dt}\, dV \\ &= \int_V \left\{ \frac{\partial f}{\partial p_\alpha}\frac{Dp_\alpha}{Dt} + \frac{\partial f}{\partial(\partial_\alpha p_\beta)}\partial_\alpha\left(\frac{Dp_\beta}{Dt}\right)\right\} dV \\ &= \int_V h_\alpha \frac{Dp_\alpha}{Dt}\, dV + \oint_{\partial V} \frac{\partial f}{\partial(\partial_\alpha p_\beta)}\frac{Dp_\beta}{Dt}\, dS_\alpha \end{aligned} \tag{B.6}$$

where ∂V is the surface bounding the volume V. The second line above comes from Reynolds transport theorem. Substituting Eqn. (B.2) into the equation above, we have

$$\begin{aligned} \frac{dF}{dt} &= \int_V h_\alpha(-\Omega_{\alpha\beta}p_\beta + \xi v_{\alpha\beta}p_\beta)\, dV + \oint_{\partial V} \dots \\ &= \int_V (\Omega_{\alpha\beta}p_\alpha h_\beta + \xi v_{\alpha\beta}p_\alpha h_\beta)\, dV + \oint_{\partial V} \dots \end{aligned} \tag{B.7}$$

Now we can split $p_\alpha h_\beta$ into symmetric and anti-symmetric parts: $\frac{1}{2}(p_\alpha h_\beta + p_\beta h_\alpha)$

and $\frac{1}{2}(p_\alpha h_\beta - p_\beta h_\alpha)$ so that the expression above becomes

$$\frac{dF}{dt} = \int_V \left[\Omega_{\alpha\beta} \frac{1}{2}(p_\alpha h_\beta - p_\beta h_\alpha) + v_{\alpha\beta} \frac{\xi}{2}(p_\alpha h_\beta + p_\beta h_\alpha) \right] dV + \oint_{\partial V} \dots \tag{B.8}$$

where we have used the following identity: $\chi_{\alpha\beta}\tau_{\alpha\beta} = 0$ for any arbitrary symmetric tensor $\chi_{\alpha\beta}$ and anti-symmetric tensor $\tau_{\alpha\beta}$.

The rate of work being done on the material volume V by the surrounding (*i.e.* the container) is given by

$$\begin{aligned} \frac{dW}{dt} &= \int_V \mathbf{f} \cdot \mathbf{u} \, dV \\ &= \int_V \frac{\partial \sigma_{\alpha\beta}}{\partial r_\beta} u_\alpha \, dV \\ &= -\int_V \sigma_{\alpha\beta} \partial_\beta u_\alpha \, dV + \oint_{\partial V} u_\alpha \sigma_{\alpha\beta} \, dS_\beta \\ &= \int_V \sigma_{\alpha\beta}(\Omega_{\alpha\beta} - v_{\alpha\beta}) \, dV + \oint_{\partial V} u_\alpha \sigma_{\alpha\beta} \, dS_\beta \end{aligned} \tag{B.9}$$

where $f_\alpha = \partial_\beta \sigma_{\alpha\beta}$ is the force density. As before we split the stress tensor $\sigma_{\alpha\beta}$ into symmetric and anti-symmetric parts: $\sigma^{sym}_{\alpha\beta}$ and $\sigma^{anti}_{\alpha\beta}$ respectively and the equation above now becomes

$$\frac{dW}{dt} = \int_V (\Omega_{\alpha\beta}\sigma^{anti}_{\alpha\beta} - v_{\alpha\beta}\sigma^{sym}_{\alpha\beta}) \, dV + \oint_{\partial V} \cdots \tag{B.10}$$

Since we have $\frac{dW}{dt} = \frac{dF}{dt}$ (neglecting heat dissipation), we can now compare the bulk terms $\int_V dV$ in Eqn. (B.8) to those in Eqn. (B.10), from which we derive the elastic stress tensor:

$$\begin{aligned} \sigma^{anti}_{\alpha\beta} &= \frac{1}{2}(p_\alpha h_\beta - p_\beta h_\alpha) \\ \sigma^{sym}_{\alpha\beta} &= -\frac{\xi}{2}(p_\alpha h_\beta + p_\beta h_\alpha) \end{aligned} \tag{B.11}$$

To briefly summarise, the elastic stress tensor in the momentum balance equation can be found in the following way. First, we perform a translation on some material volume and compute the free energy difference. Second, we rotate the same material volume with a fixed angular velocity and compute the free energy difference (neglecting viscous dissipation). The results from each

mode are then added together to give the elastic stress. The dissipative viscous stress term, on the other hand, is assumed to be the same as that of isotropic fluids: $\sigma^d_{\alpha\beta} = 2\eta v_{\alpha\beta}$. In general for liquid crystals, the viscous shear stress is also different and this depends on whether the shear flow is parallel/perpendicular to the polarisation field. Effectively, we are assuming the shear viscosities η_i's to be the same for all modes of shearing - similar to the single elastic constant approximation which we did in chapter 3.

Elastic stress term for nematic liquid crystals

For nematic liquid crystals, we have a free energy functional which depends on a tensorial order parameter $\underline{\underline{\mathbf{Q}}}$: $F = \int_V f(Q_{\alpha\beta}, \partial_\alpha Q_{\beta\gamma})\, dV$ and also an equation of motion for the order parameter: $\frac{DQ_{\alpha\beta}}{Dt} = \ldots$ which are both given in appendix A and Ref. [59]. The derivation for the elastic stress above (as well as in chapter 4) can be repeated for the $\mathbf{Q}$-tensor and the result is [59, 5, 96]:

$$\begin{aligned}
\sigma^{elastic}_{\alpha\beta} &= Q_{\alpha\gamma}H_{\gamma\beta} - Q_{\beta\gamma}H_{\gamma\alpha} \\
&\quad +2\xi\left(Q_{\alpha\beta} - \frac{1}{3}\delta_{\alpha\beta}\right)\mathbf{Q}:\mathbf{H} - \partial_\beta Q_{\gamma\nu}\frac{\delta F}{\delta\partial_\alpha Q_{\gamma\nu}} \\
&\quad -\xi H_{\alpha\gamma}\left(Q_{\gamma\beta} - \frac{1}{3}\delta_{\gamma\beta}\right) - \xi H_{\beta\gamma}\left(Q_{\gamma\alpha} - \frac{1}{3}\delta_{\gamma\alpha}\right)
\end{aligned} \tag{B.12}$$

where $\mathbf{H} = -\frac{\delta F}{\delta \mathbf{Q}} + \frac{\mathbf{I}}{3}\mathrm{Tr}\left(\frac{\delta F}{\delta \mathbf{Q}}\right)$ is the molecular field.

Bibliography

[1] M. F. Copeland and D. B. Weibel. Bacterial swarming: a model system for studying dynamic self-assembly. *Soft Matter*, 5:1174–1187, 2008.

[2] K. Drescher, J. Dunkel, L. H. Cisneros, S. Ganguly, and R. E. Goldstein. Fluid dynamics and noise in bacterial cell–cell and cell–surface scattering. *PNAS*, 108(27):10940–10945, 2010.

[3] R. Phillips, J. Kondev, and J. Theriot. *Physical Biology of the Cell.* Garland Science, 1st edition, 2009.

[4] Y. Hatwalne, S. Ramaswamy, M. Rao, and R. A. Simha. Rheology of active-particle suspensions. *PRL*, 92:118101, 2004.

[5] C. Denniston, D. Marenduzzo, E. Orlandini, and J.M. Yeomans. Lattice boltzmann algorithm for three-dimensional liquid-crystal hydrodynamics. *Phil. Trans. R. Soc. Lond. A*, 362:1745–1754, 2004.

[6] J. Toner and Y. H. Tu. Flocks, herds, and schools: A quantitative theory of flocking. *PRE*, 58(4):4828, 1998.

[7] T. Vicsek, A. Czirók, E. Ben-Jacob, I. Cohen, and O. Shochet. Novel type of phase transition in a system of self-driven particles. *PRL*, 75:1226–1229, 1995.

[8] R. A. Simha and S. Ramaswamy. Hydrodynamic fluctuations and instabilities in ordered suspensions of self-propelled particles. *PRL*, 89(5):058101, 2002.

[9] G Gregoire and H Chate. Onset of collective and cohesive motion. *PRL*, 92(2):025702, 2004.

[10] E. L. Barnhart, K. C. Lee, K. Keren, A. Mogilner, and J. A. Theriot. An adhesion-dependent switch between mehanisms that determine motile cell shape. *PLoS Biology*, 9(5):e1001059, 2011.

[11] P. T. Yam, C. A. Wilson, L. Ji, B. Hebert, E. L. Barnhart, N. A. Dye, P. W. Wiseman, G. Danuser, and J. A. Theriot. Actin–myosin network reorganization breaks symmetry at the cell rear to spontaneously initiate polarized cell motility. *JCB*, 178:1207–1221, 2007.

[12] R. Poincloux, O. Collin, F. Lizarraga, M. Romao, M. Debray, M. Piel, and P. Chavrier. Contractility of the cell rear drives invasion of breast tumor cells in 3d matrigel. *PNAS*, 108(5):1943–1948, 2011.

[13] J. C. Adams. Cell-matrix contact structures. *Cell Mol. Life Sci.*, 58:371–92, 2001.

[14] D. Pantaloni, C. Le Clainche, and M. F. Carlier. Cell biology - mechanism of actin-based motility. *Science*, 292:1502–1506, 2001.

[15] P. Nelson. *Biological Physics: Energy, Information, Life.* W. H. Freeman, 1st edition, 2007.

[16] P. Friedl and K. Wolf. Tumour-cell invasion and migration: diversity and escape mechanisms. *Nature Reviews Cancer*, 3:362–374, 2003.

[17] R. J. Hawkins, R. Poincloux, O. Benichou, M. Piel, P. Chavrier, and R. Voituriez. Spontaneous contractility-mediated cortical flow generates cell migration in 3-dimensional environments. *Biophys. J.*, 101:1041, 2011.

[18] B. Rubinstein, M. F. Fournier, K. Jacobson, A. Verkhovsky, and A. Mogilner. Actin-myosin viscoelastic flow in the keratocyte lamellipod. *Biophys. J.*, 97:1853–1863, 2009.

[19] K. Keren, Z. Pinchus, G. M. Allen, E. L. Barnhart, G. Marriott, A. Mogilner, and J. A. Theriot. Mechanism of shape determination in motile cells. *Nature*, 453:475–480, 2008.

[20] T. E. Faber. *Fluid Dynamics for Physicists.* Cambridge University Press, 1995.

[21] V. Narayan, S. Ramaswamy, and N. Menon. Long-lived giant number fluctuations in a swarming granular nematic. *Science*, 317(5834):105–108, 2007.

[22] W. Bialek, A. Cavagna, I. Giardina, T. Mora, E. Silvestri, M. Viale, and A. M. Walczak. Statistical mechanics for natural flocks of birds. *PNAS*, 109(13):4786–4791, 2012.

[23] M. E. Cates, D. Marenduzzo, I. Pagonabarraga, and J. Tailleur. Arrested phase separation in reproducing bacteria creates a generic route to pattern formation. *PNAS*, 107(26):11715–11720, 2010.

[24] C. W. Wolgemuth. Collective swimming and the dynamics of bacterial turbulence. *Biophys. J.*, 95:1564–1574, 2008.

[25] K. I. Anderson, Y. L. Wang, and J. V. Small. Coordination of protrusion and translocation of the keratocyte involves rolling of the cell body. *J. Cell Biol.*, 134(5):1209–1218, 1996.

[26] G. Salbreux, J. Prost, and J. F. Joanny. Hydrodynamics of cellular cortical flows and the formation of contractile rings. *PRL*, 103:058102, 2009.

[27] P. Lee and C. W. Wolgemuth. Crawling cells can close wounds without purse strings or signaling. *PLoS Computational Biology*, 7(3):e1002007, 2011.

[28] A. Baskaran and M. C. Marchetti. Statistical mechanics and hydrodynamics of bacterial suspensions. *PNAS*, 106(37):15567–15572, 2009.

[29] W. Kung and M. C. Marchetti. Hydrodynamics of polar liquid crystals. *PRE*, 73:031708, 2006.

[30] E. M. Purcell. Life at low reynolds number. *Am. J. Phys.*, 45:3–11, 1977.

[31] G. Forgacs, R. A. Foty, Y. Shafrir, and M. S. Steinberg. Viscoelastic properties of living embryonic tissues: a quantitative study. *Biophys. J.*, 74:2227–2234, 1998.

[32] O. M. Rossier, N. Gauthier, N. Biais, W. Vonnegut, M-. A. Fardin, P. Avigan, E. R. Heller, A. Mathur, S. Ghassemi, M. S. Koeckert, J. C. Hone, and M. P. Sheetz. Force generated by actomyosin contraction builds bridges between adhesive contacts the embo force generated by actomyosin contraction builds bridges between adhesive contacts. *EMBO Journal*, 29:1055–1068, 2010.

[33] A. B. Verkhovsky, T. M. Svitkina, and G. G. Borisy. Self-polarization and directional motility of cytoplasm. *Curr. Biol.*, 9(1):11–20, 1998.

[34] U. Euteneuer and M. Schliwa. Persistent, directional motility of cells and cytoplasmic fragments in the absence of microtubules. *Nature*, 310(5972):58–61, 1984.

[35] P. G. de Gennes and J. Prost. *The Physics of Liquid Crystals*. Clarendon Press, 1993.

[36] R. Voituriez, J. F. Joanny, and J. Prost. Spontaneous flow transition in active polar gels. *EPL*, 70(3):404–410, 2005.

[37] A. Najafi and R. Golestanian. Simple swimmer at low reynolds number: Three linked spheres. *PRE*, 69:062901, 2004.

[38] M. E. Cates, S. M. Fielding, D. Marenduzzo, E. Orlandini, and J. M. Yeomans. Shearing active gels close to the isotropic-nematic transition. *PRL*, 101:068102, 2008.

[39] G. Foffano, J. S. Lintuvuori, K. Stratford, M. E. Cates, and D. Marenduzzo. Colloids in active fluids: Anomalous microrheology and negative drag. *PRL*, 109:028103, 2012.

[40] E. Tjhung, M. E. Cates, and D. Marenduzzo. Nonequilibrium steady states in polar active fluids. *Soft Matter*, 7:7453–7464, 2011.

[41] J. S. Bois, F. Julicher, and S. W. Grill. Pattern formation in active fluids. *PRL*, 106:028103, 2011.

[42] A. J. Bray. Theory of phase-ordering kinetics. *Advances in Physics*, 51:481–587, 2002.

[43] M. E. Cates, O. Henrich, D. Marenduzzo, and K. Stratford. Lattice boltzmann simulations of liquid crystalline fluids: active gels and blue phases. *Soft Matter*, 5:3791–3800, 2009.

[44] M.R. Swift, E. Orlandini, W. R. Osborn, and J. M. Yeomans. Lattice boltzmann simulations of liquid-gas and binary fluid systems. *PRE*, 54:5041–5052, 1996.

[45] R. Benzi, S. Succi, and M. Vergassola. The lattice boltzmann equation: theory and applications. *Phys. Rep.*, pages 145–197, 1992.

[46] S. Succi. *The Lattice Boltzmann Equation for Fluid Dynamics and Beyond*. Oxford University Press, 1st edition, 2001.

[47] P.L. Bhatnagar, E.P. Gross, and M. Krook. A model for collision processes in gases. i. small amplitude processes in charged and neutral one-component systems. *PRE*, 94:511–525, 1954.

[48] S. Chapman and T. G. Cowling. *The mathematical theory of non-uniform gases: an account of the kinetic theory of viscosity, thermal conduction, and diffusion in gases*. Cambridge University Press, 1st edition, 1990.

[49] C. M. Pooley and K. Furtado. Eliminating spurious velocities in the free-energy lattice boltzmann method. *PRE*, 77:046702, 2008.

[50] K. Wolff, D. Marenduzzo, and M. E. Cates. Cytoplasmic streaming in plant cells: the role of wall slip. *J. Roy. Soc. Interface*, 71:1398–408, 2012.

[51] G. Li, J. Bensson, L. Nisimova, D. Munger, P. Mahautmr, J. X. Tang, M. R. Maxey, and Y. V. Brun. Accumulation of swimming bacteria near a solid surface. *PRE*, 84:041932, 2011.

[52] Eric Lauga, W. R. DiLuzio, G. M. Whitesides, and H. A. Stone. Swimming in circles: Motion of bacteria near solid boundaries. *Biophys. J.*, 90:400–412, 2006.

[53] R. W. Nash, R. Adhikari, and M. E. Cates. Singular forces and pointlike colloids in lattice boltzmann hydrodynamics. *PRE*, 77:026709, 2008.

[54] R. W. Nash, R. Adhikari, J. Tailleur, and M. E. Cates. Run-and-tumble particles with hydrodynamics: Sedimentation, trapping, and upstream swimming. *PRL*, 104:258101, 2010.

[55] P. M. Chaikin and T. C. Lubensky. *Principles of Condensed Matter Physics*. Cambridge University Press, 2000.

[56] L. H. Cisneros, J. O. Kessler, S. Ganguly, and R. E. Goldstein. Dynamics of swimming bacteria: transition to directional order at high concentration. *PRE*, 83:061907, 2011.

[57] J. F. Joanny, F. Jülicher, K. Kruse, and J. Prost. Hydrodynamic theory for multi-component active polar gels. *New J. Phys.*, 9:422, 2007.

[58] M. J. Schnitzer. Theory of continuum random walks and application to chemotaxis. *PRE*, 48:2553–2568, 1993.

[59] A. N. Beris and B. J. Edwards. *Thermodynamics of Flowing Systems: with Internal Microstructure*. Oxford Engineering Science Series, 1994.

[60] S. A. Edwards and J. M. Yeomans. Spontaneous flow states in active nematics: A unified picture. *EPL*, 85:18008, 2009.

[61] S. Strogatz. *Nonlinear Dynamics and Chaos*. Perseus Books, 2000.

[62] S. Rafai, L. Jibuti, and P. Peyla. Effective viscosity of microswimmer suspensions. *PRL*, 104:098102, 2010.

[63] S. M. Fielding, D. Marenduzzo, and M. E. Cates. Nonlinear dynamics and rheology of active fluids: simulations in two dimensions. *PRE*, 83:041910, 2011.

[64] J. A. Theriot and T. J. Mitchison. Actin microfilament dynamics in locomoting cells. *Nature*, 352:126–131, 1991.

[65] A. Mogilner. Mathematics of cell motility: have we got its number. *J. Math. Biol.*, 58:105–134, 2009.

[66] M. Basan, T. Risler, J. F. Joanny, X. Sastre-Garau, and J. Prost. Homeostatic competition drives tumor growth and metastasis nucleation. *HFSP Journal*, 3(4):265–272, 2009.

[67] C. S. Peskin, G. M. Odell, and G. F. Oster. Cellular motions and thermal fluctuations: the brownian ratchet. *Biophys. J.*, 65:316–324, 1993.

[68] A. Mogilner and G. Oster. Cell motility driven by actin polymerization. *Biophys. J.*, 71:3030–3045, 1996.

[69] M. Prass, K. Jacobson, A. Mogilner, and M. Radmacher. Direct measurement of the laemillipodial protrusive force in a migrating cell. *JCB: Report*, 174(6):767–772, 2006.

[70] F. Heinemann, H. Doschke, and M. Radmacher. Keratocyte lamellipodial protrusion is characterized by a concave force-velocity relation. *Biophys. J.*, 100(6):1420–1427, 2011.

[71] R. Feynman. *Feynman Lectures on Physics*. Addison Wesley, 1st edition, 2011.

[72] T.B. Liverpool and M.C. Marchetti. Rheology of active filament solutions. *PRL*, 97:268101, 2006.

[73] T.B. Liverpool and M.C. Marchetti. Bridging the microscopic and the hydrodynamic in active filament solutions. *EPL*, 69:846–852, 2005.

[74] K. Burridge and M. Chrzanowska-Wodnicka. Focal adhesions, contractility, and signaling. *Annu. Rev. Cell Dev. Biol.*, 12:463–518, 1996.

[75] M. Lenz, M. L. Gardel, and A. R. Dinner. Requirements for contractility in disordered cytoskeletal bundles. *New J. Phys.*, 14:033037, 2012.

[76] M. Lenz, T. Thoresen, M. L. Gardel, and A. R. Dinner. Contractile units in disordered actomyosin bundles arise from f-actin buckling. *PRL*, 108:238107, 2012.

[77] S. R. deGroot and P. Mazur. *Non-Equilibrium Thermodynamics*. Dover Publications, 2011.

[78] L. D. Landau and E. M. Lifshitz. *Theory of Elasticity*. Butterworth-Heinemann, 1986.

[79] A. Tiribocchi, N. Stella, G. Gonnella, and A. Lamura. Hybrid lattice boltzmann model for binary fluid mixtures. *PRE*, 80:026701, 2009.

[80] M. E. Cates, K. Stratford, R. Adhikari, P. Stansell, J. C. Desplat, I. Pagonabarraga, and A. J. Wagner. Simulating colloid hydrodynamics with lattice boltzmann method. *J. Phys. Cond. Mat.*, 16:S3903–S3915, 2004.

[81] M. A. Wozniak, K. Modzelewska, L. Kwong, and P. J. Keely. Focal adhesion regulation of cell behavior. *Biochimica et Biophysica Acta*, 1692:103–119, 2004.

[82] S. A. Sandersius, M. Chuai, C. J. Weijer, and T. J. Newman. A 'chemotactic dipole' mechanism for large-scale vortex motion during primitive streak formation in the chick embryo. *Phys. Biol.*, 8:045008, 2011.

[83] T. Sanchez, D. Welch, D. Nicastro, and Z. Dogic. Cilia-like beating of active microtubule bundles. *Science*, pages 456–459, 2011.

[84] T. Sanchez, D. T. N. Chen, S. J. DeCamp, M. Heymann, and Z. Dogic. Spontaneous motion in hierarchically assembled active matter. *Nature*, 491:431–435, 2012.

[85] S. Ramaswamy. The mechanics and statistics of active matter. *Annu. Rev. Condens. Matter Phys.*, 1:323–45, 2010.

[86] M. Schmitt and H. Stark. Swimming active droplet: A theoretical analysis. *Eur. Lett.*, (in press), 2013.

[87] S. Yabunaka, T. Ohta, and N. Yoshinaga. Spontaneous motion of a droplet coupled with a chemical wave. *J. Chem. Phys.*, 136:074904, 2012.

[88] L. Giomi and M. C. Marchetti. Polar patterns in active fluids. *Soft Matter*, 8:129–139, 2012.

[89] L. Berthier and J. Kurchan. Nonequilibrium glass transitions in driven and active matter. *Nature Physics*, (in press), 2013.

[90] J. Schwarz-Linek, C. Valeriani, A. Cacciuto, M. E. Cates, D. Marenduzzo, A. N. Morozov, and W. C. K. Poon. Phase separation and rotor self-assembly in active particle suspensions. *PNAS*, 109:4052, 2012.

[91] H. A. Pan, J. Y. Liang, Y. C. Hung, C. H. Lee, J. C. Chiou, and G. S. Huang. The spatial and temporal control of cell migration by nanoporous surfaces through the regulation of erk and integrins in fibroblasts. *Biomaterials*, 34:841–853, 2013.

[92] H. Levine and W. J. Rappel. The physics of eukaryotic chemotaxis. *Physics Today*, 66:24, 2013.

[93] D. Dormann and C. J. Weijer. Imaging of cell migration. *EMBO J.*, 25:3480–3493, 2006.

[94] H. Pleiner, E. Jarkova, H. W. Muller, and H. R. Brand. Landau description of ferrofluid to ferronematic phase transition. *Magnetohydrodynamics*, 37:254–260, 2001.

[95] R. Wittkowski, H. Löwen, and H. R. Brand. Microscopic and macroscopic theories for the dynamics of polar liquid crystals. *PRE*, 84:041708, 2011.

[96] O. Henrich, K. Stratford, D. Marenduzzo, and M. E. Cates. Ordering dynamics of blue phases entails kinetic stabilization of amorphous networks. *PNAS*, 107:13212–13215, 2010.

Publications

E. Tjhung, M. E. Cates, D. Marenduzzo. Non-equilibrium steady states in polar active fluids. *Soft Matter*, 7:7453-7464, 2011.

E. Tjhung, D. Marenduzzo, M. E. Cates. Spontaneous symmetry breaking in active droplets provides a generic route to motility. *PNAS*, 109:12381-12386, 2012.

E. Tjhung, A. Tiribocchi, D. Marenduzzo, M. E. Cates. A minimal physical model captures the shapes of crawling cells. (in preparation), 2013.